Attached eddies in wall-bounded turbulent flows: streak instability and skin-friction generation.

Imperial College London

Matteo de Giovanetti

Department of Aeronautics

Imperial College London

A Thesis submitted for the degree of

PhilosophiæDoctor (PhD)

01 2018

Date of Examination: 22/03/2018

- Internal Examiner: Prof. Sergei Chernyshenko, *Imperial College London.*

- External Examiner: Dr Ati Sharma, *University of Southampton.*

Supervisor: Dr Yongyun Hwang, *Imperial College London.*

Umbra profunda sumus, ne nos vexetis inepti.
Non vos, sed doctos tam grave quaerit opus.

Declaration of Originality

The work presented in this Document is the Author's own. Any external contribution is duly acknowledged and appropriately referenced.

Copyright Declaration

Abstract

The goal of this study is to answer some lingering questions that pertain the nature of wall-bounded turbulent flows. Building on the 'attached-eddy' hypothesis first proposed by A.A. Townsend, the main aim is to better understand the mechanisms governing their behaviour. In order to do so, several numerical experiments are performed in a turbulent channel flow. First, we seek for a better description of the mechanism behind the generation of the vortical structures: a body forcing is introduced in the flow to drive an amplified streak, and this process is carried out for several different streaks, ranging from the logarithmic to the outer region. All streaks are shown to undergo a sinuous-type instability; furthermore, they trigger the appearance of cross-streamwise structures, the streamwise wavelength scale of which is observed to be proportional to the spanwise spacing of the amplified streak. Application of dynamic mode decomposition reveals that the amplified streak can be considered the seeding mechanism for these vortical structures. Furthermore, the contribution of attached eddies to skin-friction drag is studied at relatively large Reynolds numbers. It is found that the outer-layer structures are responsible for a significant amount of skin-friction, but their removal does not result in comparable savings. Conversely, the self-similar structures populating the logarithmic layer are shown to generate a substantial amount of skin friction, and their contribution appears to increase with the Reynolds number. This outcome can explain the reduction in effectiveness of many drag-reducing devices, and is potentially useful to design novel techniques for flow control.

Contents

List of Figures

List of Tables

1

Introduction

Fluid flows have always been regarded as a major conundrum in science, and today several questions remain unresolved. These issues become ever more significant, as the engineering practice is focused on the preservation of planetary resources, and therefore the reduction of energy expenditure in all applications. Indeed, it turns out that the one of the main causes of inefficiency is represented by friction, and fluid flows are no exception. Consequently, extensive research has historically been carried out aimed at the mitigation of energy losses due to skin-friction drag, i.e. the friction between the fluid and a solid surface. At the same time, turbulence is an inherent and unavoidable feature in the vast majority of such flows. It follows that a correct understanding of its underlying principles and predominant features is instrumental in devising effective techniques to reduce friction losses at the wall and therefore increase energetic efficiency.

1.1 Coherent structures in wall-bounded turbulent flows

Coherent structure is a term that describes statistically and dynamically organised fluid motion in a chaotic flow field of turbulence. These entities have been shown to be instrumental to the onset and sustenance of turbulence, and their importance has been long known (Cantwell, 1981; Hussain, 1986; Sirovich, 1987); for these reasons, an extensive insight into the nature of coherent structures is hereby presented, with particular focus on the most up-to-date findings. The layout follows the current, shared understanding of wall-bounded flows, which prescribes the existence of three spatial regions showing different properties: the near-wall layer, the logarithmic layer and the outer layer.

1.1.1 Near-wall region

Near-wall layer is the name given to the region of space that includes the flow immediately above the wall. Its extent is generally assumed to end at $y^+ = \frac{yu_\tau}{\nu} = 30$ (where u_τ is the friction velocity and ν the kinematic viscosity), as initially showed by von Kármán (1930) when he formulated his well-known law of the wall. Although more recent studies have tried to assess whether this limit is meaningful or not (Nagib & Chauhan, 2008; Zagarola & Smits, 1998), the near-wall region is still widely assumed to terminate at this coordinate. As of today, there exists overall consensus on the coherent structures, and related processes, that populate the near-wall region. Quasi-streamwise vortices and elongated, meandering streaks are the predominant features in this layer, and account for the largest part of turbulent activity. Their existence and sustainment are considered to be essential to turbulence itself (Jimenez & Moin, 1991; Robinson, 1991). Kline *et al.* (1967) made one of the very first observations on the streaky motions in the near-wall region: a spanwise-alternating pattern of low-speed and high-speed flow with a mean spacing in the order of $\lambda_z^+ \approx 100$ (Smith & Metzler, 1983). The presence of streamwise-oriented vortices as coherent structures was postulated by Kim *et al.* (1987), who showed their existence by analysing the correlations in spanwise and wall-normal velocity, and measuring a mean diameter in the order of $\lambda_z^+ = 50$. Additional evidence of counter-rotating streamwise vortices flanking the streaks has been shown by Jeong & Hussain (1997), by employing a visualisation method developed specifically for vortical structures: these were observed with an average upward inclination and varying longitudinal tilting, albeit very small. These vortices have been found to be strongly correlated to the generation of skin friction in this region (Choi *et al.*, 1994; Kravchenko *et al.*, 1993; Orlandi & Jimenez, 1994).

The origin of these flow features has been object of extensive studies as well, and evidence has been mounting, pointing at a self-sustaining mechanism of the coherent structures. The first suggestions of a cycle of this kind can be found in Kim *et al.* (1971). The causal relationship between the existence of the vortices and the formation of the streaks has been first postulated by Blackwelder & Eckelmann (1979), whereas the first explanation regarding the regeneration of the vortices was proposed in the form of a mechanism involving inflectional instability by Swearingen & Blackwelder (1987). A systematic formalisation of these concepts was carried out by Hamilton *et al.* (1995), who proposed a three-stage regeneration process, which has been thoroughly studies and refined ever since. However, although the existence of a self-sustaining process has been widely proven and is now generally accepted, the exact mechanisms are not yet completely agreed upon. An overview of the main concepts and theories is now presented:

1. Overall, the formation of the streak is considered to be due to extraction of energy from the mean flow, but several mechanisms have been proposed. One theory suggests that the streak is amplified as a consequence of the 'lift-up' effect, the mechanism by which the vortices extract momentum from the mean shear and inject it into the streak. The lift-up effect is associated with the non-normality of the linearised Navier-Stokes operator, and it is understood to play a central role in determining the spanwise spacing of the near-wall streaks (del Álamo & Jiménez, 2006; Butler & Farrell, 1993; Cossu *et al.*, 2009; Hwang & Cossu, 2010*b*; Pujals *et al.*, 2009; Willis *et al.*, 2010). There have also been suggestions that the streak is generated as a combination of lift-up, shear and viscous diffusion (Chernyshenko & Baig, 2005*a*,*b*).

2. The generation of the vortical structures is the second step in the cycle, and has been extensively linked to the instability and breakdown of the streak. In particular, the secondary instability and/or transient growth, involving a rapid streamwise meandering motion (i.e. sinuous mode) (Hamilton *et al.*, 1995; Schoppa & Hussain, 2002), has been proposed as the principal mechanism. Following a previous observation on the role of the streak (Jiménez *et al.*, 2004), Jiménez (2013*a*) has suggested that the inviscid Orr mechanism plays an important role for the existence of the vortices.

3. Vortical perturbations are generated, which eventually develop into new streamwise vortices via non-linear mechanisms (Hamilton *et al.*, 1995; Schoppa & Hussain, 2002).

It is here interesting to also mention the results that have been obtained by using stochastic forcing in linearised models, to account for the effect of nonlinearities in the original Navier-Stokes equation. In particular, it has been observed that linearised models only show bounded growth of fluctuations when such a body forcing is applied. Using this approach, the emergence of correct one-point correlations and energy spectra has been shown in various studies (Farrell & Ioannou, 1998; Jovanović & Bamieh, 2001; Moarref & Jovanović, 2012).

Contrary to the early views, recent studies at large Reynolds numbers appear to indicate that the near-wall structures are not completely independent from the flow above. For instance, Metzger & Klewicki (2001) showed that the near-wall structures can be affected by the energy transfer from the logarithmic region. More recent findings have shown that an amplitude modulation effect also exists, by which the logarithmic and the outer layer structures affect the near-wall region (Hutchins & Marusic, 2007*b*; Mathis *et al.*, 2009, 2013; Morrison, 2007). Nonetheless, the regeneration cycle in itself has been understood to be essentially independent of the motions in the logarithmic and outer regions, since the near-wall structures survive even if the motions above the near-wall region are not properly resolved or are artificially filtered out (Hwang, 2013; Jiménez & Pinelli, 1999; Jimenez & Moin, 1991). Consequently, the self-sustaining mechanism should be considered as an essential property of turbulence.

1.1.2 Logarithmic layer

The logarithmic layer is the region of flow where the mean-velocity profile shows a logarithmic dependence on the wall-normal coordinate, and is located in between the near-wall region and the outer flow. In order to meaningfully describe the coherent structures in this region, it is necessary to introduce and refer to the seminal work of Townsend (1961). In the logarithmic region, the only relevant length scale is the distance from the wall 'y' (the wall-normal direction) which allows one to asymptotically match between the law of the wall and the velocity defect law at high Reynolds numbers (Millikan, 1938). Townsend (1961, 1976) deduced that it would be difficult to explain this feature unless the size of the energy-containing motions (i.e. coherent structures) in the logarithmic region were proportional to the distance of their centres from the wall. The energy-containing motions in the logarithmic region would therefore extend to the wall, and, in this sense, they would be 'attached' to the wall (i.e. 'attached eddy' hypothesis). Under the assumption that these energy-containing motions in the logarithmic region (i.e. attached eddies) are statistically self-similar, Townsend (1976) theoretically predicted that turbulence intensity of the wall-parallel velocity components would exhibit a logarithmic wall-normal dependence, whereas the wall-normal components and the Reynolds stresses would not.

In the last decade, the sharp increment in computational power has made possible to assess the correctness of Townsend's hypotheses (since the extent of this region depends directly on the friction Reynolds number Re_τ); in particular, the predicted behaviour of the velocity fluctuations has been widely tested. The growth of the near-wall streamwise peak (De Graaff & Eaton, 2000; Metzger & Klewicki, 2001) has been explained as an extension of the attached eddies paradigm to the near-wall itself (Marusic & Kunkel, 2003). More recently, the logarithmic wall-normal dependence of the turbulence intensities of wall-parallel velocity components has been shown and repeatedly confirmed at sufficiently high Reynolds numbers (Jiménez & Hoyas, 2008; Lee & Moser, 2015; Marusic *et al.*, 2013; Perry & Chong, 1982; Perry & Marusic, 1995), suggesting that the energy-containing motions in wall-bounded turbulent flow would indeed be organised in the form of Townsend's attached eddies. The linear growth of the spanwise integral length scale with the distance from the wall has been understood as another important evidence (Hwang, 2015; Hwang & Cossu, 2010*c*; Tomkins & Adrian, 2003), as this indicates that the spanwise size of the energy-containing motions in the logarithmic region is proportional to the distance from the wall as in Townsend's hypothesis (Tomkins & Adrian, 2005). All the presented findings directly support the notion that the entire logarithmic layer consists of a hierarchical form of self-similar coherent structures, as proposed in the seminal work of Townsend (1961, 1976) and Perry & Chong (1982). The aspect ratio of these structures has been shown to be approximately constant, as it would be expected because of their self-similarity, and has been observed to be around $\lambda_x \approx 2\lambda_z \approx 3y$ (del Álamo *et al.*, 2006; Hwang, 2016).

More recently, a further analysis on the attached eddy hypothesis up to $Re_\tau \approx 1800$ has been performed by Hwang (2015). In this study, energy-containing motions at a given spanwise length scale are isolated using a combination of the over-damped LES (Hwang & Cossu, 2010*c*, 2011), which effectively suppresses the smaller structures, and a filter capable of removing the structures larger than a required spanwise dimension (Hwang, 2013). The isolated self-sustaining energy-containing motions were found to be self-similar with respect to their spanwise length scale, and their statistical structures to be remarkably similar to those of the attached eddies, providing direct evidence on the existence of Townsend's attached eddies as energy-containing motions in the logarithmic layer. Furthermore, the attached eddy at a given wall-normal location has been described as composed of two structures: one is an elongated region of low-momentum, already observed in previous studies (Ganapathisubramani *et al.*, 2006; Hutchins & Marusic, 2007*a*). The second one has been named as either "hairpin vortex packet" (Ganapathisubramani *et al.*, 2006; Tomkins & Adrian, 2003) or "tall attached cluster" (del Álamo *et al.*, 2006), and can be described as counter-rotating vortical structures. In essence, these features mirror the structures in the near-wall region, suggesting that the near-wall coherent structures would be the smallest attached eddy in the flow.

1.1.3 Outer region

The region above the logarithmic region, usually defined as outer region, has been initially investigated in boundary layers. Research by Kovasznay and coworkers (Kovasznay, 1970; Kovasznay *et al.*, 1970) introduced the concept of lumps as Large-Scale Motions (LSMs) residing at the interface between turbulent and non-turbulent flow. These lumps are ejected from the underlying portion of the boundary layer and have a momentum defect that contributes in creating a turbulent wake, which gradually extends downstream. Subsequent observations were made, in the following years, by Falco, in a series of papers: the concept of typical eddy is introduced, defined as a coherent, three-dimensional structure that is of comparable size with the boundary layer thickness (Falco, 1974), and highly dependent on Reynolds number (Falco, 1991). Head & Bandyopadhyay (1981) initially postulated that the typical eddies would be in the form of hairpin vortices, which they observed in the flow. Over many years, Adrian and coworkers have argued that a hairpin vortex is the fundamental form of the coherent structures in wall-bounded flows. The LSMs are today understood to be the carriers of intense wall-normal and spanwise turbulent kinetic energy (Hwang, 2015; Hwang & Bengana, 2016), with a streamwise extent of $O(\delta)$ (where δ is the outer length scale). The second predominant feature in the outer region is the Very-Large-Scale Motion (VLSM) given in the form of a long and meandering streaky motion that dominates the spectra of streamwise velocity (del Álamo & Jiménez, 2003; Hutchins & Marusic, 2007*b*; Kim & Adrian, 1999), and shows a streamwise extent of $O(10\delta)$. The VLSM is a very energetic feature in the outer region and carries a significant portion of the total turbulent kinetic energy and the Reynolds stress of the flow (Guala *et al.*, 2006).

1.1.4 The self-sustaining mechanism

sec:Selfsust Recently, there has been a growing body of evidence that the outer coherent motions (i.e. LSM and VLSM) are largely independent of the near-wall cycle: for example, a number of numerical and laboratory experiments performed with rough walls have shown that the outer statistics related to LSMs and VLSMs are essentially unaffected by the disruption of the near-wall structures in the underlying flow (Flores & Jiménez, 2006; Flores *et al.*, 2007; Hutchins & Marusic, 2007*a*; Rosenberg *et al.*, 2013). Additional progress has been made by Hwang & Cossu (2010*c*, 2011), who have found that both the logarithmic and the outer coherent structures display a self-sustaining mechanism, which is largely independent from the near-wall region. These results have been further extended, to the point where the self-sustaining mechanism at a given length-scale appears now to be broadly unaffected by either smaller and larger scales (Hwang, 2015; Hwang & Bengana, 2016).

Despite this emerging evidence for the existence of a self-sustaining cycle at all scales, there is still no consensus on the exact mechanisms that lead to their generation and sustainment. In the framework of hairpin vortices, it has been argued that their generation is a non-linear mechanism, a process called 'auto-generation': this starts with the formation of a packet of hairpin vortices in the near-wall region (Adrian & Liu, 2002; Adrian *et al.*, 2000; Zhou *et al.*, 1996), and progresses with hairpin vortex packets subsequently growing and merging into one another in the logarithmic region, eventually forming a LSM in the outer region (Adrian, 2007; Perry *et al.*, 1986). The VLSM is then interpreted as a concatenation of adjacent LSMs (Baltzer *et al.*, 2013). However, this scenario is effectively inconsistent with the existence of self-sustaining mechanism; furthermore, the mergers/growth paradigm does not provide any explanation as to why the streamwise length scale of LSMs is determined to be $\lambda_x \approx 1 - 5\delta$. In light of these apparent contradictions, novel explanations have been sought for.

The resolvent norm framework, introduced by McKeon & Sharma (2010), has proved helpful to investigate the dynamics of the coherent structures. They suggested that the dominant features of turbulent flows can be considered as a superposition of different response modes; furthermore, they were able to show that the VLSM arises naturally as a solution of the forced linear equation that result from the resolvent-norm analysis. In a subsequent study (Sharma & McKeon, 2013), it is postulated that the VLSM does not appear as a concatenation of hairpin vortices, but is indeed a separate entity that interacts with the vortices in a mutually supportive manner.

More recent investigation have interpreted the generation of elongated streaks as a result of the lift-up effect (Cossu *et al.*, 2009; Hwang & Cossu, 2010*a*,*b*; Pujals *et al.*, 2009; Willis *et al.*, 2010), in a manner equivalent to their near-wall counterpart; it has also been shown that artificial inhibition of the lift-up effect destroys the self-sustaining mechanism (Hwang & Bengana, 2016). This structural similarity suggests that the initiating mechanism of LSMs may be an instability of the amplified outer streak (VLSM), like that of streamwise vortices in the near-wall region. Indeed, a recent stability analysis with an eddy viscosity model revealed that the amplified streak becomes unstable at the typical streamwise length scale of the LSM and that the corresponding instability mode is characterised by a meandering motion of the streak (i.e. sinuous-mode instability) (Alizard, 2015; Park *et al.*, 2011). In the framework of stochastic forcing, Zare *et al.* (2017) have analysed the spatio-temporal response of turbulent channel flow subjected to a time-dependent forcing (i.e. 'coloured in time'): they showed that structures very closely resembling the VLSM arise, closely flanked by alternating regions of counter-rotating vortical motions. This result is interesting because the non-linearities are modelled by the forcing itself, which supports the idea that the generation of the vortical structures is inherently nonlinear. We also mention that both the approaches, i.e. the instability and the broadband forcing, involve the separation of the flow into a base flow component, and a fluctuation component. As a consequence of this underlying characteristics, it might be difficult to distinguish between the perturbations due to the instability of the streak, and the ones introduced by the broadband forcing, and this issue should be taken into account when interpreting the response of the flow to the amplified streak (see §1.3).

Despite these theoretical findings, the issue of how the vortical structures in the logarithmic and outer regions are formed remains unsettled, even among the work supporting the self-sustaining process. Indeed, Jiménez (2013*a*,*b*) recently proposed that the Orr mechanism, which describes the transient amplification of a spanwise vortical perturbation by the mean shear, plays a role in the generation of the vortical structures. However, it should be pointed out that the Orr mechanism does not provide any description of the streamwise length-scale selection of the vortical structures, casting doubt on whether the Orr mechanism is the primary mechanism of the generation of vortical-structure. Finally, it should be mentioned that most of the previous numerical studies have investigated the dynamics of the self-sustaining process only with a very short streamwise computational domain (Flores & Jiménez, 2010; Hwang & Bengana, 2016). This restriction does not allow one to explore the mechanism by which the streamwise length scale of the coherent structures at a given spanwise length scale is determined.

1.2 Skin friction

The concept of coherent structures ties very closely with the issue of drag reduction, since it has been widely demonstrated that their role in skin-friction generation is of paramount relevance. As a consequence, several flow control techniques have been devised to target these features, and have proved themselves successful, e.g. opposition control (Choi *et al.*, 1994) and spanwise oscillations (Jung *et al.*, 1992; Stadsted & Moin, 1991). It should be noted that these control strategies perform very well at low Reynolds numbers, yielding a considerable amount of turbulent drag reduction. However, it has recently been reported that their effectiveness is deteriorated on increasing the Reynolds number (Chang *et al.*, 2002), even though the direct effect of these controls on the near-wall region appears to remain fundamentally unchanged (Agostini *et al.*, 2014). It now appears that virtually all flow control methods targeting directly the near-wall structures suffer from performance loss with an increase in Reynolds number. This trend has been similarly observed for opposition control, polymer additives and spanwise oscillations (Belan & Quadrio, 2013; Gatti & Quadrio, 2013; Touber & Leschziner, 2012). An explanation for this behaviour has been put forward by Luchini (1996), who postulated that the shift in logarithmic region of the velocity profile is independent of Re, provided that the drag-reduction parameters are as well (when scaled in inner units). The following equation is devised:

$$\frac{\Delta C_f}{C_f} = \frac{\Delta h}{(2C_f)^{-1/2} + \kappa} \tag{1.1}$$

where C_f is the skin-friction coefficient, Δh is the vertical shift in the law of the wall, and $\kappa \approx 0.41$ is the von Karman constant. According to this formula, therefore, the decrease in skin friction is dependent on the skin friction itself, and therefore on the Reynolds number. For a reduction in base skin friction, a larger vertical shift would be required to generate the same relative drag reduction, which would justify the decline in effectiveness.

Nonetheless, further effort has been made to better understand the imprint of the outer coherent structures on the wall-shear stress: evidence of this type of interaction has been presented for both internal (Abe *et al.*, 2004) and external flows (Schlatter *et al.*, 2009). The direct influence of large-scale structures on the near-wall region has been also described through a modulation mechanism (Hutchins & Marusic, 2007*b*; Mathis *et al.*, 2009, 2013). Using resolvent analysis, Luhar *et al.* (2015) showed that compliant walls would need different damping characteristics when targeting coherent structures of different sizes: they therefore suggested that this is the reason for the reduced effectiveness of flow control techniques which are optimised for the near-wall structures. At the same time, optimising all the scales might prove comprehensibly problematic. A recent study by Hwang (2013) further highlighted the increasing role in wall-shear stress production of structures that reside in the logarithmic and wake region, by performing a numerical experiment which filters out turbulent motion wider than the characteristic near-wall spanwise length scale ${\lambda_z}^+ \simeq 100$. Importantly, the contribution of the isolated near-wall structures to wall shear stress was found to rapidly decay on increasing the Reynolds number, suggesting that a significant amount of turbulent skin friction originates from the logarithmic and outer regions. The large contribution of the structures above the near-wall region was also confirmed in a turbulent boundary layer more recently by Deck *et al.* (2014) and Renard & Deck (2016), with two separate methods leading to very similar conclusions. Here, it should also be mentioned that the quasisteady quasihomogenoeus analysis by Zhang & Chernyshenko (2016) has strived to model the reduced effectiveness of drag-reducing techniques at high Re, by exploiting the modulation effect of the large scales on the near-wall structures.

1.3 Motivations and objectives

The concept of attached eddies is relatively old, and has been extensively studied in a number of different frameworks. Nonetheless, there are several questions that still linger in the research community about the characteristics and overall role that these structures have in turbulent flows. Coherent structures have been consistently shown to exist at all scales in the flow, and novel evidence has shown their essential self-similarity (del Álamo *et al.*, 2006; Hwang, 2015); this type of organisation is reminiscent of the early theories from Townsend (1976), and his concept of 'attached eddies'. The existence of self-sustaining processes at all scales, and their eventual similarity to the near-wall cycle (Hamilton *et al.*, 1995), is still very much debated, although recently evidence has been presented for their existence, at least in isolation (Hwang & Cossu, 2010*c*, 2011). With these working hypotheses, the present study has strived to shed more light on the following topics specifically:

1. The exact steps that link the generation, and regeneration, process of coherent structures is still far from completely explained. Earlier studies proposed that mergers and/or growth of the hairpin vortices from the near-wall region could be the generation mechanism of the vortical structures in the logarithmic and outer regions (Adrian *et al.*, 2001; Perry *et al.*, 1986; Zhou *et al.*, 1999). The largest vortical structure generated by this process was thought to be the LSM (Adrian, 2007) and a VLSM was subsequently interpreted as a concatenation of adjacent LSMs (Baltzer *et al.*, 2013). However, it should be pointed out that LSMs and VLSMs emerge even in the absence of motions in the near-wall and logarithmic regions (Hwang, 2015; Hwang & Cossu, 2010*c*). They also remain virtually unchanged in the presence of significant disruption of the near-wall region (Flores & Jiménez, 2006; Hutchins & Marusic, 2007*b*). Finally, the hairpin vortex paradigm does not provide any explanation with regards to the streamwise length scale of the LSMs, which has been repeatedly observed to be $\lambda_x \simeq 1 - 5\delta$ (where λ_x is the streamwise wavelength, and δ is the outer length scale, such as the boundary-layer thickness, half-height of the channel, and radius of the pipe). For this reason, an experiment is devised to investigate the direct relationship between the outer streaks, their breakdown and the generation of large-scale vortical structures. This part has been carried out by artificially driving streaks using a forcing profile computed by Hwang & Cossu (2010*b*). By gradually increasing the forcing amplitude, the objective is to observe the formation of the vortical structures, and to help shed light on the mechanisms that lead to it.

2. Currently, there is compelling evidence for the existence of a self-similar, self-sustaining process of the coherent structures in the logarithmic region, independently of both the near-wall and the outer regions (Hwang, 2015; Hwang & Cossu, 2011). However, the steps leading to the generation of the vortical structures are still debated, and a number of mechanisms has been proposed, similarly to the outer region. We essentially replicate the approach used in the outer layer (and presented in the previous point), to study the relationship between the meandering streaks and the vortical structures, and assess whether similarities exist at different scales, and indeed with the previous results obtained in the outer layer.

3. Despite a growing body of recent evidence on the hierarchical organisation of the self-similar energy-containing motions in the form of Townsend's attached eddies in wall-bounded turbulent flows, their role in turbulent skin-friction generation is currently not well understood, especially when relatively large Reynolds number (i.e. $Re_\tau > 1000$) are considered. It is currently accepted that at low Reynolds numbers, the quasi-streamwise vortices residing in the near-wall region are responsible for most of the drag production (Kravchenko *et al.*, 1993). However, the mechanism involved in drag generation at higher Reynolds numbers is still broadly unclear. While it now appears that the logarithmic and outer structures could contribute to skin friction (Deck *et al.*, 2014; Hwang & Bengana, 2016), their exact role and significance are debated. A series of numerical experiment has been designed to improve our understanding of this issue.

1.4 Organisation of the Thesis

The present Thesis is organised as follows: chapter 2 serves as a repository for all the methodologies employed throughout the whole study; chapter 3 tries to unveil the role of the very-large-scale motions in the formation of large-scale motions; similarly, in chapter 4 the relationship between the elongated streak and the vortical motions is studied in the logarithmic layer; chapter 5 deals with the contributions to skin-friction production from coherent structures at different scales; finally, chapter 6 rounds up the main results of this research, outlining the most important conclusions and proposing an outlook for future investigations.

It should be also mentioned that results reported in chapter 2, 3 and 4 have been published, or under review, in peer-reviewed articles, respectively:

[1] de Giovanetti M., Hwang Y. & Choi H. 2016, *Skin-friction generation by attached eddies in*

turbulent channel flow, **Journal of Fluid Mechanics**, 808, 511-538.
[2] de Giovanetti M., Sung H.J. & Hwang Y. 2017, *Streak instability in turbulent channel flow: a seeding mechanism of large-scale motions*, **Journal of Fluid Mechanics**, 832, 483-513.
[3] de Giovanetti M. & Hwang Y., Self-similar streak instability and vortex packet formation in the logarithmic layer of turbulent channel flow, **Physical Review Fluids**, *sub judice*.

Furthermore, some of the tools developed for this study have been used to investigate the near-wall structures. The results have been published in:
[4] Cassinelli A., de Giovanetti M. & Hwang Y. 2017, *Streak instability in near-wall turbulence revisited*, **Journal of Turbulence**, 18(5), 443-464.

2

Methodologies

This chapter collects and presents all the methodologies that have been employed to obtain the results shown throughout this document. All the numerical experiments have been carried out computationally, in the form of large-eddy-simulations. The main features of this technique are reported in §2.1, and are valid for all the performed simulations. Following, the two main methods that enable the study of the streak instability are detailed: the body forcing to drive the streak in §2.2, and the dynamic mode decomposition in §2.3; these are relevant to chapters 3 and 4. Lastly, the three different approaches for the determination of skin friction from different scales are documented in §2.4; these apply to chapter 5.

2.1 Large eddy simulation

The potential for numerical simulations of fluids was spotted very early in the computer age (Corrsin, 1961), and has been extensively exploited ever since. One of the very first techniques was theorised by Smagorinsky (1963), and initially intended for meteorological flows; this approach, currently known as large-eddy-simulation (LES), was employed for wall-bounded flows only at a later stage, by Deardorff (1970). Since those early years, the exponential improvement in computational power has transformed this instrument into a fundamental staple in turbulence and fluid research.

LES relies on a filtering procedure to reduce the computational requirements of direct numerical simulation (DNS), by assuming an universality of the smallest scales in a given flow (Rogallo & Moin, 1984). It therefore represents an interesting and widely employed trade-off between the accuracy of the solution and the computational cost, since the smaller-scale motions are modelled instead of directly resolved. The required filter is often applied to the Navier-Stokes equations in space, so that only the residual stress generated by small-scale structures needs to be modelled (Meneveau & Katz, 2000).

The initial filtering operation decomposes the velocity field $\mathbf{u}(\mathbf{x}, t)$ into the sum of two components, i.e. the resolved velocity component $\overline{\mathbf{U}}(\mathbf{x}, t)$ and the sub-grid velocity component $\mathbf{u}'(\mathbf{x}, t)$:

$$\mathbf{u}(\mathbf{x}, t) = \overline{\mathbf{U}}(\mathbf{x}, t) + \mathbf{u}'(\mathbf{x}, t) \tag{2.1}$$

Even though this procedure is reminiscent of Reynolds-averaging, it must be stressed that the two techniques are starkly different in both concept and results, since the time-average of the sub-grid component is different from 0. The filtering operation can be written, for a general variable $\phi(\mathbf{x}, t)$, as

$$\overline{\phi}(\mathbf{x}, t) = \int_{-\infty}^{\infty} G(\mathbf{r}, \mathbf{x})\phi(\mathbf{x} - \mathbf{r})\mathrm{d}\mathbf{r} \tag{2.2}$$

where $G(\mathbf{r}, \mathbf{x})$ is a filter function that satisfies the normalisation condition

$$\int_{-\infty}^{\infty} G(\mathbf{r}, \mathbf{x})\mathrm{d}\mathbf{r} = 1 \tag{2.3}$$

When this filter is applied to the incompressible Navier-Stokes equations, the corresponding equations for the resolved velocity field can be derived:

$$\frac{\partial \overline{u}_i}{\partial t} + \frac{\partial}{\partial x_j}(\overline{u_i u_j}) = -\frac{1}{\rho}\frac{\partial \overline{p}}{\partial x_i} + \nu \frac{\partial}{\partial x_j}\left(\frac{\partial \overline{u}_i}{\partial x_j} + \frac{\partial \overline{u}_j}{\partial x_i}\right) \tag{2.4}$$

The non-linear advection term $\frac{\partial}{\partial x_j}(\overline{u_i u_j})$ contains informations about the sub-grid velocity field, and therefore needs to be modelled. According to Leonard (1974), this term can be expressed as

$$\overline{u_i u_j} = \tau_{ij}^r + \overline{u}_i \overline{u}_j \tag{2.5}$$

where the sub-grid stress tensor τ_{ij}^r is the unknown term. Several models have been proposed to model this term, since it can considerably affect the fidelity of the numerical simulation. For more details on the fundamentals of large-eddy-simulations, and the most recent developments and issues, the reader can refer to Argyropoulos & Markatos (2015); Piomelli & Balaras (2002); Pope (2000, 2004).

2.1.1 DIABLO code

To perform the numerical simulation, an existing open-source CFD code (DIABLO) has been adopted and used as a foundation to further develop the required capabilities (Bewley *et al.*, 2001). Its performance had been previously validated as a DNS solver (Hwang, 2013), and a LES module has been developed specifically for this study (see next section). A brief outline of the code is hereby presented.

Incompressible Navier-Stokes equation The simulated system is governed by the incompressible Navier-Stokes equation, given by

$$\frac{\partial u_i}{\partial t} = \frac{\partial u_j u_i}{\partial x_j} + \nu \frac{\partial^2 u_i}{\partial x_j^2} - \frac{1}{\rho}\frac{\partial p}{\partial x_i} + \Psi_i \tag{2.6a}$$

$$\frac{\partial u_j}{\partial x_j} = 0 \tag{2.6b}$$

The momentum equation (2.6a) is marched in time, whereas the continuity equation (2.6b) represents a constraint for the velocity field, which must be satisfied at every time-step. The equations are written for a three-dimensional system with the following nomenclature: the streamwise, wall-normal and spanwise directions are denoted as x, y and z, respectively, and the corresponding velocities are defined as u, v and w, respectively. In order to correctly simulate channel flow, the lower and upper walls of the channel are set at $y = 0$ and $y = 2h$, where h denotes the half-height of the channel, and it is used as the outer length scale. Boundary conditions are enforced as periodic in the streamwise and spanwise directions, and pre-determined in the wall-normal direction. To drive the flow, a pressure gradient is imposed through the term $\Psi_i = -P_x\delta_{ij}$, such that the mass flux is kept constant.

Numerical implementation The partial differential equation describing the continuous flow field is approximated as a constrained ordinary differential equation (ODE), discretised on a finite set of points, and discrete time steps are used to march the ODE in time. The computational points are equally spaced in the streamwise and spanwise direction, and stretched in the wall-normal direction, to obtain an optimal trade-off between the resolution in the near-wall region and the computational cost. The numerical solver discretises the ODE in the streamwise and spanwise directions using Fourier series with the 2/3 dealiasing rule. In particular, given a function $u(x, y, z, t)$, the Fourier transform is performed so that the corresponding truncated function $u_t(x, y, z, t)$ can be obtained as a sum of Fourier coefficients

$$u_t(x, y, z, t) = \sum_{n=-N_x/3}^{N_x/3} \sum_{m=-N_z/3}^{N_z/3} \hat{u}_m(k_x, k_z; y, t) e^{ik_z z} e^{ik_x x} \tag{2.7}$$

where N_x and N_z are the number of computational points in the streamwise and spanwise directions, and

$$k_x = \frac{2\pi n}{L_x} \qquad k_z = \frac{2\pi m}{L_z} \tag{2.8}$$

This procedure allows the computation of the spatial derivatives with respect to x and z. Derivatives with respect to y are computed using a second-order central finite difference. The time-stepping is performed semi-implicitly with a fractional step method: the Crank-Nicolson method is used for the terms with wall-normal derivatives and a third-order Runge-Kutta method is used for all the remaining terms. At every step of the Runge-Kutta method, the velocity field is made divergence-free by using the pressure update obtained through the solution of the Poisson equation.

Two Reynolds numbers are used to characterise the simulated flow, the bulk Reynolds number $Re_m = U_m h/\nu$ and the friction Reynolds number $Re_\tau = u_\tau h/\nu$. The bulk velocity scale U_m is defined as:

$$U_m = \frac{1}{2h} \int_{-h}^{h} \langle u \rangle_{x,z} \mathrm{d}y \tag{2.9}$$

where $\langle \cdot \rangle_{x,z}$ represents the average in streamwise and spanwise direction respectively. The friction velocity u_τ is defined as:

$$u_\tau = \sqrt{\frac{\tau_\mathrm{w}}{\rho}} = \sqrt{\frac{(\partial u/\partial y)_\mathrm{w}}{\rho}} \tag{2.10}$$

where ρ is the density.

2.1.2 Vreman Model

In the present study, an eddy-viscosity model recently proposed by Vreman (2004) has been implemented in the existing code. The Vreman model was developed to closely match the theoretically-predicted algebraic properties of sub-grid-scale (SGS) dissipation for an extensive database of flows. An important feature of this model is that dissipation by the eddy viscosity becomes relatively small in transitional and near-wall regions, not requiring any special treatment for the near-wall region; conversely, many SGS models require this type of artificial, and often crude, correction in vicinity to the wall (Van Driest, 1956). The model shows performance comparable to the standard dynamic Smagorinsky model (Germano *et al.*, 1991), and its dynamic variant has recently demonstrated a range of applicability to several canonical flows (Park *et al.*, 2006). For further details, the reader may refer to Vreman (2004) and Park *et al.* (2006). In the selected model, the sub-grid stress tensor τ_{ij}^r (defined in 2.5), is modelled as

$$\tau_{ij}^r = -2\nu_e S_{ij} + \tau_{kk}\frac{\delta_{ij}}{3} \tag{2.11}$$

where S_{ij} is the strain-of-rate tensor

$$S_{ij} = \left(\frac{\partial \overline{u}_i}{\partial x_j} + \frac{\partial \overline{u}_j}{\partial x_i}\right) \tag{2.12}$$

and the eddy viscosity ν_e is approximated as

$$\nu_e = c\sqrt{\frac{B_\beta}{\alpha_{ij}\alpha_{ij}}}, \tag{2.13}$$

with

$$\alpha_{ij} = \partial_i \bar{u}_j = \frac{\partial \bar{u}_j}{\partial x_i}, \tag{2.14}$$

$$\beta_{ij} = \Delta_m^2 \alpha_{mi}\alpha_{mj}, \tag{2.15}$$

$$B_\beta = \beta_{11}\beta_{22} - \beta_{12}^2 + \beta_{11}\beta_{33} - \beta_{13}^2 + \beta_{22}\beta_{33} - \beta_{23}^2. \tag{2.16}$$

In these equations, Δ_m is the filter width in each direction, and c is a scalar representing the tuneable model constant.

2.1.3 Validation

The numerical experiment has been validated with several tests carried out at different values of Re_τ to appraise the performance of the Vreman model. Fig. 2.1 compares the mean velocity profile and turbulent velocity fluctuations of the present LES at $Re_\tau \simeq 2000$ (labelled as $F2000$, see table 2.2 for computational details) with those from DNS by Bernardini *et al.*

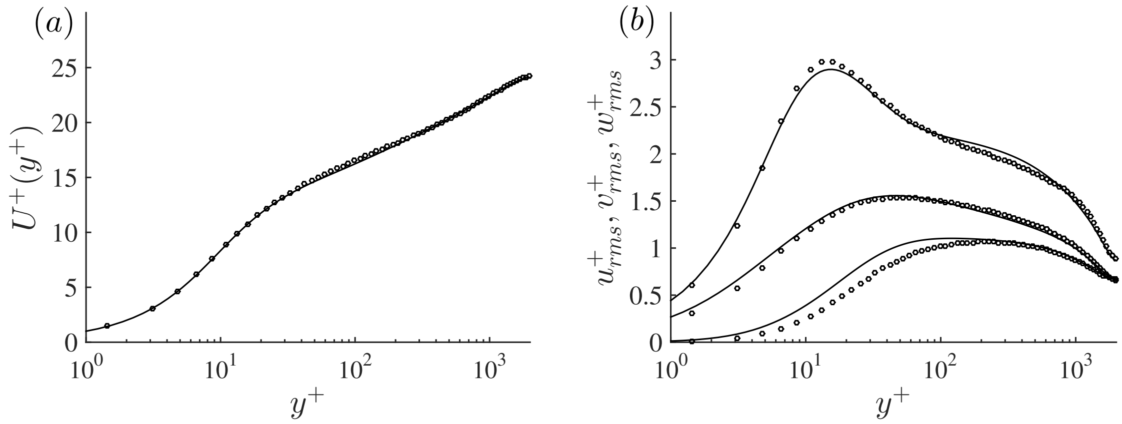

Figure 2.1: (a) Mean velocity profile $U^+(y^+)$ and (b) turbulent velocity fluctuations at $Re_\tau \approx 2000$ (from top to bottom: u^+_{rms}, w^+_{rms}, v^+_{rms}). ——, DNS by Bernardini *et al.* (2014); ○, present LES ($F2000$).

(2014). Very good agreement is observed in the mean velocity profile, and the velocity fluctuations also show acceptable agreement as well. The peak for the streamwise velocity fluctuation is slightly over-predicted, as it is commonly seen in LES. The spanwise and wall-normal components show somewhat smaller intensities than those of DNS, especially in the region closer to the wall, and this behaviour has been reported previously (Dukowicz & Dvinsky, 1992; Gullbrand, 2000; Kravchenko & Moin, 1997; Sarghini *et al.*, 1999). For the purposes of this study, the premultiplied velocity spectra need to show a good level of accuracy as well; consequently, both the streamwise (fig. 2.2) and spanwise (fig. 2.3) energy spectra are compared with the corresponding data from DNS at a very similar Reynolds number, from Hoyas & Jiménez (2006). A satisfactory agreement can be observed, both quantitatively and qualitatively; the only minor mismatch is represented by an under-prediction of the spectral location of the outer peak, both in fig. 2.3(a) and 2.3(d). This is deemed to be a minor inaccuracy, especially when considering the reduced computational cost of LES.

The suitability of this model for drag prediction is also tested. The simulations are carried out with the minimal computational domain, i.e. $L_x = 3.0h$ and $L_z = 1.5h$, and the resulting skin-friction coefficient C_f is compared with those obtained by experiment (Schultz & Flack, 2013) and previous DNSs (Bernardini *et al.*, 2014; Hoyas & Jiménez, 2006; Lee & Moser, 2015; Lozano-Durán & Jiménez, 2014). In fig. 2.4 it is possible to observe that the present LES shows good agreement with both of the existing data and the empirical fit of Dean (1978) over the range of Re_m considered. The small difference at large Reynolds numbers ($Re_m > 10^5$) appears

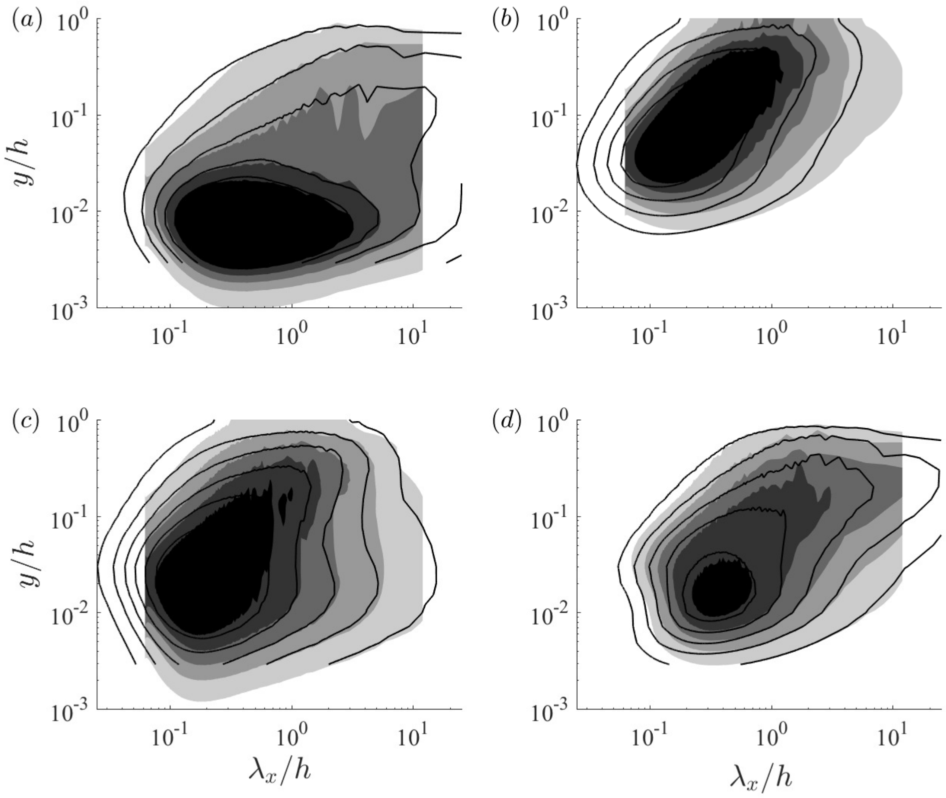

Figure 2.2: Premultiplied one-dimensional streamwise wavenumber spectra of (*a*) streamwise, (*b*) wall-normal, (*c*) spanwise velocities, and (*d*) Reynolds shear stress. Contour lines are equally spaced and each step is 1/6 of the maximum value. Contour lines from Hoyas & Jiménez (2006), shaded contours from present LES.

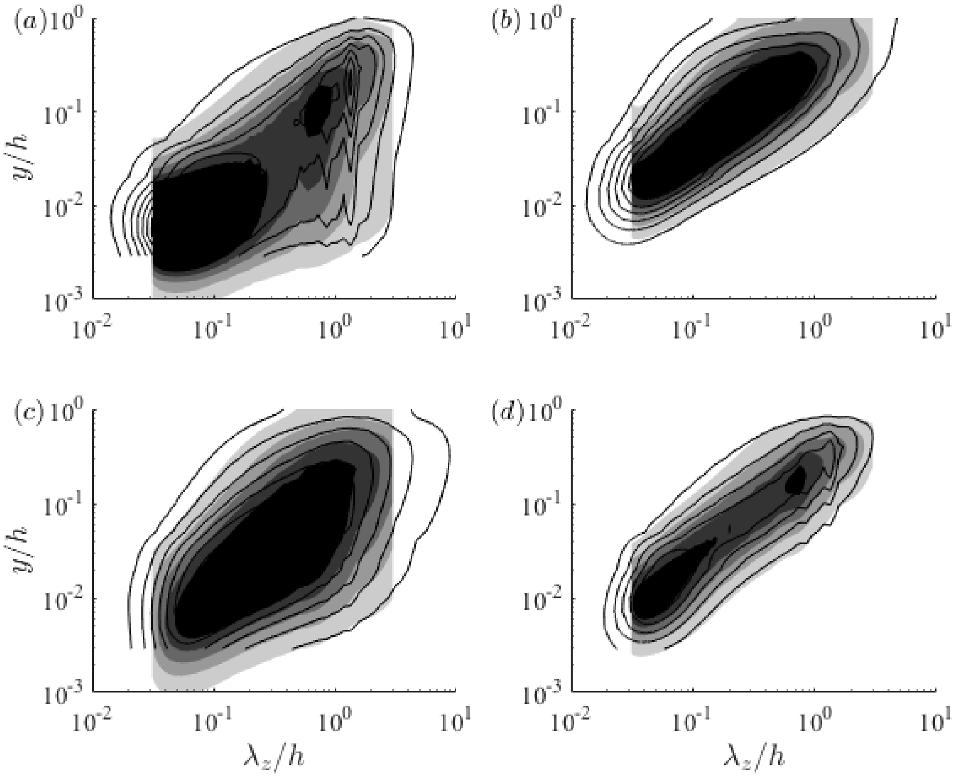

Figure 2.3: Premultiplied one-dimensional spanwise wavenumber spectra of (*a*) streamwise, (*b*) wall-normal, (*c*) spanwise velocities, and (*d*) Reynolds shear stress. Contour lines are equally spaced and each step is 1/6 of the maximum value. Contour lines from Hoyas & Jiménez (2006), shaded contours from present LES.

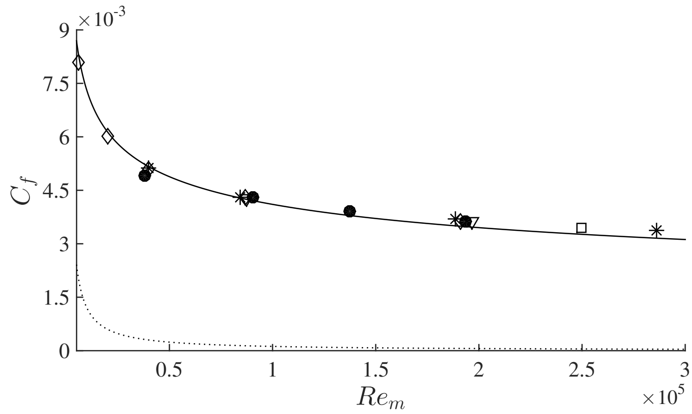

Figure 2.4: Variation of skin friction coefficient with Re_m: ——, empirical fit of turbulent skin friction ($C_f = 0.073Re_m^{-0.25}$, Dean, 1978); - - - -, laminar skin friction ($C_f = 12/Re_m$); $\triangledown$, DNS (Hoyas & Jiménez, 2006; Lozano-Durán & Jiménez, 2014); $\diamond$, DNS (Bernardini *et al.*, 2014); $\square$, DNS (Lee & Moser, 2015); $*$, experiment (Schultz & Flack, 2013); $\bullet$, present LES ($L_x = 3.0h$ and $L_z = 1.5h$).

to be due to a slight imprecision in Dean's original formula, and the issue has been recently addressed by Zanoun *et al.* (2009).

2.2 Body forcing

Given the scope of this study, the role of the body forcing is to drive a long streaky motion in the flow field. We obtain such a body forcing by following Hwang & Cossu (2010*b*), who computed a forcing that drives streaks in an optimal manner using a linear theory. We note that since the forcing is merely to drive the streak, other forms of the forcing can also be considered as long as they can drive a streaky motion. This issue will be further discussed in §3.3.4. In this section, we briefly summarise the procedure to compute the forcing, and the reader may refer to Hwang & Cossu (2010*b*) for further details.

We start by considering the triple decomposition of a given flow field as in Reynolds & Hussain (1972):

$$\mathbf{u} = \mathbf{U}_0 + \tilde{\mathbf{u}} + \mathbf{u}', \tag{2.17}$$

where $\mathbf{u} = (u, v, w)$ is the velocity field, $\mathbf{U}_0 = (U_0(y), 0, 0)$ the mean velocity obtained by averaging in time and in two homogeneous directions, $\tilde{\mathbf{u}}$ the so-called 'organised wave', and $\mathbf{u}'$ the random turbulent velocity fluctuation. If we strictly follow Reynolds & Hussain (1972), $\mathbf{U}_0$ is the mean velocity in the absence of the forcing and $\tilde{\mathbf{u}}$ is the motion induced by a systematically

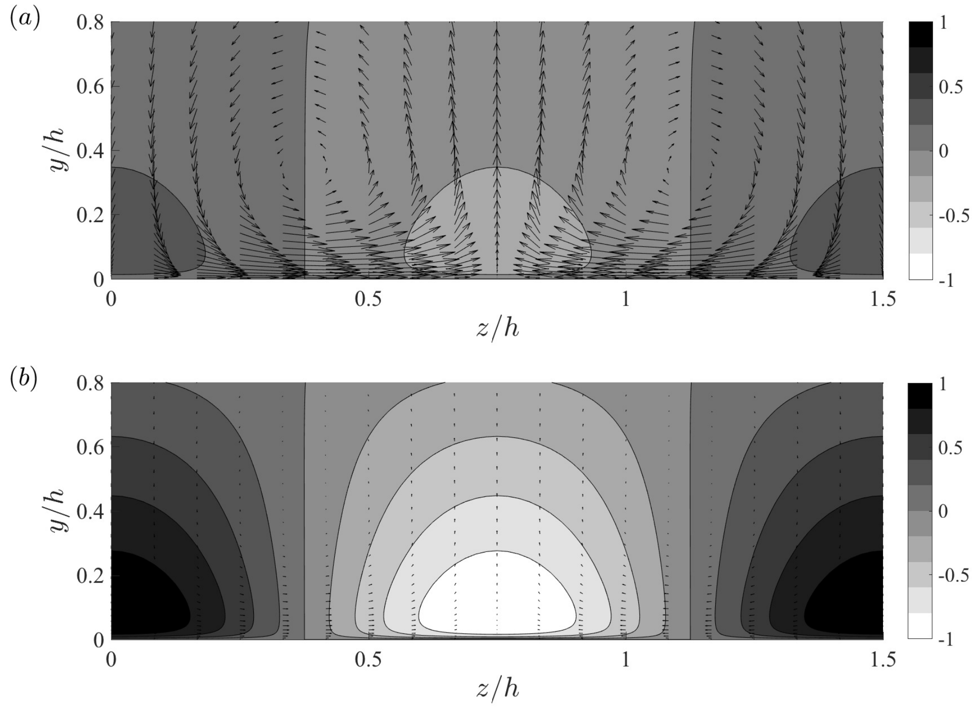

Figure 2.5: Cross-streamwise view of (a) the body forcing $\tilde{\mathbf{f}}(y,z)(=\mathbf{f})$ and (b) the response $\tilde{\mathbf{u}}(y,z)$ with (2.18). The contours indicate the streamwise component, while the vectors indicate the wall-normal and spanwise components. Here, the contour levels in (a) are normalised by the maximum value of the wall-normal component to highlight that the forcing is dominated by the cross-streamwise components (i.e. streamwise vortices), whereas those in (b) are normalised by the maximum value of the streamwise component to show that the response is dominated by the streamwise component (streak). The contours and the vectors in (a) and (b) are plotted with the same scale.

controllable external forcing (e.g. vibrating ribbon). Therefore, $\mathbf{U}_0$ is obtained by an experiment or a numerical simulation without any external forcing, whereas $\tilde{\mathbf{u}}$ is obtained by applying a suitable ensemble (or phase) average to the flow fields in the presence of the given forcing. For this reason, in the absence of any external forcing, $\tilde{\mathbf{u}}$ should become zero, and, in such a circumstance, (2.17) becomes identical to the standard Reynolds decomposition.

Now, we consider a deterministic body forcing $\mathbf{f} = (f_u, f_v, f_w)$ that will be used to drive a streak in the numerical simulation to be performed. We set the mean of the forcing, obtained by averaging in time and in two homogeneous directions, to be zero (see also (2.20b)) so that the forcing can be captured completely by the chosen ensemble average, i.e. $\mathbf{f} = \tilde{\mathbf{f}}$. If the size of $\mathbf{f}$ is small, $\tilde{\mathbf{u}}$ also becomes small. In this case, the following linearised equation for $\tilde{\mathbf{u}}$ is obtained if an appropriate closure is provided to describe the effect of $\mathbf{u}'$ on the evolution of $\tilde{\mathbf{u}}$ (Reynolds & Hussain, 1972):

$$\nabla \cdot \tilde{\mathbf{u}} = 0, \tag{2.18a}$$

$$\frac{\partial \tilde{\mathbf{u}}}{\partial t} + (\mathbf{U}_0 \cdot \nabla)\tilde{\mathbf{u}} + (\tilde{\mathbf{u}} \cdot \nabla)\mathbf{U}_0 = -\frac{1}{\rho}\nabla\tilde{p} + \nabla\cdot[(\nu + \nu_t)(\nabla\tilde{\mathbf{u}} + \nabla\tilde{\mathbf{u}}^T)] + \tilde{\mathbf{f}}, \tag{2.18b}$$

where $\tilde{p}$ is the pressure induced by the forcing and ν_t the eddy viscosity that models the effect of the surrounding turbulence $\mathbf{u}'$ on $\tilde{\mathbf{u}}$. As in previous studies (e.g. Reynolds & Tiederman, 1967), the well-known Cess model is considered for ν_t:

$$\nu_t(\eta) = \frac{\nu}{2}\left\{1 + \frac{\kappa^2 Re_\tau^2}{9}(1-\eta^2)^2(1+2\eta^2)^2 \times 1 - e^{[(|\eta|-1)Re_\tau/A]^2}\right\}^{\frac{1}{2}} - \frac{\nu}{2}, \tag{2.19}$$

where $\eta = (y-1)/h$, $\kappa = 0.426$ and $A = 25.4$ from del Álamo & Jiménez (2006). The mean-velocity profile $U_0(y)$ is subsequently obtained by applying Prandtl's mixing length model to (2.19): $\nu_t dU_0/dy = -\overline{u'v'}$ where the overbar denotes average in time and homogeneous directions. For further details on the profiles of $\nu_t(y)$ and $U_0(y)$, the reader may refer to del Álamo & Jiménez (2006) and Pujals *et al.* (2009).

The body forcing that yields the largest response of (2.18) has been previously computed in Hwang & Cossu (2010*b*). This forcing is given in the form of a counter-rotating vortical motion and it creates a streak by optimally utilising the lift-up effect (see also fig. 2.5). Here, we compute this forcing to drive a streak in the simulation. Given the spatial homogeneity of the mean flow and the eddy viscosity in the streamwise and the spanwise directions, the solution of

(2.18) is written as

$$\tilde{\mathbf{u}}(x,y,z,t) = \hat{\mathbf{u}}(y,t;k_x,k_z)e^{i(k_x x + k_z z)}, \tag{2.20a}$$

where k_x and k_z are the streamwise and spanwise wavenumbers, respectively. The body forcing is also written in the form of

$$\tilde{\mathbf{f}}(x,y,z,t) = \hat{\mathbf{f}}(y,t;k_x,k_z)e^{i(k_x x + k_z z)}. \tag{2.20b}$$

We now assume that the forcing is harmonic in time with a prescribed real frequency ω_f, i.e. $\hat{\mathbf{f}}(y,t) = \hat{\mathbf{f}}_w(y)e^{i\omega_f t}$. Since (2.18) is a linear time-invariant system, its solution becomes $\hat{\mathbf{u}}(y,t) = \hat{\mathbf{u}}_w(y)e^{i\omega_f t}$ after initial transience. Then, the forcing profile leading to the largest response will be computed by solving the following optimisation problem:

$$\max_{\omega_f} \max_{||\hat{\mathbf{f}}_w|| \neq 0} \frac{||\hat{\mathbf{u}}_w||}{||\hat{\mathbf{f}}_w||}, \tag{2.21}$$

where $|| \cdot ||^2 \equiv (1/h) \int_{-h}^{h} (\cdot)^H (\cdot) \, \mathrm{d}y$ and $(\cdot)^H$ indicates the complex conjugate transpose.

The solution procedure of (2.21) typically involves the computation of the 2-norm of the so-called resolvent operator (Schmid & Henningson, 2001). In this study, the optimisation problem (2.21) is solved by repeating the calculation by Hwang & Cossu (2010*b*) using their numerical solver with the same wall-normal resolution.

The present study is concerned with the instability of the low-speed streaks at various scales, and their characteristics are used to select the correct parameters for the computation of the body forcing. Since the mean spanwise spacing of the VLSM in turbulent channel flow was found to be $\lambda_z \simeq 1.5h$ (del Álamo & Jiménez, 2003; Hwang, 2015), the spanwise wavenumber of the forcing is chosen to be $k_z = 2\pi/1.5h$ (this will be used chapter 3). The same logic is applied in the logarithmic layer (see chapter 4), where the spanwise wavenumber of the forcing is equivalent to the mean spacing of the streaks: $k_z = 2\pi/\lambda_z$, with $0.3h < \lambda_z < h$ (Hwang, 2015). Furthermore, we select the streamwise wavenumber to be $k_x = 0$, in order to generate the streamwise-uniform streaky mean flow. For the same reason, the forcing frequency is chosen to be $\omega_f = 0$, thus eliminating one of the optimisation problems in 2.21. We note that, for a given spanwise wavenumber k_z, this choice of k_x and ω_f yields the largest response of $\tilde{\mathbf{u}}$ with (2.18) (see below for further explanation). Also, the streamwise-uniform streaky mean flow allows us to examine all possible streamwise wavelengths of the streak instability.

Fig. 2.5 shows the cross-streamwise view of the computed optimal forcing profile $\tilde{\mathbf{f}}$ and the corresponding response $\tilde{\mathbf{u}}$ of (2.18). The forcing $\tilde{\mathbf{f}}$ is given in the form of a pair of counter-rotating streamwise vortices, and is dominated by the cross-streamwise velocity components (fig. 2.5*a*). On the other hand, the response velocity field $\tilde{\mathbf{u}}$ is dominated by a streaky motion of the streamwise velocity and its cross-streamwise velocity components are much weaker than the streamwise one (fig. 2.5*b*). This indicates that the cross-streamwise components in the forcing are used to amplify the streamwise velocity streak in the response field. This is the so-called 'lift-up' effect, in which the streamwise velocity component is highly amplified by the presence of a small amount of the cross-streamwise velocity components (the wall-normal one in particular).

The lift-up effect can be better understood from the wall-normal velocity and vorticity form of the linearised equation for $\hat{\mathbf{u}}(y,t;k_x,k_z)$: i.e.

$$\begin{aligned} \frac{\partial}{\partial t}\begin{bmatrix} \hat{v} \\ \hat{\omega}_y \end{bmatrix} &= \begin{bmatrix} \Delta^{-1}\mathcal{L}_{\mathcal{OS}} & 0 \\ -ik_zU' & \mathcal{L}_{\mathcal{SQ}} \end{bmatrix}\begin{bmatrix} \hat{v} \\ \hat{\omega}_y \end{bmatrix} \qquad (2.22\text{a}) \\ &+ \begin{bmatrix} -ik_x\Delta^{-1}\mathcal{D} & -k^2\Delta^{-1} & -ik_z\Delta^{-1}\mathcal{D} \\ ik_z & 0 & -ik_x \end{bmatrix}\begin{bmatrix} \hat{f}_x \\ \hat{f}_y \\ \hat{f}_z \end{bmatrix}, \end{aligned}$$

where

$$\mathcal{L}_{\mathcal{OS}} = -ik_x(U\Delta - U'') + \nu_T\Delta^2 + 2\nu_T'\Delta\mathcal{D} + \nu_T''(\mathcal{D}^2 + k^2), \qquad (2.22\text{b})$$

$$\mathcal{L}_{\mathcal{SQ}} = -ik_xU + \nu_T\Delta + \nu_T'\mathcal{D}. \qquad (2.22\text{c})$$

Here, $\hat{\omega}_y$ is the wall-normal vorticity of $\hat{\mathbf{u}}(y,t;k_x,k_z)$, $\nu_T = \nu + \nu_t$, $\Delta = \mathcal{D}^2 - k^2$, $k^2 = k_x^2 + k_z^2$, and $\mathcal{D}$ and $'$ denote $\partial/\partial y$. In (2.22), it is important to note that the equation for $\hat{\omega}_y$ (the Squire equation) is passively coupled with the equation for $\hat{v}$ (the Orr-Sommefeld equation) via the off-diagonal term $-ik_zU'$. Therefore, the energy transfer between the wall-normal velocity and vorticity in (2.22) should always take place from $\hat{v}$ to $\hat{\omega}_y$ (Schmid & Henningson, 2001). Furthermore, it should be noted that, for given $\hat{v}$, the amplification of $\hat{\omega}_y$ is solely governed by the Squire equation. Therefore, the largest amplification by the optimal forcing is expected in the set of streamwise and spanwise wavenumbers which would minimise the effect of dissipation in the Squire equation, while maximising the role of its driving term. In the Squire equation, the effect of dissipation is roughly proportional to $k^2(= k_x^2 + k_z^2)$, whereas the driving term is only proportional to k_z. Therefore, the largest possible amplification by the forcing is expected at $k_x = 0$ and $k_z \simeq O(U'l/\nu_T)$ with l being the length scale of ω_y, as also confirmed by numerous previous studies (e.g. Schmid & Henningson, 2001). In this case, the main energy transfer between the velocity components of the linearised Navier-Stokes equation should be from $\hat{v}$ to $\hat{u}$. This is also why the optimal forcing is featured by large cross-streamwise components and its response is dominated by a large streamwise component (see fig. 2.5).

Finally, it is important to mention that the linearised equation (2.22) does not allow for any mechanism of energy transfer from $\hat{\omega}_y$ (i.e. $\hat{u}$ and $\hat{w}$) to $\hat{v}$ because the equation for $\hat{v}$ is independent of $\hat{\omega}_y$. Such a mechanism is only achieved through the non-linearity of the Navier-Stokes equation. Therefore, describing the dynamics of the wall-normal velocity with this particular kind of linear theory would be physically meaningless and incomplete. We will see that the streak instability mechanism provides a sound explanation for the generation of the wall-normal velocity from the highly amplified streamwise velocity structure (i.e. streak). In this respect, it is also worth mentioning that studying the streak instability mechanism would provide physical insight into design of constant or dynamical modifications of the linearised Navier-Stokes equations around turbulent mean velocity. Therefore, this effect may be modelled by various forms of deterministic and stochastic forcing introduced into the linearised dynamics, as also recently shown by Zare *et al.* (2017).

2.3 Dynamic mode decomposition

Dynamic mode decomposition (DMD) (e.g. Schmid, 2010) is employed to detect the eigenstructure of the streak instability using a set of flow-field snapshots. The DMD is an increasingly popular post-processing technique for analysis of the temporal and spatial evolution of given flow structures of interest. It approximates the flow-field evolution with a finite-dimensional linear time-invariant (LTI) dynamical system. The DMD employed in the present study follows the one proposed by Jovanović *et al.* (2014), and here we only provide a brief summary of their approach.

We consider a sequence of equally time-spaced complex-valued snapshots with a time interval Δt, such that $\psi_n \equiv \psi(n\Delta t)$ where ψ_n is the flow field at $t = n\Delta t$ for $n = 0, 1, 2, ..., N$. If the temporal evolution of the given flow field is assumed to be generated by a discrete-time LTI system, it can be written as

$$\psi_{n+1} = \mathbf{A}\psi_n. \tag{2.23}$$

The snapshots, each composed of M spatial points, are then collected in two ordered matrices $\boldsymbol{\Psi}_0$ and $\boldsymbol{\Psi}_1$, such that

$$\boldsymbol{\Psi}_0 = [\psi_0, \psi_1, \psi_2, \ldots, \psi_{N-1}] \quad \in \mathbb{C}^{M\times N}, \tag{2.24a}$$

$$\boldsymbol{\Psi}_1 = [\psi_1, \psi_2, \psi_3, \ldots, \psi_N] \quad \in \mathbb{C}^{M\times N}. \tag{2.24b}$$

The relation between $\boldsymbol{\Psi}_0$ and $\boldsymbol{\Psi}_1$ is subsequently given by

$$\boldsymbol{\Psi}_1 = \mathbf{A}\boldsymbol{\Psi}_0. \tag{2.25}$$

Here, the matrix $\mathbf{A}$ is a projection of the so-called Koopman operator onto the DMD basis (Korda & Mezić, 2018; Rowley *et al.*, 2009). A DMD is essentially an algorithm that computes eigenvalues and the corresponding eigenmodes (dynamic modes) of $\mathbf{A}$ only using the snapshots ψ_n.

The approximation of $\mathbf{A}$ in this study is made by combining with POD (proper orthogonal decomposition). This approach enables us to robustly implement the DMD, as it prevents mathematically singular construction of the companion matrix of $\mathbf{A}$ from noise and other uncertainties in the snapshots (e.g. small-scale background turbulence in the current study) (Schmid, 2010). The POD is performed with an economy-size singular value decomposition of the snapshot matrix $\boldsymbol{\Psi}_0$, i.e. $\boldsymbol{\Psi}_0 = \mathbf{U}\boldsymbol{\Sigma}\mathbf{V}^H$, where $\boldsymbol{\Sigma} = diag\{\sigma_1, \sigma_2, ..., \sigma_{N_p}\}$ with non-zero real positive singular value σ_m for $m = 1, 2, .., N_p$ ($N_p \leq N$), and $\mathbf{U} \in \mathbb{C}^{M\times N_p}$ and $\mathbf{V} \in \mathbb{C}^{N\times N_p}$ are unitary matrices. Each POD mode is then given by the m-th column vector of $\mathbf{U}$ with the corresponding energy σ_m, and its temporal dynamics are described by the m-th column vector of $\mathbf{V}$. Here, if one is to use only the first r POD modes ($r \leq N_p$), $\boldsymbol{\Psi}_0 \simeq \mathbf{U}_r\boldsymbol{\Sigma}_r\mathbf{V}_r^H$ where $\boldsymbol{\Sigma}_r = diag\{\sigma_1, \sigma_2, ..., \sigma_r\}$, $\mathbf{U}_r \in \mathbb{C}^{M\times r}$ and $\mathbf{V}_r \in \mathbb{C}^{N\times r}$.

Projection of $\mathbf{A}$ onto the subspace of the first r POD modes is then given by

$$\mathbf{S} = \mathbf{U}_r^H\mathbf{A}\mathbf{U}_r = \mathbf{U}_r^H\boldsymbol{\Psi}_1\mathbf{V}_r\boldsymbol{\Sigma}_r^{-1}, \tag{2.26}$$

where $\mathbf{S} \in \mathbb{C}^{r\times r}$. The eigenvalues of $\mathbf{S}$, denoted by μ_j, then approximate some of the leading eigenvalues of $\mathbf{A}$ and the corresponding eigenvectors $\mathbf{y}_j$ construct the dynamic modes from

$$\phi_j = \mathbf{U}_r\mathbf{y}_j. \tag{2.27}$$

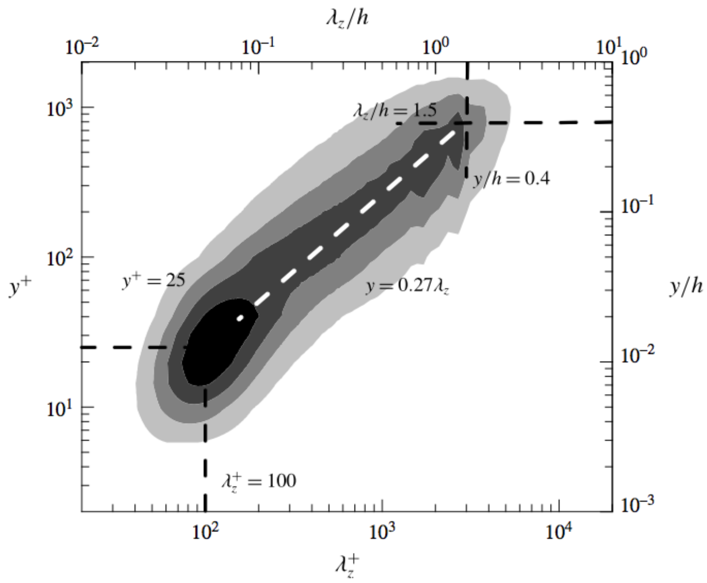

Figure 2.6: Premultiplied spanwise wavenumber spectra of the Reynolds shear stress at $Re_\tau = 2003$ in a turbulent channel flow from Hoyas & Jiménez (2006). The contour labels indicate 0.2, 0.4, 0.6, and 0.8 of the maximum, respectively.

Any snapshot may then be expressed in terms of a series expansion of the dynamic modes, such that:

$$\psi_n \simeq \sum_{j=1}^{r} \alpha_j \mu_j^n \phi_j, \tag{2.28}$$

where α_j is the amplitude of each dynamic mode ϕ_j, which represents its relative contribution. In this study, α_j has been calculated following the standard (non-sparsity-promoting) optimisation procedure in Jovanović *et al.* (2014).

2.4 Assessment of skin-friction generation by self-similar attached eddies

In chapter 5, it will be necessary to evaluate the contribution to skin friction from the coherent structures at different scales. In order to do so, three different methods have been devised, and are introduced in the upcoming sections.

2.4.1 FIK identity with spanwise wavenumber spectra

The first approach is designed to follow the one recently proposed by Deck *et al.* (2014) who combined the streamwise wavenumber spectra of the Reynolds shear stress with the FIK identity (Fukagata *et al.*, 2002) to calculate the contribution of large-scale outer structures to turbulent skin friction. In the present study, we use the spanwise wavenumber spectra unlike the approach of Deck *et al.* (2014), as they are more instructive than the streamwise ones to identify the length scale of the energy-containing motions (Hwang, 2015). Fig. 2.6 shows the spanwise wavenumber spectra of the Reynolds shear stress in a turbulent channel flow at $Re_\tau = 2003$ (Hoyas & Jiménez, 2006). The spectra are well aligned along the ridge given by $y \simeq 0.27\lambda_z$, indicating the linear spanwise scale growth with the distance from the wall. This feature enables us to clearly identify three different length scales of the energy-containing motions in wall-bounded shear flows: the inner ($\lambda_z^+ \simeq 100$), log-layer ($\lambda_z \sim y$) and outer ($\lambda_z \simeq 1.5h$) length scales. The motions at $\lambda_z^+ \simeq 100$ are composed of the near-wall streaks and the quasi-streamwise vortices (Hwang, 2013), whereas the motions at $\lambda_z \simeq 1.5h$ are given with the VLSMs (outer streaky structures) and the LSMs (outer streamwise vortical structures) (Hwang, 2015; Hwang & Cossu, 2010*c*). At the intermediate length scale between $\lambda_z^+ \simeq 100$ and $\lambda_z \simeq 1.5h$, the motions at each λ_z also consist of streamwise vortical structures and streaks, and they are self-similar to one another, forming the behaviour hypothesised by Townsend (1976) (i.e. attached eddy hypothesis). For further details, the reader may refer to Hwang (2015).

For a statistically stationary turbulent channel flow, the FIK identity gives the following relation between the skin friction coefficient and the Reynolds shear stress:

$$C_f = \frac{12}{Re_m} + 12 \int_0^h 2\Big(1 - \frac{y}{h}\Big)\Big(- \frac{\overline{u'v'}}{4U_m^2}\Big)\; dy, \tag{2.29}$$

where U_m is the bulk velocity. Here, the first term represents the contribution of the laminar part and the second term gives the contribution from turbulence. Using one-dimensional spanwise power spectral density $\Phi_{uv}(y;k_z)$, the Reynolds shear stress is written as

$$-\overline{u'v'}(y) = 2 \int_0^\infty \Phi_{uv}(y;k_z)\; dk_z, \tag{2.30}$$

where $k_z(= 2\pi/\lambda_z)$ is the spanwise wavenumber and the overbar denotes average in time and two homogeneous directions. Here, the factor 2 in (2.30) is given to take the contribution of $\Phi_{uv}(y;k_z)$ for $k_z < 0$ into account. Equation (2.30) then enables us to calculate the Reynolds-

Case	Re_m	Re_τ	L_x/h	L_z/h	$N_x \times N_y \times N_z$	Δx^+	Δz^+	Δy_1^+
$M950$	38100	951	3.0	1.5	$96 \times 81 \times 64$	44.6	33.4	1.80
$M2000$	89100	2070	3.0	1.5	$144 \times 129 \times 144$	64.7	32.3	1.45
$M3000$	137500	3042	3.0	1.5	$180 \times 151 \times 180$	76.0	39.1	1.83
$M4000$	193200	4026	3.0	1.5	$288 \times 169 \times 288$	62.9	31.5	1.60

Table 2.1: Simulation parameters of the largest computational domain for the box-confinement approach (before dealiasing).

shear-stress contribution of the motions, the spanwise size λ_z of which is smaller than a given cut-off wavelength $\lambda_{z,t}$, such that:

$$-(\overline{u'v'})_t(y;\lambda_{z,t}) = 2\int_{2\pi/\lambda_{z,t}}^{\infty} \Phi_{uv}(y;k_z)\ dk_z, \tag{2.31}$$

where $(\overline{u'v'})_t$ is the Reynolds shear stress obtained with the spanwise wavenumber spectra for $\lambda_z < \lambda_{z,t}$. Substituting $(\overline{u'v'})_t$ into $\overline{u'v'}$ in (2.29) then leads to

$$C_{f,t}(\lambda_{z,t}) = \frac{12}{Re_m} + 12\int_0^h 2\Big(1-\frac{y}{h}\Big)\Big(-\frac{(\overline{u'v'})_t(y;\lambda_{z,t})}{4U_m^2}\Big)dy, \tag{2.32}$$

yielding the skin-friction coefficient generated by the motions at $\lambda_z \leq \lambda_{z,t}$ and the laminar-flow component: if $\lambda_{z,t} \to 0$, (2.32) yields the skin-friction coefficient given by the corresponding laminar flow. This approach is designed to apply to the existing data obtained by a full scale simulation (DNS by Hoyas & Jiménez, 2006), and quantifies the skin-friction generation by the motions at $\lambda_z \leq \lambda_{z,t}$ in the 'presence of all the motions'. It is also worth being noted that the last term in the right-hand side of (2.32), the key part of this approach, basically evaluates the amount of the Reynolds shear stress at $\lambda_z \leq \lambda_{z,t}$ with a weight $1 - y/h$. Finally, it should be mentioned that this approach is solely based on a post processing of the computed data (i.e. the spanwise wavenumber spectra of Reynolds shear stress). Therefore, the approach does not affect other flow parameters and statistical quantities. We shall refer to this method as the 'FIK-identity-based approach'.

2.4.2 Confining computational domain

The second approach is based on the minimal box technique proposed by Hwang & Cossu (2010*c*, 2011) and Flores & Jiménez (2010) for the structures in the logarithmic and outer regions. The key parameter of this approach is the spanwise size of the computational domain L_z, as setting

$$L_z = \lambda_{z,t}, \tag{2.33}$$

allows one to simulate only the motions at $\lambda_z \leq \lambda_{z,t}$. This approach clearly differs from the FIK-identity-based approach, as it quantifies skin-friction generation by the motions at $\lambda_z \leq \lambda_{z,t}$ in the absence of those at $\lambda_z > \lambda_{z,t}$. This approach was used by Hwang (2013) for the near-wall motions, and revealed that contribution of the near-wall motions to turbulent skin friction decays rapidly with the Reynolds number. In the present study, we further extend this approach by considering an order of magnitude higher Reynolds numbers (up to $Re_\tau \simeq 4000$). The spanwise computational domain is also varied up to the largest spanwise length scale of the motions, $L_z = 1.5h$ (i.e. the spanwise length scale of the LSM and the VLSM).

In this approach, the constraint imposed on the spanwise domain size (2.33) provides the upper limit for the the maximum finite value of λ_z. Nonetheless, the computational domain retains some motions at $\lambda_z > \lambda_{z,t}$ in the form of the spanwise uniform eddy: i.e. the motions at $\lambda_z \to \infty$ ($k_z = 0$). The eddy corresponding to this wavelength could still influence the remaining structures of the flow. In order to assess the influence of this uniform mode, the filter used in Hwang (2013) is also introduced to remove the $k_z = 0$ component of the streamwise and wall-normal velocities. This approach modifies the right-hand side of the momentum equation at each Runge-Kutta substep, such that:

$$\begin{aligned} \widehat{\mathrm{RHS}}_x(y, k_x \neq 0, k_z = 0) = 0, \\ \widehat{\mathrm{RHS}}_y(y, k_x \neq 0, k_z = 0) = 0, \end{aligned} \tag{2.34}$$

where $\widehat{\cdot}$ denotes the Fourier coefficient in the x and z directions, k_x is the streamwise wavenumber, and RHS_x and RHS_y are respectively the right-hand sides of the streamwise and wall-normal components of the discretised momentum equation. More details of this technique, along with a broader discussion on its effects at low Reynolds numbers, can be found in Hwang (2013, 2015). With this technique, we will show that the effect of the spanwise uniform mode to skin friction is very limited (see §5.2.1 and Appendix B.)

It should be noted that, in applying this approach, considering a very long streamwise domain has been found not to be very critical (see also Appendices B.1 and B.2). This appears to be because the long streaky structures in the logarithmic and outer regions are well resolved with the streamwise uniform Fourier component. Indeed, the mean-velocity profile and skin-

Case	Re_m	Re_τ	L_x/h	L_z/h	$N_x \times N_y \times N_z$	Δx^+	Δz^+	Δy_1^+
$W2000$	89100	2044	3.0	3.0	$144 \times 129 \times 288$	63.9	31.9	1.43
$F2000$	89100	2056	12.0	3.0	$576 \times 129 \times 288$	64.3	32.1	1.44

Table 2.2: Parameters of reference simulation for the artificial damping (before dealiasing).

friction coefficient at a given Reynolds number have been found to be well recovered even with $L_x = 3.0h$ and $L_z = 1.5h$, consistent with previous studies (Flores & Jiménez, 2010; Hwang & Cossu, 2011; Lozano-Durán & Jiménez, 2014). A careful examination has further revealed that the change of the streamwise domain yields variation of skin-friction coefficient only within 2% if $L_x > 2L_z$ (Appendix B.1). This amount of deviation is small enough for the given scope of the present study, as the skin friction has been found to vary up to 85% with the designed numerical experiment (e.g. fig. 5.3). This feature also allows us to explore a relatively wide range of the parameter space of Re_m and $\lambda_{z,t}$ without very long streamwise domain sizes. All the computations with this approach are therefore carried out with $L_x = 2L_z$. We note that this aspect ratio is equivalent to the smallest box size allowing for self-sustaining process of the motions at each spanwise length scale L_z (Hwang & Cossu, 2010*c*, 2011), and also well corresponds to the size of the self-similar vortex clusters (del Álamo *et al.*, 2006). Simulation parameters for the biggest computational domain at four different Reynolds numbers are summarised in table 2.1. This method shall be referred to as 'box-confinement approach'.

2.4.3 Artificial damping of the motions

The last approach employed is to compute skin friction drag after eliminating the structures at $\lambda_z > \lambda_{z,t}$ in a sufficiently large computational domain. In this case, the removal of the motions at $\lambda_z > \lambda_{z,t}$ is implemented by introducing an artificial damping in the form of a body forcing to the right-hand side of the Navier-Stokes equation, such that:

$$\frac{\partial \mathbf{u}}{\partial t} + (\mathbf{u} \cdot \nabla)\mathbf{u} = -\frac{1}{\rho}\nabla p + \nu \nabla^2 \mathbf{u} + \mathbf{f}, \tag{2.35}$$

where $\mathbf{u} = (u, v, w)$, t is time, ρ the density of fluid, p the pressure, ν the kinematic viscosity, and $\mathbf{f}$ the introduced body forcing, respectively. To damp the motions at $\lambda_z > \lambda_{z,t}$, $\mathbf{f}$ is set for its Fourier component to satisfy

$$\hat{\mathbf{f}}(y,t;\lambda_x,\lambda_z) = -\mu(\lambda_z)\hat{\mathbf{u}}(y,t;\lambda_x,\lambda_z), \tag{2.36a}$$

with

$$\mu(\lambda_z) = \begin{cases} 0 & \text{for } \lambda_z \le \lambda_{z,t}, \\ \mu_0 & \text{for } \lambda_z > \lambda_{z,t}, \end{cases} \tag{2.36b}$$

where $\hat{\cdot}$ denotes the Fourier coefficient in the x and z directions, and λ_x is the streamwise wavelength. We note that the damping is not applied to zero spanwise wavenumber ($k_z = 0$) to make direct comparison with the result of the box-confinement approach without (2.34). A set of different values of μ_0, ranging from 5.3×10^{-4} to 4.2×10^{-3} have been examined to check the robustness of this approach to the choice of μ_0. The statistics and skin-friction drag are found not to be appreciably dependent on the value of μ_0 considered, and $\mu_0 = 1.4 \times 10^{-3}$ is used throughout the present study. The simulation parameters for this numerical experiment are summarised in table 2.2. Two computational domains are considered: one is with a sufficiently long streamwise domain ($F2000$), and the other is the minimal one for the largest structures ($W2000$). Most of the computations are performed with $W2000$, and a few cases are also verified with $F2000$. We shall call this method 'artificial damping'.

It should finally be noted that the approach damping the spanwise Fourier components for $\lambda_z > \lambda_{z,t}$ has an important difference from the box-confinement approach described in §2.4.2. The box-confinement approach basically excludes the motions at $\lambda_z > \lambda_{z,t}$ by not resolving them except through zero spanwise wavenumber (i.e. $k_z = 0$). This implies that the motions at $\lambda_z \le \lambda_{z,t}$ in a confined computational domain have no way to transfer energy to the motions at $\lambda_z > \lambda_{z,t}$, except through zero spanwise wavenumber ($k_z = 0$). On the contrary, the damping approach allows for such energy transfer, and the transferred energy is damped in the range of the spanwise wavelengths at $\lambda_z > \lambda_{z,t}$. The two methods therefore do not necessary have to yield the same result.

3

Streak instability in the outer layer

3.1 Introduction

Given the ongoing discussion about the formation of the vortical structures in the logarithmic and outer regions, the existence of streak instability and the related streamwise length-scale selection mechanism in 'real' turbulent flows must be examined. In particular, this scenario can provide an explanation of the streamwise length-scale selection of the vortical structures, unlike some previous theories, e.g. the merger/growth of hairpin vortices. The goal of the present study is therefore to demonstrate that the streak instability is the seeding mechanism of the vortical structure in the outer region (i.e. LSM). To this end, we design a numerical experiment that enables us to access the streak instability in a 'real' turbulent flow. We introduce a body forcing, computed with the previous linear theory (Hwang & Cossu, 2010*b*), to drive long streaks in the outer region (i.e. an idealised form of VLSMs). The forcing amplitude is then gradually elevated to examine the emergence of streak instability and the corresponding eigenstructure. To carefully detect the eigenstructure, a dynamic mode decomposition (DMD) (Jovanović *et al.*, 2014; Schmid, 2010) is subsequently employed. From the designed numerical experiment, we will indeed see that sinuous-mode streak instability and the related vortical structure emerge with a streamwise length scale of $\lambda_x \simeq 1 - 5\delta$.

3.2 Results

The designed experiment is carried out with a set of numerical simulations documented in table 3.1. Three different Reynolds numbers are considered, but most of the data presented in this section will be from the numerical simulations at $Re_\tau \simeq 960$ (S960). However, we note that the

Case	Re_m	Re_τ	L_x/h	L_z/h	$N_x \times N_y \times N_z$	Δx^+	Δz^+	Δy_1^+
S490	17800	494	25.0	3.0	$288 \times 81 \times 72$	64.7	32.3	1.45
S960	38100	960	25.0	3.0	$576 \times 81 \times 144$	62.5	33.4	1.80
S2050	89100	2056	12.0	3.0	$576 \times 129 \times 288$	64.3	32.1	1.44

Table 3.1: Simulation parameters of the unforced cases (before dealiasing).

findings at this Reynolds number are qualitatively the same as those at the other two Reynolds numbers (see e.g. §3.2.3). The body forcing computed in §2.2 is implemented in each of the numerical simulations and the forcing amplitude is gradually increased to drive stronger streaks. The forcing amplitude is defined as

$$||\mathbf{f}|| = \sqrt{\frac{2}{V}\int_V \mathbf{f}^H\mathbf{f}\; dV}, \tag{3.1}$$

where V is the total volume of the computational domain. We note that the factor 2 is introduced here to make the norm in (3.1) identical to the one in (2.21) and that $\mathbf{f} = \tilde{\mathbf{f}}$ by the definition of the forcing introduced in §2.2.

Application of the forcing is found to affect friction drag and the related Re_τ. However, for all forcing amplitudes considered, there was no case resulting in any drag reduction, consistent with the recent work by Canton *et al.* (2016). For small forcing amplitudes, the friction Reynolds number Re_τ of the simulations changes very little. However, as the forcing amplitude is increased further, Re_τ increases significantly: see table 3.2 for the case of the S960 simulations. Here, it should be noted that the elevated skin friction is not due to any interaction with structures at smaller length scales in the near-wall and logarithmic regions. In fact, the introduction of the large-amplitude forcing has been found to destroy a significant amount of the structures in these regions (see fig. 3.5). Instead, the increase in skin friction for such large forcing amplitudes appears to be due to direct effect of the forcing on the wall shear stress. This interpretation is consistent with recent findings (Hwang & Bengana, 2016) where the lift-up effect was found to be an important skin-friction generation mechanism of the structures in the logarithmic and outer regions. Indeed, the forcing in the present study, given in the form of counter-rotating vortices (fig. 2.5), is designed to generate a streak by promoting the lift-up effect.

It should finally be mentioned that the main focus of the present study is the comparison of the reference and forced simulations in order to identify the flow structures associated with

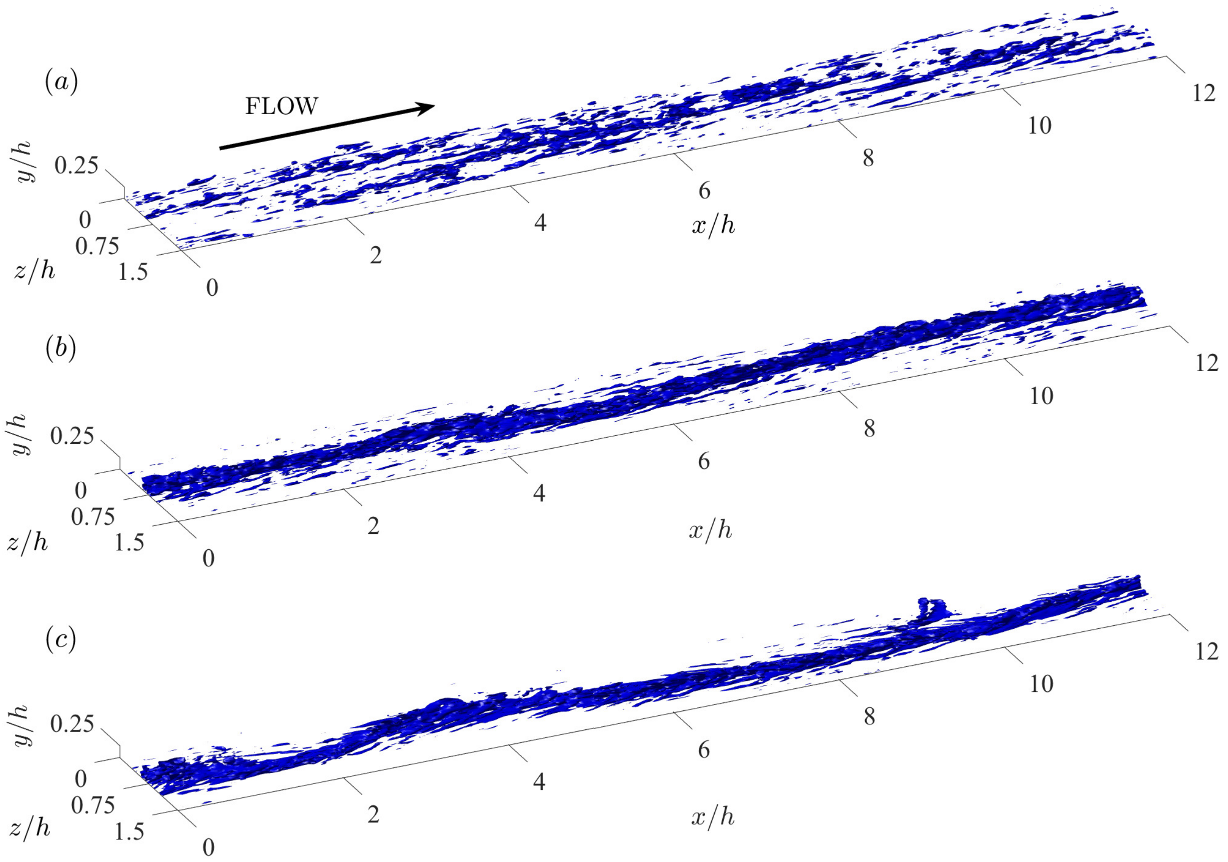

Figure 3.1: Iso-surfaces of instantaneous streamwise velocity ($u'^+ = -3.5$) (S960): (*a*) $||\mathbf{f}h/u^2_{\tau,\mathrm{ref}}|| = 0.31$ ($A^+_s = 1.44$), (*b*) $||\mathbf{f}h/u^2_{\tau,\mathrm{ref}}|| = 0.94$ ($A^+_s = 3.42$), (*c*) $||\mathbf{f}h/u^2_{\tau,\mathrm{ref}}|| = 6.11$ ($A^+_s = 5.30$).

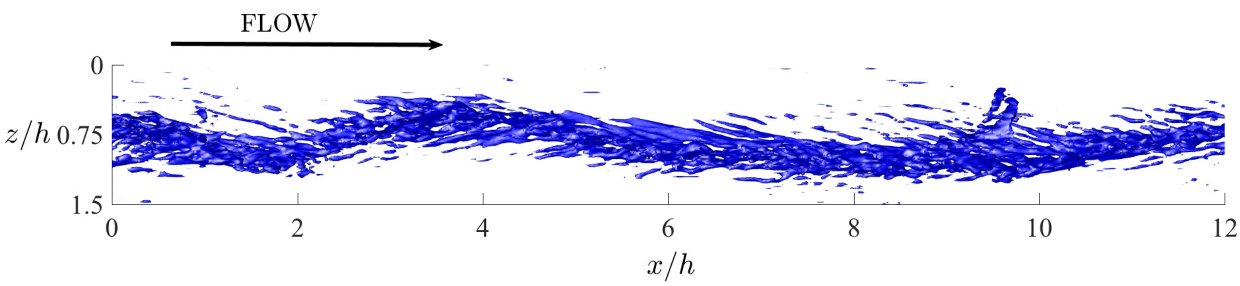

Figure 3.2: Top view of the iso-surfaces of instantaneous streamwise velocity ($u'^+ = -3.5$) in fig. 3.1 (*c*). Here, the flow direction is from left to right.

$\|\mathbf{f}h/u_{\tau,\mathrm{ref}}^2\|$	0	0.11	0.31	0.68	0.94	1.90	3.85	6.11	8.06
Re_τ	960	967	992	1021	1029	1034	1042	1078	1121
$\|\tilde{\mathbf{u}}_s^+\|$	0	0.63	1.90	2.53	2.76	3.00	3.42	3.79	4.04
A_s^+	0	0.54	1.44	2.96	3.42	4.04	4.73	5.30	5.72

Table 3.2: Summary of flow response with respect to the forcing amplitude (S960).

streak instability statistically and dynamically. Therefore, all data from the forced simulations are presented by scaling with the friction velocity of the (unforced) reference simulations, $u_{\tau,\mathrm{ref}}$.

3.2.1 Streak amplification

Fig. 3.1 reports the instantaneous streamwise velocity fluctuation of case S960 on increasing the forcing amplitude. Given the spanwise wavelength of the forcing ($\lambda_z/h = 1.5$), two streaks are driven in our computational domain (see table 3.1). Here, for brevity, we only present half of the spanwise domain. As the forcing amplitude is gradually increased (from fig. 3.1*a* to *c*), a streaky structure covering the entire streamwise domain clearly emerges. It is also interesting to note that the highly amplified streak appears to meander along the streamwise direction (fig. 3.1*c*) and this is clearly seen in fig. 3.2, where a top view of fig. 3.1 (*c*) is given. This meandering behaviour of the driven streak is reminiscent of that reported for VLSMs in a turbulent boundary layer (Hutchins & Marusic, 2007*b*). However, more quantitative discussion of this feature will be deferred to §3.2.2 and §3.2.3.

The streaky structure driven by the body forcing in the numerical simulations is detected statistically using the definition of the triple decomposition in (2.17). Since the applied body forcing is steady and uniform in the streamwise direction, it is evident that the ensemble average in (2.17) is replaced by the average in time and the streamwise direction. The organised wave in a simulation with the forcing is then obtained by

$$\tilde{\mathbf{u}}_s = \langle \mathbf{u} - \mathbf{U}_0 \rangle_{x,t}, \tag{3.2}$$

where the subscript 's' on the left-hand side denotes the organised wave component obtained by a numerical simulation and $\langle\cdot\rangle_{x,t}$ indicates the average in time and in the streamwise direction. We also recall that $\mathbf{U}_0 = (U_0(y), 0, 0)$ is the mean velocity of the reference (unforced) simulation.

The cross-streamwise view of the mean velocity ($\langle \mathbf{u} \rangle_{x,t} = \mathbf{U}_0 + \tilde{\mathbf{u}}_s$) is shown in fig. 3.3 for two different forcing amplitudes. The appearance of a low-velocity region is evident around

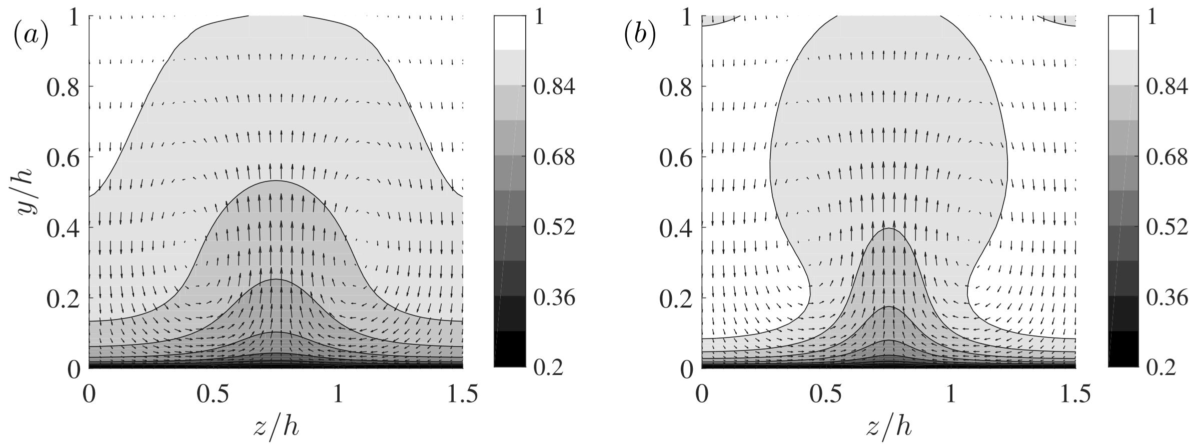

Figure 3.3: Mean cross-stream flow field (S960): (a) $\|\mathbf{f}h/u_{\tau,\mathrm{ref}}^2\| = 0.31$ ($A_s^+ = 1.44$); (b) $\|\mathbf{f}h/u_{\tau,\mathrm{ref}}^2\| = 1.90$ ($A_s^+ = 4.04$). The contours indicate the streamwise velocity, and the arrows represent the wall-normal and spanwise velocities. The contours are normalised by the centreline velocity of each simulation.

$z/h = 0.75$, where the streamwise momentum is expected to be pumped away from the wall by the counter-rotating vortical forcing (see also fig. 2.5). The low-speed region extends along the entire wall-normal location including the logarithmic layer ($0.05 < y/h < 0.2$ at this Reynolds number). Two symmetric high-velocity regions arise both sides of the low-velocity region, where the streamwise momentum is supposed to be brought down to the wall by the forcing. An increase in the forcing amplitude results in the narrower spanwise extent of the low-speed region (compare fig. 3.3a with 3.3b), as was also reported for the near-wall case (Cassinelli *et al.*, 2017). Finally, it should be mentioned that $\tilde{\mathbf{u}}_s$ is dominated by the streamwise velocity: for example, when $||\mathbf{f}h/u_{\tau,\mathrm{ref}}^2|| = 1.91$, the maximum streamwise component of $\tilde{\mathbf{u}}_s$ is $\tilde{u}_{s,max}^+ = 4.76$, while its wall-normal counterpart is only $\tilde{v}_{s,max}^+ = 1.01$ (the superscript '+' denotes scaling in the inner units). This indicates that the formation of the streaky mean flow is a consequence of the lift-up effect, as explained in detail in §2.2.

Using the computed $\tilde{\mathbf{u}}_s$, two quantities are computed to measure the response to the forcing. The first one is the norm of $\tilde{\mathbf{u}}_s$:

$$||\tilde{\mathbf{u}}_s|| = \sqrt{\frac{2}{V}\int_V \tilde{\mathbf{u}}_s^H \tilde{\mathbf{u}}_s \, dV}, \tag{3.3}$$

which represents the kinetic energy of the induced motion averaged over the given computational domain. We note that if the forcing amplitude is small and the eddy viscosity in (2.19) correctly

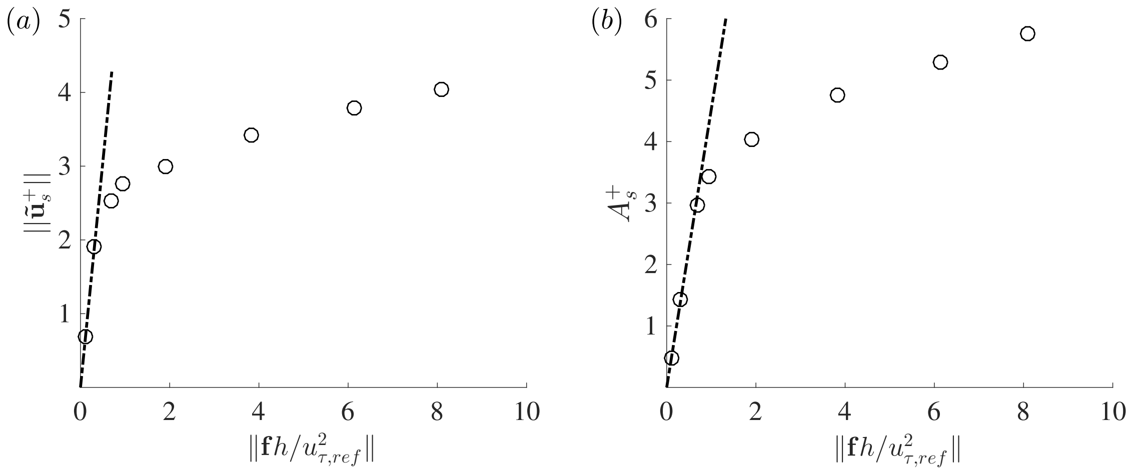

Figure 3.4: Flow response to the forcing (S960): (a) $||\tilde{\mathbf{u}}_s^+||$; ($b$) A_s^+. Here, the definitions of $||\tilde{\mathbf{u}}_s^+||$ and A_s^+ are given in (3.3) and (3.4), respectively.

models the surrounding turbulence, $\tilde{\mathbf{u}}_s$ from (3.2) would be identical to $\tilde{\mathbf{u}}$ from the linear model (2.18). Although, in practice, this is unlikely to happen due to the crude nature of the eddy-viscosity model, computation of $||\tilde{\mathbf{u}}_s||$ as in (3.3) would be useful to assess the linear model (2.18), enabling the quantitative comparison of the amplification by the forcing in a real turbulent flow with that in the linear model (2.18). The second measure of the response to the forcing is chosen to be the streak amplitude and is defined as

$$A_s^+ = \frac{1}{2}\Big(\max_{y,z} \big[\tilde{u}_s^+(y,z)\big] - \min_{y,z} \big[\tilde{u}_s^+(y,z)\big] \Big), \tag{3.4}$$

where $\tilde{u}_s^+$ is the streamwise component of $\tilde{\mathbf{u}}_s$. This definition follows that used in a laminar boundary layer and previous studies (Alizard, 2015; Andersson *et al.*, 2001; Cassinelli *et al.*, 2017; Park *et al.*, 2011).

The evolution of the two quantities on increasing the forcing amplitude is shown in fig. 3.4. As expected, both $\|\tilde{\mathbf{u}}_s^+\|$ and A_s^+ increase linearly with $\|\mathbf{f}\|$ at small forcing amplitudes (i.e. $\|\mathbf{f}h/u^2_{\tau,\mathrm{ref}}\| \lesssim 0.5$), although we should stress that there are just two or three points that belong to the linear regime. We note that the existence of a linear regime for very small values of the forcing amplitude is essentially consistent with previous findings by Russo & Luchini (2016). The linear fit is found to follow $\|\tilde{\mathbf{u}}_s^+\|/\|\mathbf{f}h/u^2_{\tau,\mathrm{ref}}\| \simeq 6.2$. This value is fairly close to $\|\tilde{\mathbf{u}}^+\|/\|\tilde{\mathbf{f}}h/u_\tau^2\| = 4.0$ obtained with the linear theory based on (2.18) (note that $\mathbf{f} = \tilde{\mathbf{f}}$), suggesting that the eddy viscosity in (2.19) is reasonably a good approximation (see also §3.3.4).

When the forcing amplitude is large enough, neither $\|\tilde{\mathbf{u}}_s^+\|$ nor A_s^+ increase linearly anymore, showing a non-linear behaviour. The largest forcing amplitude considered for the S960 case is $\|\mathbf{f}h/u_{\tau,\mathrm{ref}}^2\| = 8.09$. However, as we shall see in §3.3.1, this forcing amplitude is too high to study the physical processes in a natural unforced flow. Therefore, forcing amplitude greater than this value is not considered.

3.2.2 Streak instability: spectra and rms

Now, we investigate the emergence of other flow structures from the driven streamwise-uniform streaks. The focus of this section is given to the detection of wall-normal and spanwise velocity fluctuations at $1 < \lambda_x/h < 5$, as this is the main statistical feature of LSMs (Hwang, 2015). All velocity spectra analysed in this section have been normalised using the friction velocity of the reference (unforced) simulation. Fig. 3.5 shows the evolution of the streamwise wavenumber spectra of the wall-normal velocity, as the streak (and forcing) amplitude is increased. In the absence of any forcing (fig. 3.5*a*), the spectra are well aligned along the linear ridge $y = 0.35\lambda_x$, as pointed out by Hwang (2015). At the top end of the linear edge (i.e. $y/h \geq 0.4 - 0.6$), the spectra show their peak at $\lambda_x/h \simeq 1 - 2$, as in other direct numerical simulations (e.g. Hoyas & Jiménez, 2006). Although this streamwise wavelength is a little shorter than $\lambda_x/h \simeq 3 - 4$ observed in the streamwise velocity spectra (Monty *et al.*, 2009), it is evident that this part would correspond to LSMs, given its wall-normal location and streamwise wavelength. Application of the forcing is found to significantly change the wall-normal velocity spectra. Even at fairly small forcing amplitudes (figs 3.5*b*, *c*), the spectral intensity around the channel centre for $\lambda_x/h \simeq 1 - 2$ is slightly elevated compared to the unforced case (fig. 3.5*a*). As the forcing amplitude is further increased, the spectra reveal a well-manifested peak at $\lambda_x/h \simeq 1 - 2h$ and $y/h \geq 0.4 - 0.6$, consistent with the location of LSMs (figs 3.5*d*,*e*). At excessively large forcing amplitudes (figs 3.5*f*-*h*), excitation at larger streamwise length scales is observed. However, the excited streamwise wavelength does not exceed $\lambda_x/h \simeq 10$ at least for $A_s^+ < 5$ (fig. 3.5*g*).

Through the elevation of the forcing amplitude, it has been consistently observed that the forcing significantly affects the structures at smaller length scales in the near-wall and logarithmic regions. Indeed, the increase in the forcing amplitude gradually reduces the activity in the logarithmic region (figs 3.5*b*-*e*), significantly weakening even the near-wall processes eventually (figs 3.5*f*-*h*). It is not clear yet why the application of such a body forcing significantly inhibits the processes at smaller scales in the near-wall and logarithmic regions. However, this feature reminds us of the suppression of the near-wall process, previously observed when a large-scale

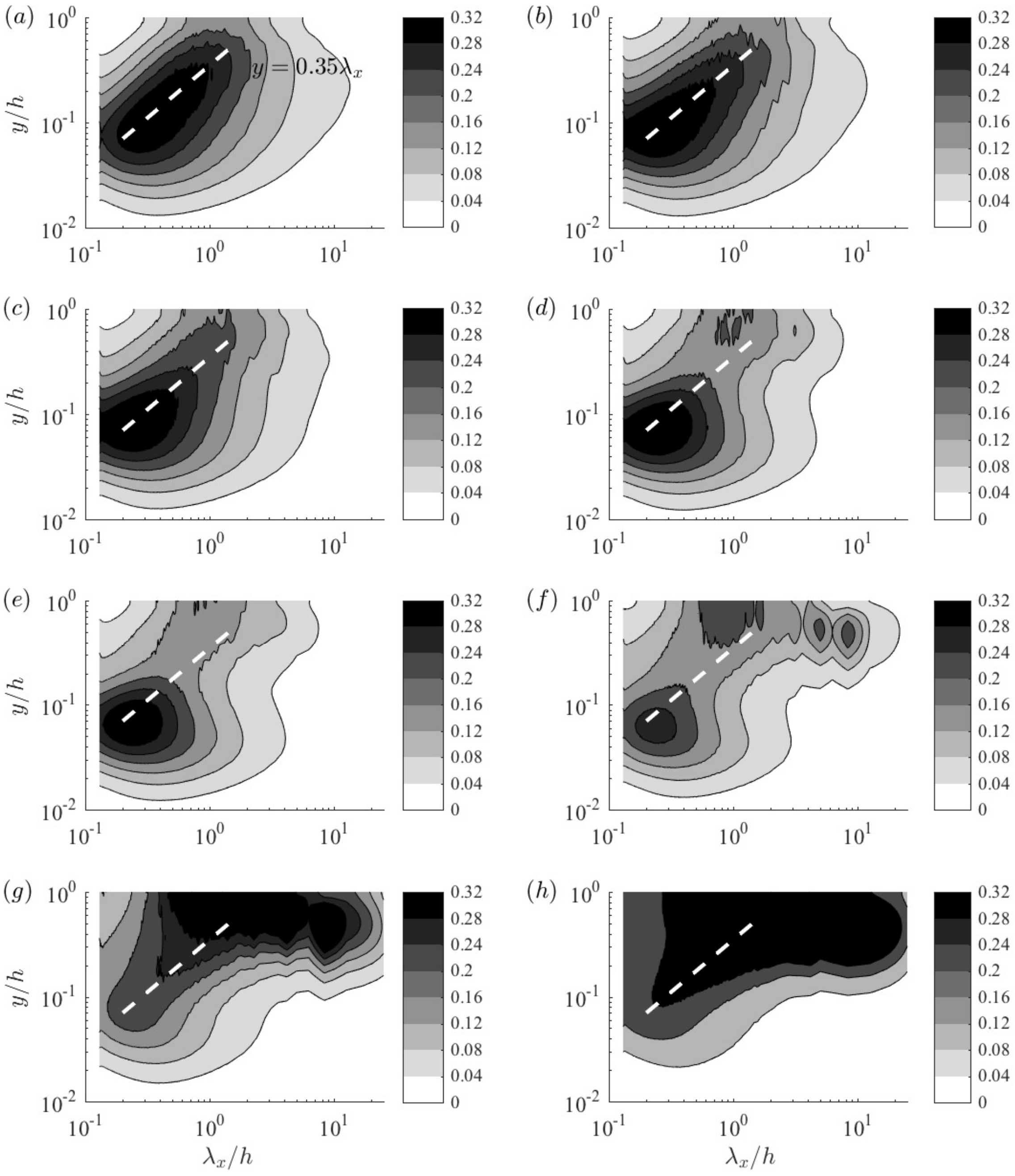

Figure 3.5: Premultiplied streamwise wavenumber spectra of wall-normal velocity (S960). (*a*) $A_s^+ = 0$ (unforced); (*b*) $A_s^+ = 0.54$; (*c*) $A_s^+ = 1.44$; (*d*) $A_s^+ = 2.96$; (*e*) $A_s^+ = 3.42$; (*f*) $A_s^+ = 4.04$; (*g*) $A_s^+ = 4.76$; (*h*) $A_s^+ = 5.30$. Here, the thick white dashed line indicates $y = 0.35\lambda_x$.

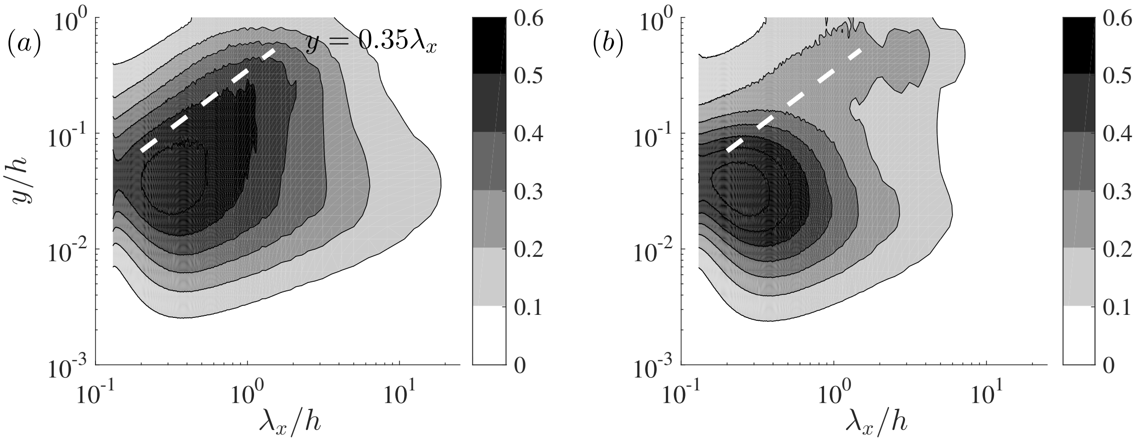

Figure 3.6: Premultiplied streamwise wavenumber spectra of spanwise velocity (S960): (a) $A_s^+ = 0$ (unforced); (b) $A_s^+ = 3.42$. Here, the thick white dashed line indicates $y = 0.35\lambda_x$.

counter-rotating vortical body forcing is applied at low Reynolds numbers (Canton *et al.*, 2016; Schoppa & Hussain, 1998; Willis *et al.*, 2010). Indeed, the inhibition of the structures at smaller scales in fig. 3.5 is consistent with previous observations. However, in the present study, the suppression of the near-wall and logarithmic regions did not yield any skin-friction reduction, unlike previous studies at low Reynolds numbers. This is because the forcing itself has elevated the skin-friction generation process at the scale of the applied forcing via the enhanced lift-up effect (see also the discussion in §3.2.1). Finally, we note that the observed suppression of the processes at smaller scales is clearly due to an interaction of the forcing with other scales. Therefore, further discussion on this issue is beyond the scope of the present study.

The dependence of the spanwise velocity spectra on increasing the forcing amplitude has also been found to be qualitatively the same as that of the wall-normal velocity spectra. Fig. 3.6 shows the streamwise wavenumber spectra of the spanwise velocity for the unforced and forced cases. Similar to the wall-normal velocity spectra, the forcing resulting in $A_s^+ \simeq 3-4$ excites the spectral intensity at $\lambda_x/h \simeq 1-2$ and $y/h \geq 0.4-0.6$, while weakening the activity of the structures in the near-wall and logarithmic regions.

The observation made with figs 3.5 and 3.6 suggests that an intense cross-streamwise velocity structure at $\lambda_x/h \simeq 1-2$ is excited at low amplitudes of the body forcing. It is important to remember that the applied forcing is uniform in the streamwise direction ($\lambda_x = \infty$), thus this cross-streamwise velocity structure at a finite streamwise length scale should not be the direct outcome of the forcing. Instead, it suggests that another physical mechanism is at play in the generation of this structure. In this respect, it is encouraging to compare the observed streamwise wavelength of the cross-streamwise velocity structure with that of the streak instability in the previous theoretical analysis. The stability analysis using an eddy-viscosity model (Park *et al.*, 2011) predicted that a streaky base flow with $\lambda_z/h = 4$ becomes unstable at $\lambda_x/h \simeq 3-6$. At first glance, this prediction does not seem to match well with $\lambda_x/h \simeq 1-2$ in the present numerical experiment. However, the spanwise spacing of the streak in the present study is $\lambda_x/h \simeq 1.5$, considerably smaller than $\lambda_z/h = 4$ in Park *et al.* (2011). Indeed, a recent extension of the theoretical analysis to smaller spanwise wavelengths showed that there exists a self-similar relation between the spanwise wavelength of the imposed streak and the streamwise wavelength of its instability (Alizard, 2015). If this is adopted, a streak at $\lambda_z/h \simeq 1.5$ would become unstable at $\lambda_x/h \simeq 1.13-2.25$, showing a fairly good agreement with $\lambda_x/h \simeq 1-2$ observed in the present study.

Further evidence of the streak instability mechanism is found in the cross-streamwise view of the velocity fluctuations in fig. 3.7, where the left and right columns visualise the unforced and forced cases, respectively. We remind the reader that the streaky mean flow shows an even symmetry about $z/h = 0.75$ (fig. 3.3) and that the eigenstructure of a sinuous-mode streak instability is mathematically defined by odd symmetry of the streamwise and wall-normal velocities and by even symmetry of the spanwise velocity about this axis (see e.g. Andersson *et al.*, 2001): i.e.

$$\begin{aligned} \check{u}(y,z^*) &= -\check{u}(y,-z^*), \\ \check{v}(y,z^*) &= -\check{v}(y,-z^*), \\ \check{w}(y,z^*) &= \check{w}(y,-z^*), \end{aligned} \tag{3.5}$$

with $z^* = z - 0.75h$. Here, $\check{\mathbf{u}}(y,z^*) = (\check{u},\check{v},\check{w})$ is the eigenfunction of the streak instability, and the instability mode in physical space is constructed as $\check{\mathbf{u}}(y,z^*)e^{ik_{x,m}x}$ ($k_{x,m}$ is the streamwise wavenumber of the instability). Given the mathematical definition, the streamwise and wall-normal velocity fluctuations solely from the sinuous-mode instability should be zero along $z/h = 0.75$ and the spanwise velocity fluctuation is supposed to have a local maximum/minimum along this axis. Therefore, in the presence of background turbulence, the streamwise and wall-normal velocity fluctuations of the sinuous-mode instability would always show a local minimum along $z/h = 0.75$, while the spanwise one should exhibit a local maximum/minimum along this axis. These features indeed appear in the computed cross-streamwise view of turbulent velocity

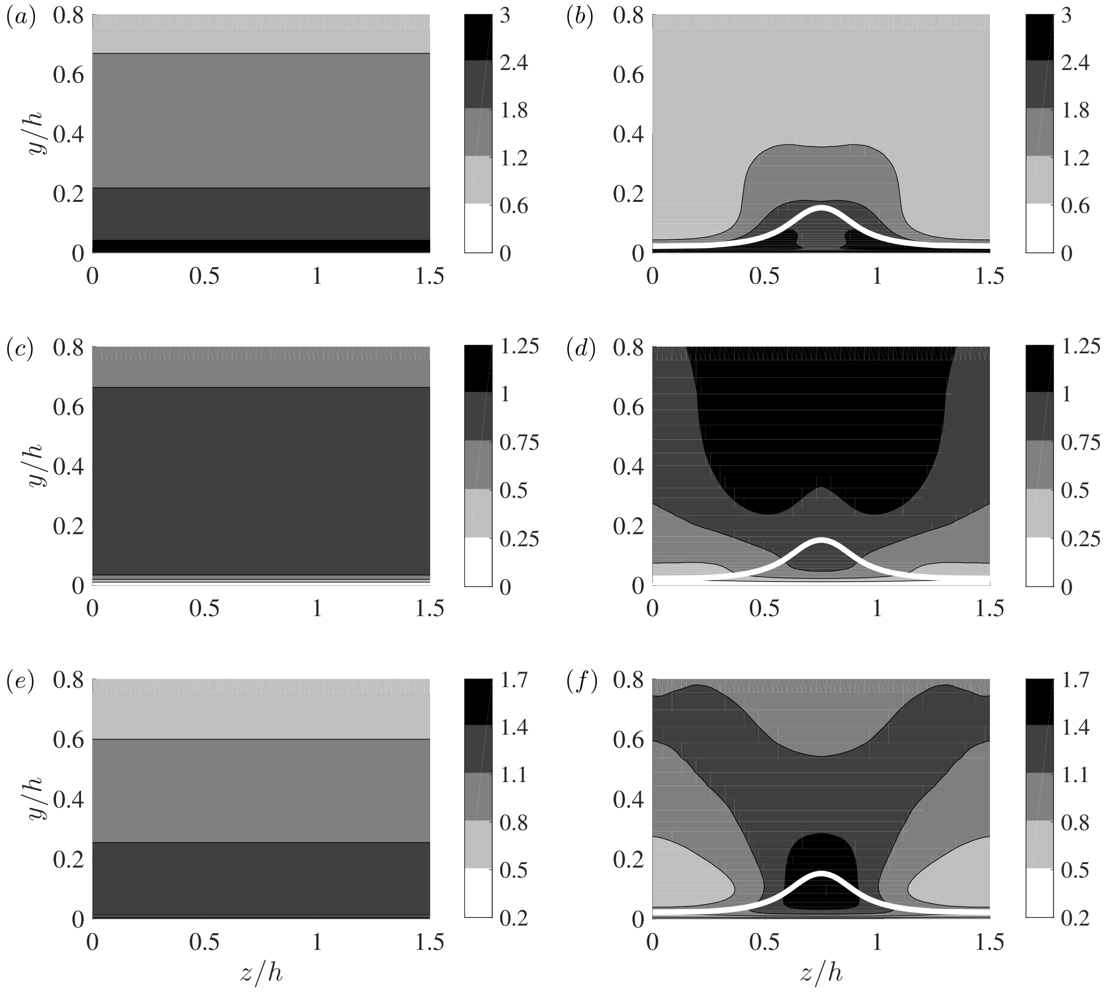

Figure 3.7: Cross-streamwise view of the rms of the velocities for (a, c, e) $A_s^+ = 0$ and (b, d, f) $A_s^+ = 3.42$ (S960): (a,b) streamwise velocity; (c,d) wall-normal velocity; (e,f) spanwise velocity. The thick white line indicates the location where the cross-streamwise mean velocity is $0.9U_c$ (U_c is the centreline velocity of the simulation).

fluctuations in fig. 3.7: both the streamwise and wall-normal velocity fluctuations exhibit two symmetric peaks with a local minimum given along $z = 0.75h$ (figs 3.7*b*,*d*), while the spanwise one shows a local maximum along $z/h = 0.75$ (fig. 3.7*f*). We also note that the cross-streamwise view of the velocity fluctuations is qualitatively the same as the one in a laminar boundary layer (Andersson *et al.*, 2001), indicating the presence of a sinuous-mode instability. In §3.2.3, we will provide further evidence of the sinuous-mode instability by visualising the most energetic DMD mode (see fig. 3.11).

3.2.3 Dynamic mode decomposition

A DMD is performed to examine the flow structure in detail. For the snapshots of the DMD, a time series of a specific Fourier component of the velocity field in the lower half of the wall-normal domain is taken from the simulation with a sufficiently large streak amplitude. Since we are here interested in the effect of the amplified streak, the spanwise wavenumber is chosen to be the same as that of the forcing ($k_z = 2\pi/\lambda_z$ with $\lambda_z/h = 1.5$), while a range of different streamwise wavenumbers ($k_x = 2\pi/\lambda_x$) are considered ($2 < \lambda_x/h < 5$). For given k_z and k_x, each snapshot is constructed such that:

$$\bar{\mathbf{u}}(y, z; k_x) = \hat{\mathbf{u}}(y; k_x, k_z)e^{ik_z z} + \hat{\mathbf{u}}(y; k_x, -k_z)e^{-ik_z z}. \tag{3.6}$$

We note that $\bar{\mathbf{u}}(y, z; k_x)$ is the streamwise Fourier component given only with $\pm k_z$ spanwise Fourier components. The DMD modes and the corresponding eigenvalues μ_j are then computed following the procedure in §2.3. The time interval, the number of POD modes and the number of snapshots for the DMD are carefully chosen to ensure good temporal resolution of large-scale dynamics: $\Delta t u_\tau/h = 0.009$, $r = 30$ and $N = 1000$ (see Appendix A for a detailed discussion on the choice of parameters). Once the DMD is performed, the associated angular frequency is computed by taking the real part of $\omega_j = \mathrm{i} \ln \mu_j/\Delta t$. Since the snapshot in (3.6) represents a streamwise Fourier component, the downstream propagating speed of the DMD mode is computed by

$$c_j = \frac{\omega_j}{k_x}, \tag{3.7}$$

where c_j is the phase speed of the j-th DMD mode. The relative amplitude α_j of all of the DMD modes is finally determined (see also §2.3).

The DMD result of the S960 simulation is shown in fig. 3.8 for $\lambda_x/h = 3.57$ and $A_s^+ = 3.42$. The DMD modes are deemed to be neutral, given that the eigenvalues μ_j sit well on

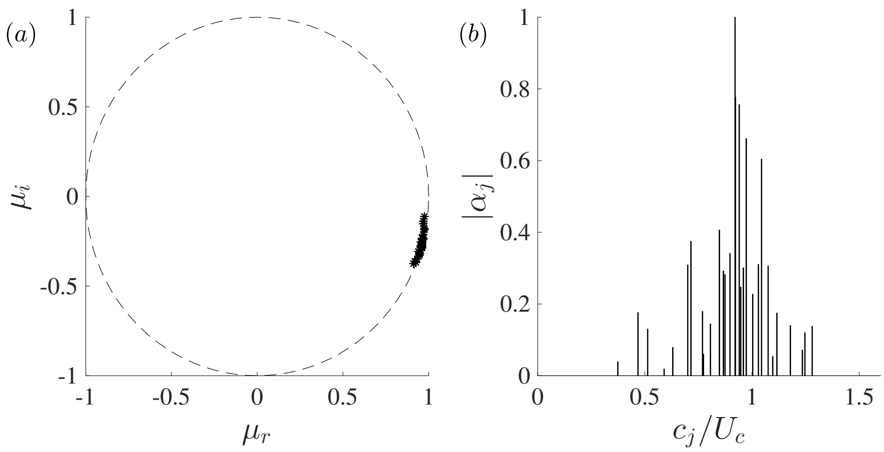

Figure 3.8: DMD analysis with $\lambda_x = 3.57h$ for $A_s^+ = 3.42$ (S960): (a) eigenspectra in the μ_r-μ_i plane; (b) mode amplitude $|\alpha_j|$ with phase speed c_j (the mode amplitude is normalised by the largest one).

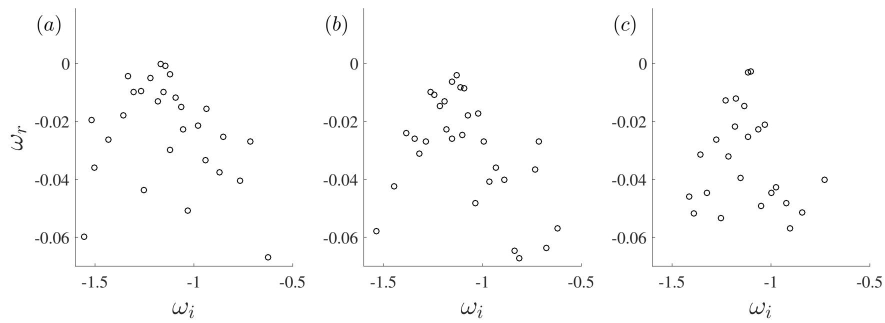

Figure 3.9: DMD analysis with $\lambda_x = 3.57h$, eigenspectra in the ω_r-ω_i plane; (a) $A_s^+ = 4.11$ (S490); (b) $A_s^+ = 3.42$ (S960); (c) $A_s^+ = 3.77$ (S2050).

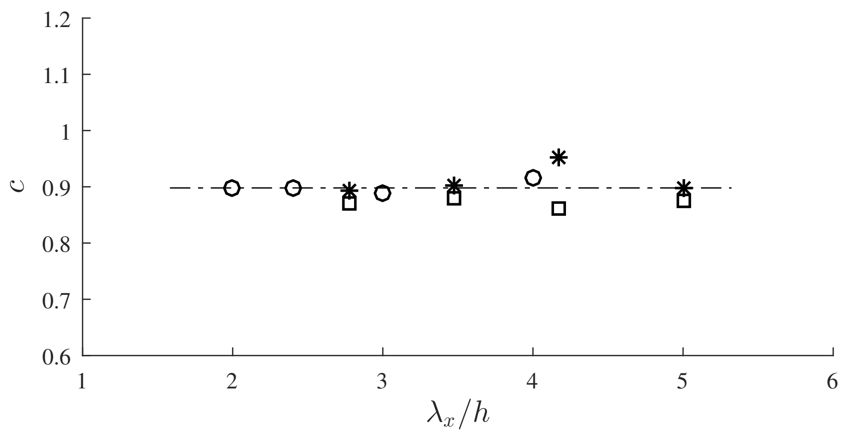

Figure 3.10: Variation of phase speed (c/U_c) with streamwise wavelength: □, $A_s^+ = 4.11$ (S490), ∗, $A_s^+ = 4.04$ (S960); ∘, $A_s^+ = 3.77$ (S2050). Here, the horizontal line indicates $c = 0.9U_c$.

the unit circle (fig. 3.8*a*). This also indicates that the snapshots are indeed collected from a statistically stationary flow with a good resolution. Their asymmetry is due to the processing of complex-valued snapshots instead of real-valued ones. Using (3.7), the computed eigenvalues are subsequently transformed to the phase speed of the DMD modes. The contribution of each DMD mode is then assessed by computing its amplitude α_j, as shown in fig. 3.8(*b*). The phase speed of the DMD modes appears mainly in the range of $0.7 \lesssim c/U_c \lesssim 1.1$ (U_c is the centreline velocity of each simulation), and, in particular, the most energetic DMD mode exhibits $c/U_c \simeq 0.9$. The unpacked eigenspectra at different Reynolds numbers are reported in 3.9.

It is important to mention that the computed phase speed of the most energetic DMD mode is found to not significantly depend on the streamwise wavelength and the Reynolds number, as long as the streak amplitude is chosen to be $A_s^+ > 3$. We also anticipate that it is not due to the wall-normal distribution of the body forcing, since we observe no significant variation even with a very different forcing profile (see §3.3.4). Fig. 3.10 shows the phase speed of the most energetic DMD mode with respect to the streamwise wavelength for all the considered Reynolds numbers. It appears that the most energetic DMD mode, for different streamwise lengths and Reynolds numbers, robustly exhibits $c/U_c \simeq 0.9$. This suggests that the propagation speed of the flow structure generated by the streak instability scales well with the centreline velocity, consistent with del Álamo & Jiménez (2009) who showed the outer scaling of the propagation speed of large-scale structures.

Finally, the most energetic DMD mode is examined. Fig. 3.11 (*a*) and (*b*) show the streaky

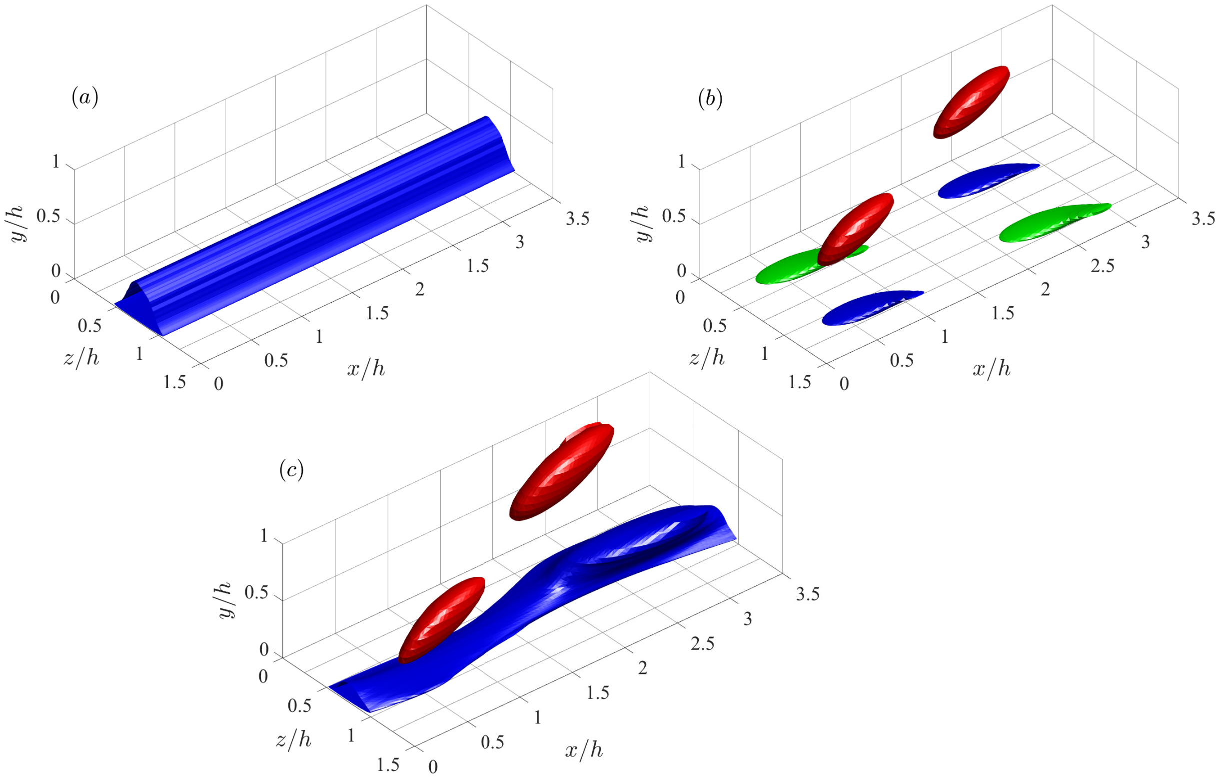

Figure 3.11: Visualisation of the streak instability using the most energetic DMD mode from the S960 simulation ($\lambda_x/h = 3.73$ and $A_s^+ = 4.73$): (a) the low-speed streak with $u'_s = -0.03U_c$ ($u'_s \equiv u_s(y,z) - \langle u_s(y,z)\rangle_z$ where $\langle\cdot\rangle_z$ denotes average in the spanwise direction); (b) the DMD mode $\mathbf{u}_{dmd}$ where the green iso-surfaces are a positive streamwise velocity ($0.8\,\max[u_{dmd}]$), the blue ones a negative streamwise velocity ($u = 0.8\,\min[u_{dmd}]$), and the red ones a negative wall-normal velocity ($v = 0.8\,\min[v_{dmd}]$); (c) the low-speed streak with the DMD mode ($\mathbf{u}_s - \langle\mathbf{u}_s\rangle_z + \gamma\mathbf{u}_{dmd}$ where γ is an appropriate tuning constant for visualisation). In (c), the blue iso-surface indicates a negative streamwise velocity, while the red ones indicate a negative wall-normal velocity.

uniform mean flow and the most energetic DMD mode for $\lambda_x/h = 3.73$, respectively, and their combination is given in fig. 3.11 (*c*). Fig. 3.11 (*c*) clearly reveals that the structure is composed of a streamwise meandering low-speed streak (blue isosurface in fig. 3.11*c*) and a streamwise-alternating pattern of wall-normal velocity structures (red iso-surface in fig. 3.11*c*). We note that this is a robust feature of the computed DMD mode and it does not significantly depend upon the choice of the DMD parameters, such as the streamwise wavelength λ_x, the number of snapshots N, and the number of POD modes r. Therefore, the spatial structure of the DMD mode in fig. 3.11 clearly indicates that the flow structure with an intense cross-streamwise turbulent kinetic energy in §3.2.2 is directly linked to the sinuous-mode streak instability. In this respect, it is finally worth mentioning that the structure of the most energetic DMD mode with the streaky mean flow highly resembles the general form of the travelling-wave solutions in Hwang *et al.* (2016), which is a mathematical representation of the self-sustaining process.

3.3 Discussion

Thus far, we have explored the instability mechanism of an 'amplified' streak in the outer region (VLSM) and its mode as the initiating physical process of LSMs. A body forcing, designed to drive an infinitely long streak (Hwang & Cossu, 2010*a*), is implemented in a set of numerical simulations. As the forcing amplitude is increased, a long streaky structure, which resembles a VLSM, emerges. It is shown that the presence of such a long streaky structure in the outer region generates an intense cross-streamwise velocity structure at $\lambda_x/h \simeq 1-2$, and this streamwise length scale shows good agreement with that predicted by the previous stability analysis (Alizard, 2015; Park *et al.*, 2011). The cross-streamwise view of the turbulence statistics has also revealed that this structure has features mathematically consistent with the sinuous-mode streak instability. Finally, a DMD analysis shows that this structure is characterised by a streamwise meandering motion of the driven streak and alternating cross-streamwise velocity structures, supporting the concept that the cross-streamwise velocity structure at $\lambda_x/h \simeq 1-2$ is a consequence of the sinuous-mode streak instability.

The present numerical experiment is specifically designed to observe the streak instability, while taking the non-linearity of the governing equation and background turbulence fully into account. This is achieved by artificially driving a streak with the optimal forcing, but we note that this does not allow the driven streak to break down. For this reason, in the present numerical experiment, the non-linearly evolved streak instability and the accompanying vortical

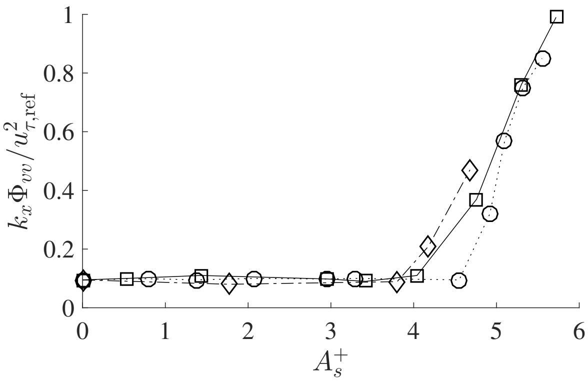

Figure 3.12: Premultiplied streamwise wavenumber spectral intensity of wall-normal velocity with the streak amplitude at $y/h = 0.64$ for $\lambda_x/h = 3.57$: ○, S490; □, S960; ◇, S2050. The maximum amplitude value in an unforced flow is $A_s^+ \approx 4$.

structures coexist. Therefore, with the present numerical experiment alone, it is difficult to precisely explain the causal relation between the streak instability and the vortical structures. However, as we shall see in §3.3.3, the sinuous-mode streak instability essentially originates from the spanwise shear created by the presence of the driven large-amplitude streak. This implies that the streak instability is the seeding mechanism of the vortical structures, and this interpretation is consistent with Hwang & Bengana (2016), where the emergence of the streak instability prior to the vortical structures is clearly identified with the minimal-unit simulation.

In many ways, the flow structure emerging at $\lambda_x/h \simeq 1 - 2$ via the streak instability is remarkably similar to the LSM. Firstly, its streamwise length scale and wall-normal location (figs 3.5 and 3.6) are in good agreement with those of the LSM (Kovasznay, 1970; Monty *et al.*, 2009). Secondly, the structure is mainly featured by intense wall-normal and spanwise turbulent kinetic energy, as the LSM is in a real flow (Hwang, 2015). Thirdly, a series of the cross-streamwise velocity components of this structure are collectively aligned along the low-speed streak (fig. 3.11*c*), consistent with the early view of a VLSM as a concatenation of adjacent LSMs (e.g. Baltzer *et al.*, 2013; Kim & Adrian, 1999). However, it should be mentioned that the present numerical experiment provides a different interpretation of the relation between the LSM and the VLSM: the reason that a VLSM appears as a concatenation of a number of LSMs is because a series of the LSMs are formed along a long VLSM by the streak instability. Lastly, the emergence of the sinuous-mode instability implies that the VLSM would meander along the streamwise direction (figs 3.1 and 3.11), as previously observed in Hutchins & Marusic (2007*b*).

All of these observations suggest that the LSM is initiated by the sinuous-mode instability of the amplified streak in the outer region (VLSM). This interpretation is well integrated into the self-sustaining nature of the large-scale structures composed of VLSMs and LSMs (Hwang, 2015; Hwang & Bengana, 2016; Hwang & Cossu, 2010*c*; Hwang *et al.*, 2016), and is also consistent with the previous theoretical studies on the streak instability (Alizard, 2015; Park *et al.*, 2011). There have been several different propositions on the formation mechanism of the LSM, such as the mergers/growth mechanism (Adrian, 2007; Perry *et al.*, 1986; Zhou *et al.*, 1999) and the Orr mechanism (Jiménez, 2013*a*,*b*). However, it should be stressed that, to the best of our knowledge, only the streak instability mechanism currently explains the streamwise length-scale determination of the LSM among these different propositions.

3.3.1 Emergence of streak instability at large scales

In the near-wall region, it has been shown that the streak instability is subcritical, admitting strong transient growth at low streak amplitudes before the onset of a normal-mode instability (Schoppa & Hussain, 2002). Consistent with this, our recent work has shown that the streak instability and the related near-wall quasi-streamwise vortices at $\lambda_x^+ \simeq 200 - 300$ spontaneously emerge on increasing the streak amplitude (Cassinelli *et al.*, 2017), exhibiting a sensitive response to the initial condition and/or external noise, as is typically observed in a highly non-normal system (Schmid & Henningson, 2001). However, it should also be mentioned that such non-normal growth of the perturbation around a low-amplitude streak is typically an outcome of the interaction with the marginally stable sinuous mode. Therefore, in practice, distinguishing the transient growth from the normal-mode instability is almost impossible at least for near-wall turbulence and for transitional laminar boundary layers, as pointed out by Hoepffner *et al.* (2005).

To carefully examine the emergence of the streak instability in the present numerical experiment, the one-dimensional spectral intensity of the wall-normal velocity for $\lambda_x/h = 3.57$ is plotted in fig. 3.12 against the streak amplitude. For relatively low streak amplitudes ($A_s^+ < 4$), the intensity of the wall-normal velocity is very slightly elevated. However, when the streak amplitude reaches $A_s^+ \simeq 4$, the spectral intensity drastically increases for all the Reynolds numbers considered. This behaviour is very interesting, as it indicates that the onset of a normal-mode instability would be $A_s^+ \simeq 4$. However, this does not imply that the streaky motion in a real flow (VLSM) would experience such a normal-mode instability for $A_s^+ \gtrsim 4$. Firstly, as is evident in fig. 3.12, the typical spectral intensity of the wall-normal velocity in the unforced simulation is much smaller than that observed for $A_s^+ \gtrsim 4$. Secondly, the spectra of the wall-normal velocity

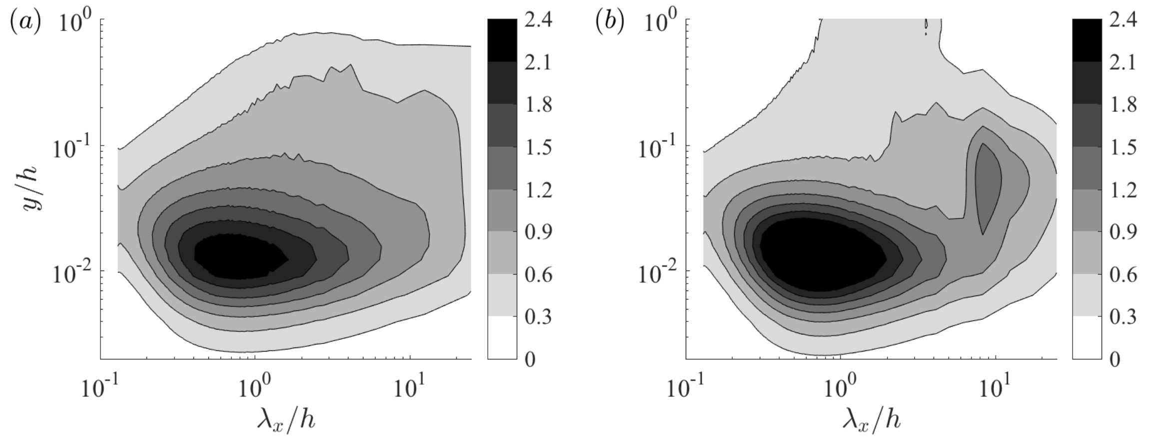

Figure 3.13: Premultiplied streamwise wavenumber spectra of streamwise velocity (S960); (*a*) unforced case; (*b*) $A_s^+ = 4.04$.

in the unforced simulation do not exhibit high intensity for $\lambda_x > 5 - 10h$ in the outer region (fig. 3.5*a*). However, the forced simulations with $A_s^+ \gtrsim 4$ show much higher spectral intensity in this range of the streamwise wavelength (figs 3.5*f*-*h*). Finally, the forced simulations with relatively low streak amplitudes ($A_s^+ \lesssim 4$) are not actually unresponsive to the surrounding perturbations: the wall-normal velocity spectra of the simulations with $3 \lesssim A_s^+ \lesssim 4$ also exhibit a fairly energetic peak at $\lambda_x/h \simeq 1 - 2$ (figs 3.5*d*-*f*), which would be more consistent with the spectra of the unforced reference simulation.

These observations suggest that VLSMs in a real flow are unlikely to reach $A_s^+ \gg 4$ because they should break down quickly with the emergence of the streak instability (Hwang & Bengana, 2016). The streak amplitude would reach at best $A_s^+ \simeq 4$, below which the wall-normal velocity structure is excited primarily at $\lambda_x/h \simeq 1 - 2$. This also indicates that the streak instability process in the outer region may be mainly driven by a non-modal mechanism (secondary transient growth), as that in the near-wall region. Finally, it should be stressed that the wall-normal velocity structure at $\lambda_x/h \simeq 1 - 2$ is the first feature noticeable statistically on increasing the streak amplitude, and it depends very little on the type of body forcing that drives the streak. This issue will be further discussed in §3.3.4.

3.3.2 The streamwise length scale of very large-scale motion

The present numerical experiment also provides important physical insight into the streamwise length scale determination of the VLSM. If the streak amplitude is given by $3 \lesssim A_s^+ \lesssim 4$ just

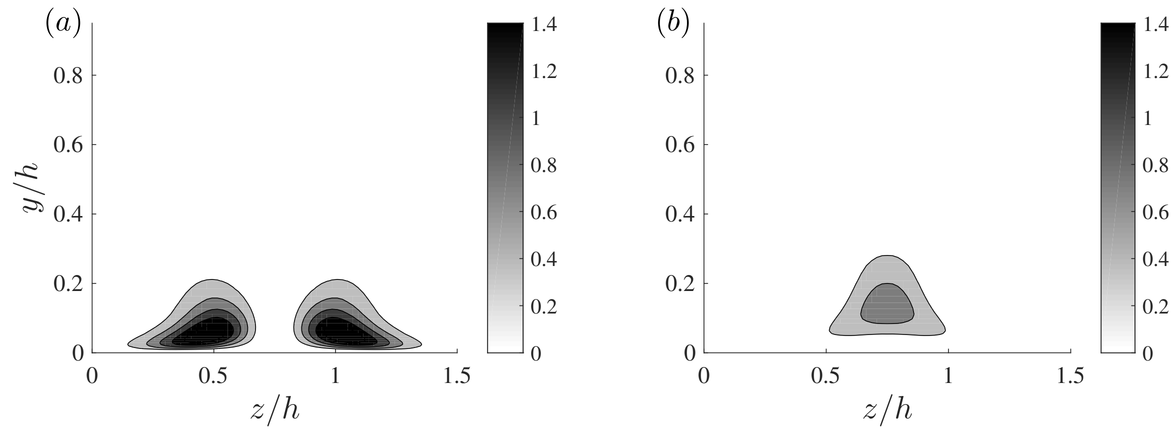

Figure 3.14: Turbulent kinetic-energy production around the streaky mean flow for $A_s^+ = 3.42$ (S960): (a) $-\langle u'w' \rangle_{x,t} \partial \overline{U}^+(y,z)/\partial z$; (b) $-\langle u'v' \rangle_{x,t} \partial \overline{U}^+(y,z)/\partial y$.

before the breakdown phase in the self-sustaining process (see also the discussion in §3.3.1), the largest streamwise wavelength of the wall-normal velocity structure generated by the streak instability mechanism would be limited to $\lambda_x/h \simeq 10-20$ (see figs 3.5d-f). The generated wall-normal velocity structure would then trigger linear amplification of the streaky structures that mainly carry the streamwise turbulent kinetic energy (i.e. lift-up effect). As discussed in §2.2, the largest possible linear amplification of the streaks takes place at infinitely long streamwise wavelength and it generally prefers longer streamwise length for larger amplification (del Álamo & Jiménez, 2006; Cossu *et al.*, 2009; Hwang & Cossu, 2010b; Pujals *et al.*, 2009; Willis *et al.*, 2010). Therefore, the largest admissible streamwise wavelength of the streak instability (i.e. $\lambda_x/h \simeq 10-20$) is expected to determine the streamwise length scale of the VLSM.

This scenario is examined in fig. 3.13, where the streamwise wavenumber spectra of the streamwise velocity for both the unforced and forced simulations are shown. Here, the streak amplitude of the forced simulation is chosen to be $A_s^+ = 4.04$, as the excitation of the wall-normal velocity structure around $\lambda_x/h \simeq 10$ is well visible at this amplitude (see fig. 3.5f). As expected from the wall-normal and spanwise velocity spectra (figs 3.5 and 3.6)), the streamwise velocity spectra of the forced simulation reveal elevated spectral intensity at $\lambda_x/h \simeq 1-2$ and $y/h \gtrsim 0.3$ (fig. 3.13b), the location associated with the LSM (fig. 3.13a). However, in the streamwise velocity spectra of the forced simulation (fig. 3.13b), there exists another more distinct peak at $\lambda_x/h \simeq 10$ throughout the logarithmic layer. Importantly, the wall-normal location and the streamwise wavelength of this peak are very close to those of the VLSM, directly supporting the

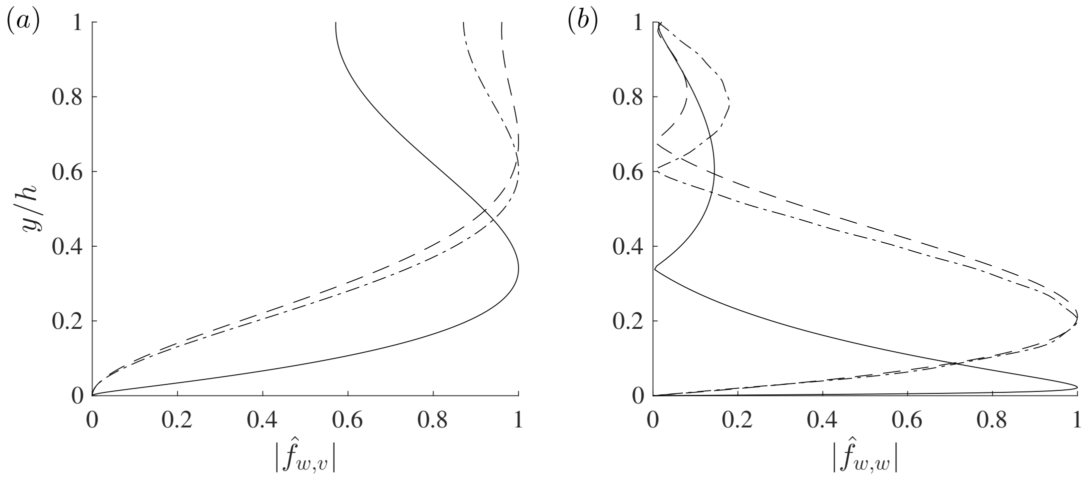

Figure 3.15: The wall-normal profile of the optimal forcing with three different eddy viscosities in (2.18): (*a*) $|\hat{f}_{w,v}|$, (*b*) $|\hat{f}_{w,w}|$. Here, ——, the Cess eddy viscosity ($\nu_t = \nu_t(y)$ in (2.19)); $-\cdot-\cdot-$, a constant eddy viscosity ($\nu_t = \max_y \nu_t(y)$); - - - -, no eddy viscosity ($\nu_t = 0$).

notion that the largest streamwise wavelength of the streak instability determines the streamwise length scale of the VLSM.

3.3.3 Physical mechanism of streak instability

The second-order cross-streamwise statistics and the DMD analysis suggest that the vortical structure at $\lambda_x/h \simeq 1-2$ originates from the sinuous-mode streak instability in the form of a streamwise meandering streak and alternating cross-streamwise velocity components (fig. 3.11*c*). The sinuous-mode instability is understood to be an energy-production process from the spanwise mean shear via the inflectional mechanism (e.g. Park & Huerre, 1995). To investigate this feature of the sinuous-mode instability in the present numerical experiment, turbulent production by the streaky mean flow are further examined in this section. The streaky mean flow is defined as $\overline{U}(y,z) = U_0(y) + \tilde{u}(y,z)$ because the mean flow is dominated by the streamwise component (see the discussion in §3.2.1). Turbulent production around such a mean flow are given by $-\langle u'w'\rangle_{x,t}\partial\overline{U}^+/\partial z$ and $-\langle u'v'\rangle_{x,t}\partial\overline{U}^+/\partial y$; the former indicates production by the spanwise mean shear, while the latter is production by the wall-normal mean shear. The two turbulent kinetic-energy production mechanisms are visualised in fig. 3.14. Production by the spanwise shear appears at either side of the low-speed region at $z/h = 0.75$ (fig. 3.14*a*), whereas that by the wall-normal shear is strong only in the top of the low-speed region (fig. 3.14*b*). In this figure, it

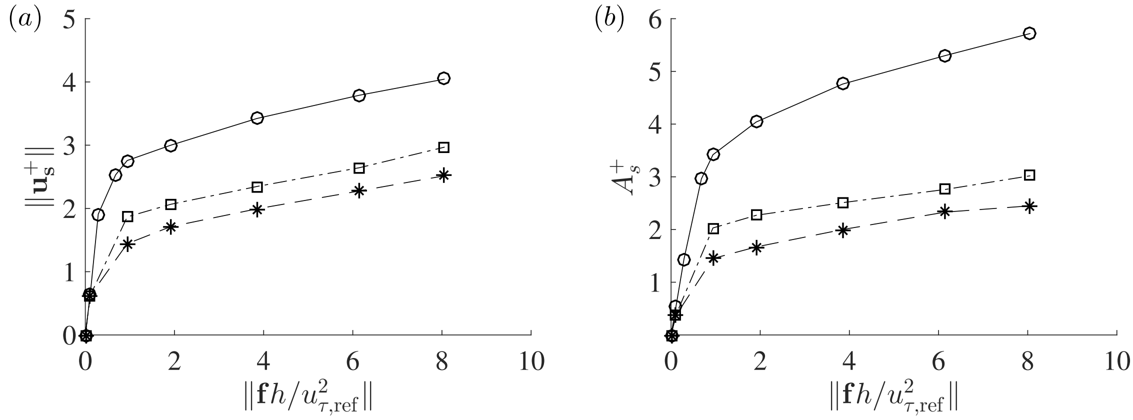

Figure 3.16: Flow response to the forcing (S960): (a) $||\tilde{\mathbf{u}}_s^+||$; ($b$) A_s^+. Here, $\circ$, the Cess eddy viscosity ($\nu_t = \nu_t(y)$ in (2.19)); $*$, no eddy viscosity ($\nu_t = 0$); $\square$, a constant eddy viscosity ($\nu_t = \max_y \nu_t(y)$).

is evident that production by the spanwise shear is much grater than that by wall-normal shear, confirming that the streak instability in the present study is a sinuous mode.

3.3.4 Robustness to the forcing profile

Thus far, the optimal forcing employed in the present study is obtained using the linearised Navier-Stokes equation with the eddy viscosity in (2.19). However, it should be pointed out that this forcing is not the only type of the forcing that can generate a streak. Indeed, the only requirement for body forcing to generate a streak is to contain reasonably strong cross-streamwise components, given the mechanism of the streak formation (i.e. the lift-up effect). In this section, we therefore consider two additional forcing profiles to examine the robustness of the present result: one is the optimal forcing computed without eddy viscosity ($\nu_t = 0$), and the other is obtained by setting $\nu_t = \max_y(\nu_t(y))$. We note that these different eddy viscosities are introduced only for the linear theory in order to generate different types of forcing. Unsurprisingly, the optimal forcing with the two different eddy viscosities are also found to consist of a pair of counter-rotating streamwise vortices (not shown; see also the discussion in §2.2). However, as shown in fig. 3.15, their wall-normal profiles significantly differ from that of the original optimal forcing. While the wall-normal profiles of the two new forcings are not very different from each other, they have much larger values in the location much further from the wall: indeed, the wall-normal component of the two forcings show a maximum at $y/h \simeq 0.6$, whereas the optimal forcing with the original Cess viscosity exhibits its peak at a location much closer to the wall, $y/h \simeq 0.35$.

The response to the three different types of the forcing was then examined, as reported in fig. 3.16. While all the three forcings are found to robustly generate the streaky motion (not shown; see also the discussion in §2.2), the optimal forcing obtained with the Cess eddy viscosity gives rise to a significantly larger response of the streamwise velocity component. This implies that the linearised Navier-Stokes equation with the Cess eddy viscosity provides a much better description of the linear process in a real turbulent flow than the other two cases with different eddy viscosities. This also suggests that the streaky motion generated by the optimal forcing with the Cess eddy viscosity would be the closest to the one in a real flow, because it implies that such a streaky motion can be most easily generated by the non-linear term.

Here, it should be stressed that this interesting behaviour originates from an important physical feature of the Cess eddy viscosity, which satisfies the following mixing length hypothesis:

$$\nu_t \frac{dU}{dy} = -\overline{u'v'}. \tag{3.8}$$

In the logarithmic region, $dU/dy \sim 1/y$ and the Reynolds shear stress is approximately constant. Therefore, the considered $\nu_t(y)$ should grow linearly with y in the logarithmic region according to (3.8). It should be pointed out that this tendency of ν_t must be generic in any turbulence model for wall-bounded shear flows. In the near-wall region, both the integral and dissipation length scales are the inner length scale ν/u_τ, indicating that the dissipation process should be dominated by the molecular viscosity. On the other hand, in the outer region, the integral length scale (h) is largely separated from the dissipation length scale ($(\nu^3 h/u_\tau^3)^{1/4}$), and this length-scale separation is given by the ratio of the integral scale to the dissipation scale, i.e. $Re_\tau^{3/4}$. Therefore, in the outer region, the energy dissipation takes place through the Richardson-Kolmogorov cascade, requiring large ν_t from the modelling viewpoint. In the logarithmic region, the only way to smoothly connect the two very different dissipation mechanisms in the near-wall and outer regions is by having monotonically increasing ν_t in the wall-normal direction, as reflected in (3.8). This behaviour of ν_t explains why the optimal forcing obtained with the Cess eddy viscosity has large values in the region close to the wall – the large value of the forcing should generate a large response due to the small eddy viscosity in this region. It has been recently shown that this behaviour of ν_t is essential for understanding the scaling of coherent structures in the logarithmic and outer regions (Hwang, 2016): for example, the Reynolds-

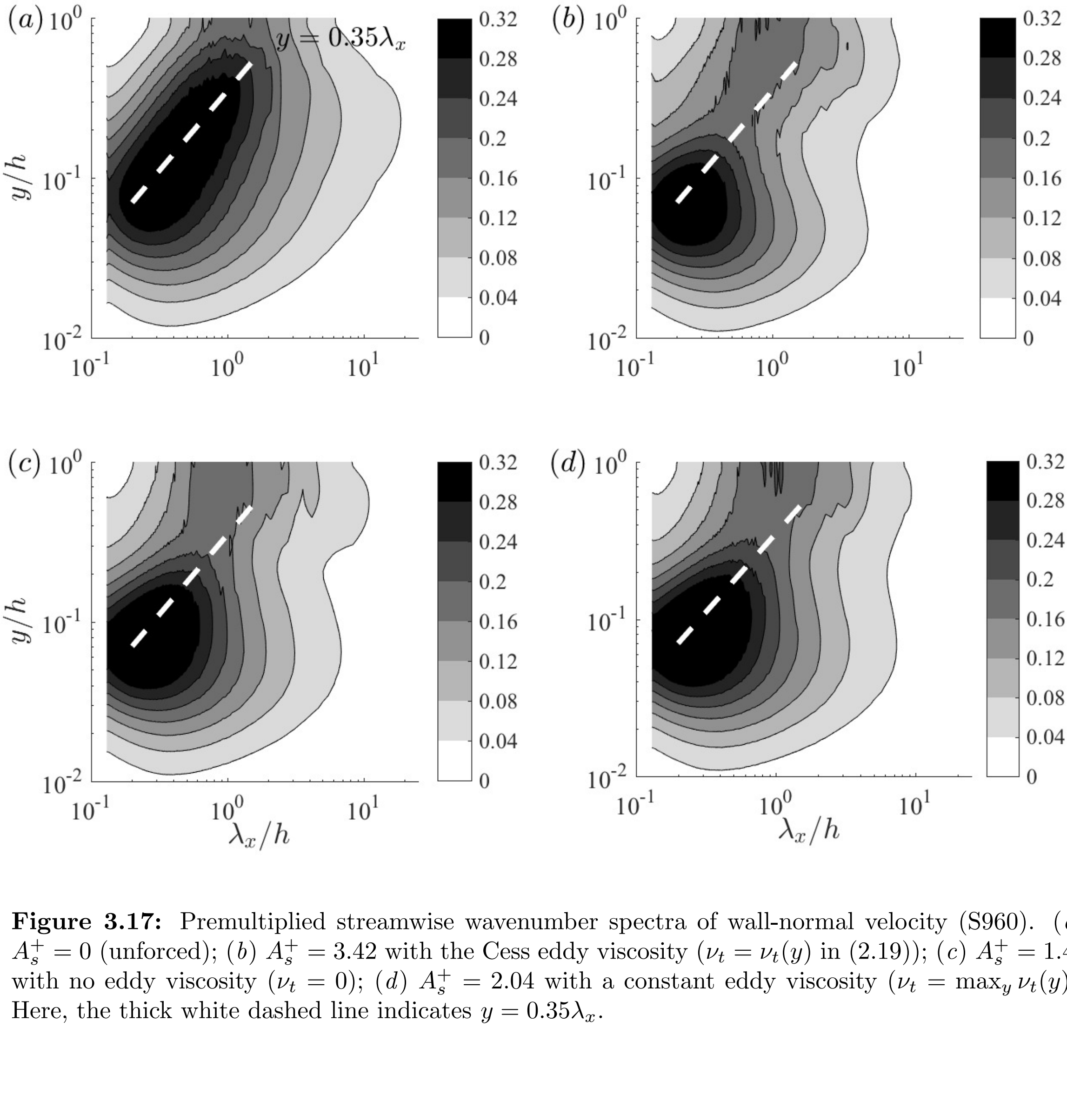

Figure 3.17: Premultiplied streamwise wavenumber spectra of wall-normal velocity (S960). (a) $A_s^+ = 0$ (unforced); (b) $A_s^+ = 3.42$ with the Cess eddy viscosity ($\nu_t = \nu_t(y)$ in (2.19)); (c) $A_s^+ = 1.47$ with no eddy viscosity ($\nu_t = 0$); (d) $A_s^+ = 2.04$ with a constant eddy viscosity ($\nu_t = \max_y \nu_t(y)$). Here, the thick white dashed line indicates $y = 0.35\lambda_x$.

number-dependent scaling of the peak wall-normal location of streamwise turbulence intensity, the near-wall penetration of the large-scale outer structures, and the incomplete self-similarity of the streamwise and spanwise velocity components of the coherent structures in the logarithmic region.

By applying the three different types of optimal forcing in fig. 3.16 to a numerical simulation, the sensitivity of the streak instability was finally examined. Fig. 3.17 shows the streamwise wavenumber spectra of the wall-normal velocity when each of the three optimal forcings just begins to exhibit streak instability. Here, the forcing amplitude follows the definition of (3.1), and the corresponding responses are evaluated using (3.3) and (3.4). Despite the difference in the forcing profiles shown in fig. 3.15, the streamwise wavenumber spectra of the wall-normal velocity reveal that the energetic vortical structures at $\lambda_x \simeq 1 - 2h$ in the outer region emerge in all the three cases (figs 3.17*b*,*c*,*d*). This clearly indicates that the streak instability is a very robust physical process that depends very little on the type of the forcing, as long as the forcing is kept to generate an amplified streak in the outer region.

4

Streak instability in the logarithmic layer

4.1 Introduction

Recent studies have unearthed the underlying similarities between the logarithmic and outer layers: the coherent structures that reside in both regions appear to be almost equivalent, and a self-sustaining mechanism has been shown to be at the very heart of their existence. Given the important results obtained in the previous chapter, the logical progression is to examine whether the streak instability should be considered the seeding mechanism for the vortical structures in the logarithmic layer. We therefore follow an approach broadly analogous to chapter 3, but now the forcing profile is designed to amplify the logarithmic streak. Specifically, we use the spanwise spacing of the streaks to characterise their size, following the concept of self-similar attached eddies. The forcing profile is then computed to generate the largest amplification of the structures at a given spanwise wavenumber $\lambda_{z,f}$, in the range $0.3h < \lambda_{z,f} < h$. Indeed, it is found that the amplification of the logarithmic streaks corresponds to the emergence of more energetic cross-streamwise structures, and that their streamwise length-scale depends on the spacing of the streak.

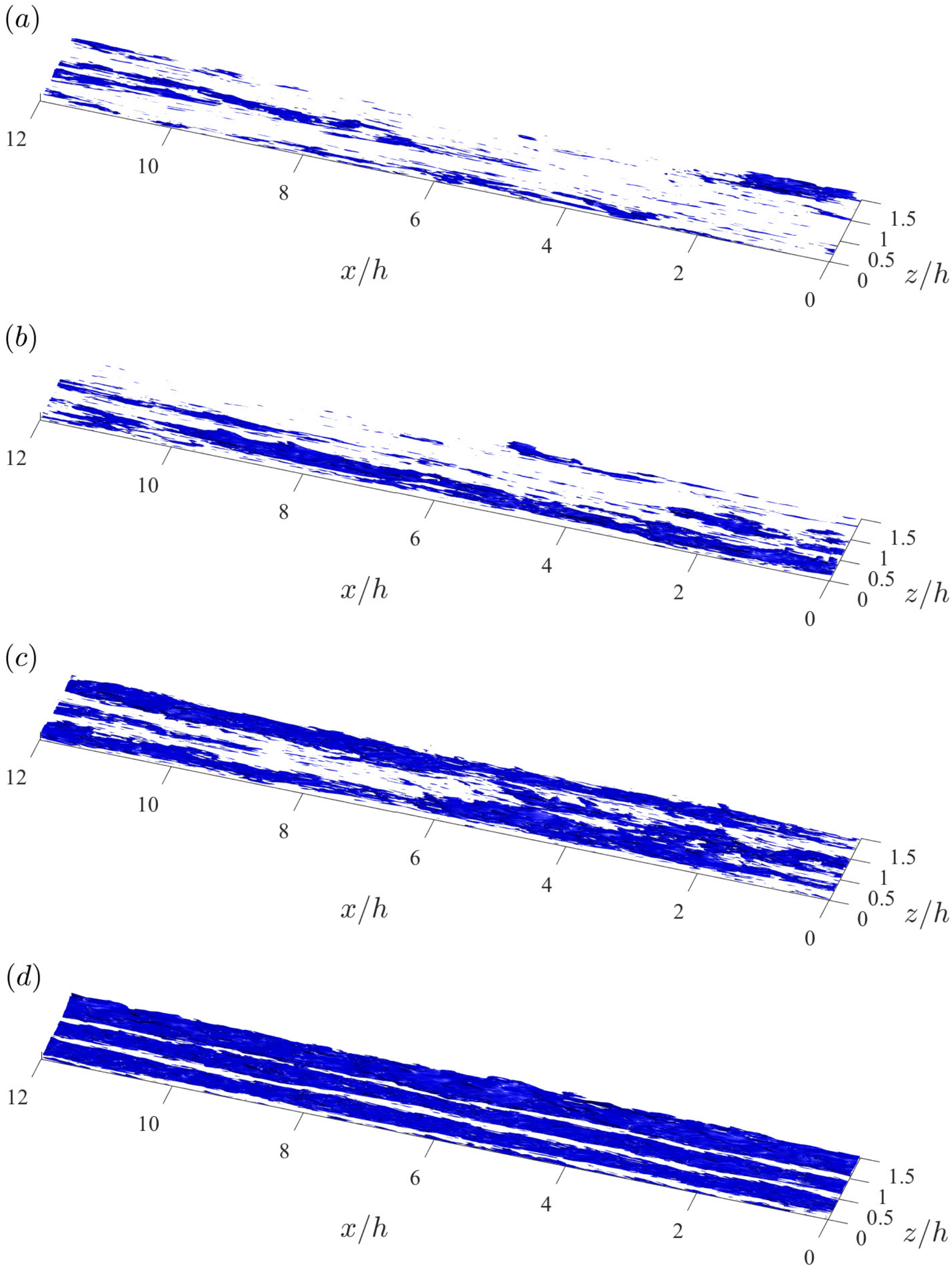

Figure 4.1: Instantaneous fluctuations of streamwise velocity ($u'^{+} = -3.2$) for $\lambda_{z,f} = 0.5h$. (*a*) $A_s^+ = 0.48$; (*b*) $A_s^+ = 1.61$; (*c*) $A_s^+ = 2.03$; (*d*) $A_s^+ = 3.11$.

$Case$	Re_m	Re_τ	L_x/h	L_z/h	$N_x \times N_y \times N_z$	Δx^+	Δz^+	Δy_1^+
S490	17800	494	25.0	3.0	$288 \times 81 \times 72$	64.7	32.3	1.45
S960	38100	960	25.0	3.0	$576 \times 81 \times 144$	62.5	33.4	1.80
S2050	89100	2056	12.0	3.0	$576 \times 129 \times 288$	64.3	32.1	1.44

Table 4.1: Simulation parameters of the unforced cases (before dealiasing).

4.2 Results

4.2.1 Streak amplification

The numerical experiment is performed at $\mathrm{Re}_\tau \approx 500, 1000, 2000$, as documented in table 4.1. The optimal forcing profile has been computed for the four spanwise wavelengths mentioned earlier, and it is subsequently applied to the flow. The forcing amplitude is defined as

$$||\mathbf{f}|| = \sqrt{\frac{2}{V}\int_V \mathbf{f}^H \mathbf{f}\ dV}, \tag{4.1}$$

where V is the total volume of the computational domain. It is worth mentioning that, on application of the forcing, no drag reduction has been found throughout all the parameters considered, similarly to what previously observed for the outer-layer structures. Instead, the skin friction has been found to increase at large forcing amplitudes. This effect is deemed to be due to the shape of the optimal forcing profile which magnifies the lift-up effect, a critical mechanism of the drag production (Hwang & Bengana, 2016). Finally, to highlight the change of the flow field by the forcing, the data from the simulations with the forcing are presented by scaling with the friction velocity of the unforced simulation. Throughout the entire paper, the corresponding inner scaling is denoted by the superscript $^+$.

First, we present the result for $\lambda_{z,f} = 0.5h$ at $\mathrm{Re}_\tau \approx 2000$. The primary outcome expected from the application of the forcing is the appearance of amplified streamwise streaks, as shown in the instantaneous fields of streamwise velocity fluctuation in fig. 4.1. As the forcing amplitude is increased, the emergence of highly amplified streaky structures becomes more evident. To statistically measure the change of the flow field by the amplified streaks, the mean velocity is calculated by taking average in time and in the streamwise direction: i.e.

$$\mathbf{U}(y,z) = \mathbf{U}_0(y) + \tilde{\mathbf{u}}_s(y,z), \tag{4.2a}$$

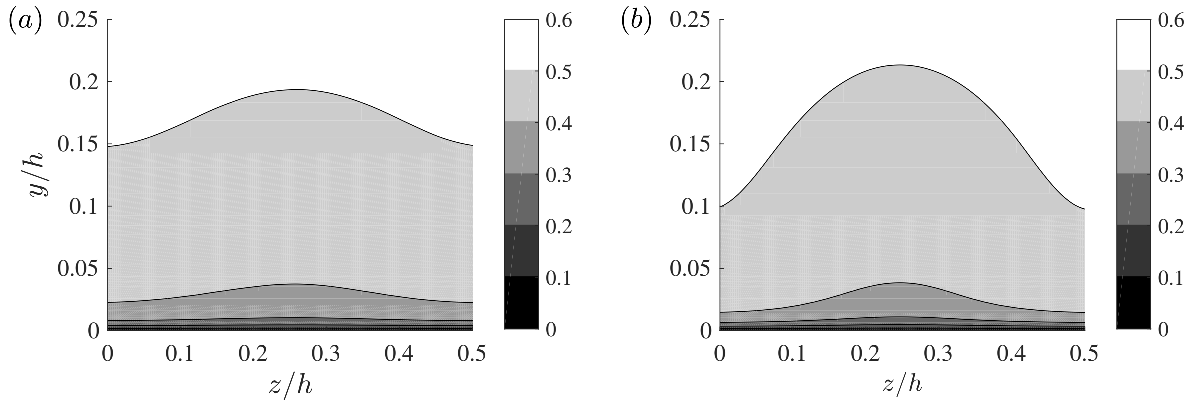

Figure 4.2: Streamwise velocity field of the streaky mean flow $U(y,z)$ for $\lambda_{z,f} = 0.5h$ (S2050): (*a*) $\|\mathbf{f}h/u^2_{\tau,\mathrm{ref}}\| = 0.67$ ($A^+_s = 1.61$); (*b*) $\|\mathbf{f}h/u^2_{\tau,\mathrm{ref}}\| = 0.93$ ($A^+_s = 2.03$). Here, the contour levels are normalised by the centreline velocity of each case.

with

$$\tilde{\mathbf{u}}_s(y,z) = \langle \mathbf{u} - \mathbf{U}_0 \rangle_{x,t}, \tag{4.2b}$$

where $\mathbf{U}_0(y)$ is the mean velocity of the unforced simulation, and $\langle \cdot \rangle_{x,t}$ indicates the average in streamwise direction and time. We now note that $\tilde{\mathbf{u}}_s(y,z)$ becomes the organised wave directly computed from simulations using the given average, and the subscript s here is introduced to indicate its calculation method (i.e. simulation).

The cross-streamwise profile of the computed streaky mean flow is shown in fig. 4.2. Since the forcing profile has been computed to amplify structures characterised by $\lambda_z = 0.5h$, we expect the low-speed streak to be centred around $z = 0.25h$. Two symmetric high-velocity regions arise both sides of this low-velocity region and they are centred around $z = 0$ and $z = 0.5h$ due to the spanwise periodic nature of forcing. An increase in the forcing amplitude results in narrower spanwise extent of the low-speed region (compare fig. 4.2*a* with 4.2*b*), consistent with (Cassinelli *et al.*, 2017). Finally, it should be mentioned that $\tilde{\mathbf{u}}_s$ is dominated by the streamwise velocity, as it is the outcome of the lift-up effect.

Once the mean velocity is calculated, the amplification of the streaks can be statistically quantified. For the sake of consistency, we recur to the two same two quantities defined and employed in the previous chapter (equations 3.3 and 3.4), which definition is here repeated for clarity. One is the norm of $\mathbf{u}_s$,

$$||\tilde{\mathbf{u}}_s|| = \sqrt{\frac{2}{V}\int_V \tilde{\mathbf{u}}_s^H \tilde{\mathbf{u}}_s \, dV}, \tag{4.3}$$

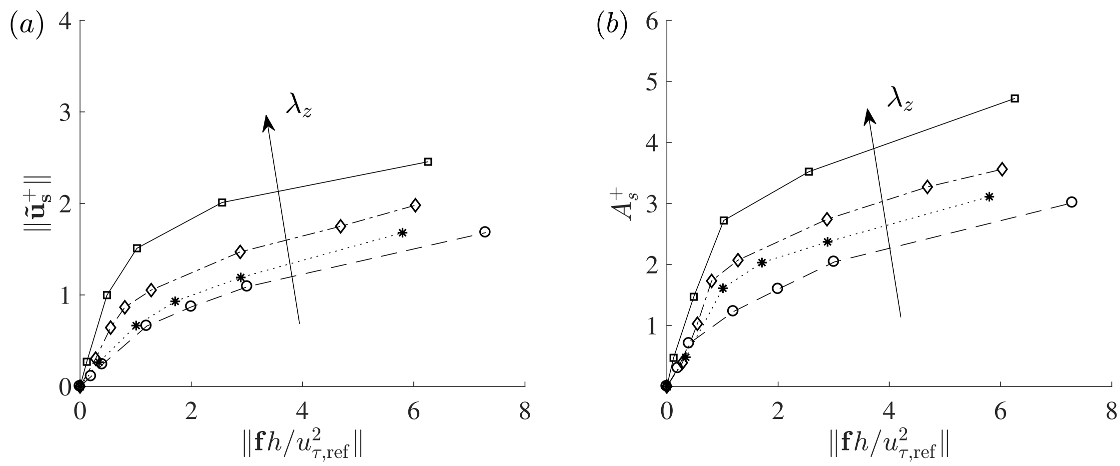

Figure 4.3: Flow response to the forcing for S2050: (a) $||\tilde{\mathbf{u}}_s^+||$; ($b$) A_s^+. Here, the definitions of $||\tilde{\mathbf{u}}_s^+||$ and A_s^+ are given in (4.3) and (4.4), respectively. Symbols: $\circ$, $\lambda_{z,f} = 0.3h$; $*$, $\lambda_{z,f} = 0.5h$; $\diamond$, $\lambda_{z,f} = 0.75h$; $\square$, $\lambda_{z,f} = h$.

λ_z/h	0.30	0.50	0.75	1.00
$\mathbf{R}_{les}$	0.55	0.92	1.67	2.63
$\mathbf{R}_{lin}$	0.26	0.52	0.98	1.69

Table 4.2: Comparison of flow response in the linear regime with respect to the forcing amplitude (S2050).

and the other is half of the maximum difference in the streamwise mean velocity Andersson *et al.* (2001),

$$A_s = \frac{1}{2}\Big(\max_{y,z}\left[\tilde{u}_s(y,z)\right] - \min_{y,z}\left[\tilde{u}_s(y,z)\right]\Big), \tag{4.4}$$

where $\tilde{u}_s$ is the streamwise component of $\tilde{\mathbf{u}}_s$. Fig. 4.4 reports the two streak amplitudes with on increasing the forcing amplitude. It is evident that both $||\tilde{\mathbf{u}}_s^+||$ and A_s^+ are elevated, as the forcing amplitude is increased. In particular, for the small forcing amplitudes (i.e. $||\tilde{\mathbf{f}}h/u_{\tau,\mathrm{ref}}^2|| \ll 1$), both $||\tilde{\mathbf{u}}_s^+||$ and A_s^+ are found to increase linearly with the forcing amplitude, as expected from the derivation of the linear model (2.18).

The linearly growing behaviour of the streak amplitudes further allows us to compare the responses to the forcing in the real flow with those computed with the linear model (2.18). For this purpose, we introduce the response in the linear regime for the simulations:

$$\mathbf{R}_{les} = \frac{||\tilde{\mathbf{u}}_s^+||}{||\mathbf{f}h/u_{\tau,\mathrm{ref}}||}. \tag{4.5a}$$

Similarly, the response of the linear model to the forcing is defined as

$$\mathbf{R}_{lin} = \frac{||\tilde{\mathbf{u}}^{+}||}{||\mathbf{f}h/u_{\tau,\mathrm{ref}}||}. \tag{4.5b}$$

Here, we note that (4.5b) is identical to the one given in (2.21). Table 4.2 compares $\mathbf{R}_{les}$ from the simulations with $\mathbf{R}_{lin}$ from the linear theory. The two values differ from each other, but only a factor of two at most. This suggests that the eddy viscosity is an acceptable approximation for modelling the role of the surrounding turbulence at least in this case. Furthermore, the magnitude of the response is also found to grow with the value of $\lambda_{z,f}$, as is the response of the linear model. However, we were not able to check whether $\mathbf{R}_{les}$ follows the scaling behaviour of $\mathbf{R}_{lin} \sim \lambda_{z,f}$ predicted in Hwang & Cossu (2010*b*) due to the relatively low Reynolds numbers considered.

4.2.2 Statistical evidence of streak instability

Now, we seek the statistical evidence on the streak instability. For the outer-layer streak we have employed the symmetry characteristics of the velocity fluctuations to ascertain this, and here we will follow the same approach, as laid out in §3.2.2 and eq. 3.5. The eigenstructure of a sinuous-mode streak instability is defined by the odd symmetry of the streamwise and wall-normal velocity fluctuations and by even symmetry of the spanwise velocity about $z = z^{*}$, along which the streaky mean flow exhibits local minimum (Andersson *et al.*, 2001; Asai *et al.*, 2002). Since we are here interested in the streak with a size of $\lambda_z = 0.5$, we expect the symmetries to arise around $z = 0.25h$. The cross-streamwise view of velocity fluctuations obtained from the sinuous-mode streak instability is featured by two symmetric peaks in the streamwise and the wall-normal components about $z = z^{*}$ and a single peak along $z = z^{*}$ (Cassinelli *et al.*, 2017). Fig. 4.4 compares the cross-streamwise view of velocity fluctuations of the unforced case (left column) with that of the forced case with $A_s^{+} = 3.11$ (right column), where the spanwise location of the local minimum of the streaky mean flow is given at $z(= z^{*}) = 0.25h$. It is seen that the expected symmetries of the peaks are well visible in the forced simulation, suggesting the existence of sinuous-mode instability around the driven streak at sufficiently large amplitudes.

This observation is further corroborated by turbulent production of the streaky mean flow, as shown in fig. 4.5. The sinuous-mode instability is known to be generated predominantly by spanwise shear of the streaky mean flow, whereas the varicose-mode instability would be

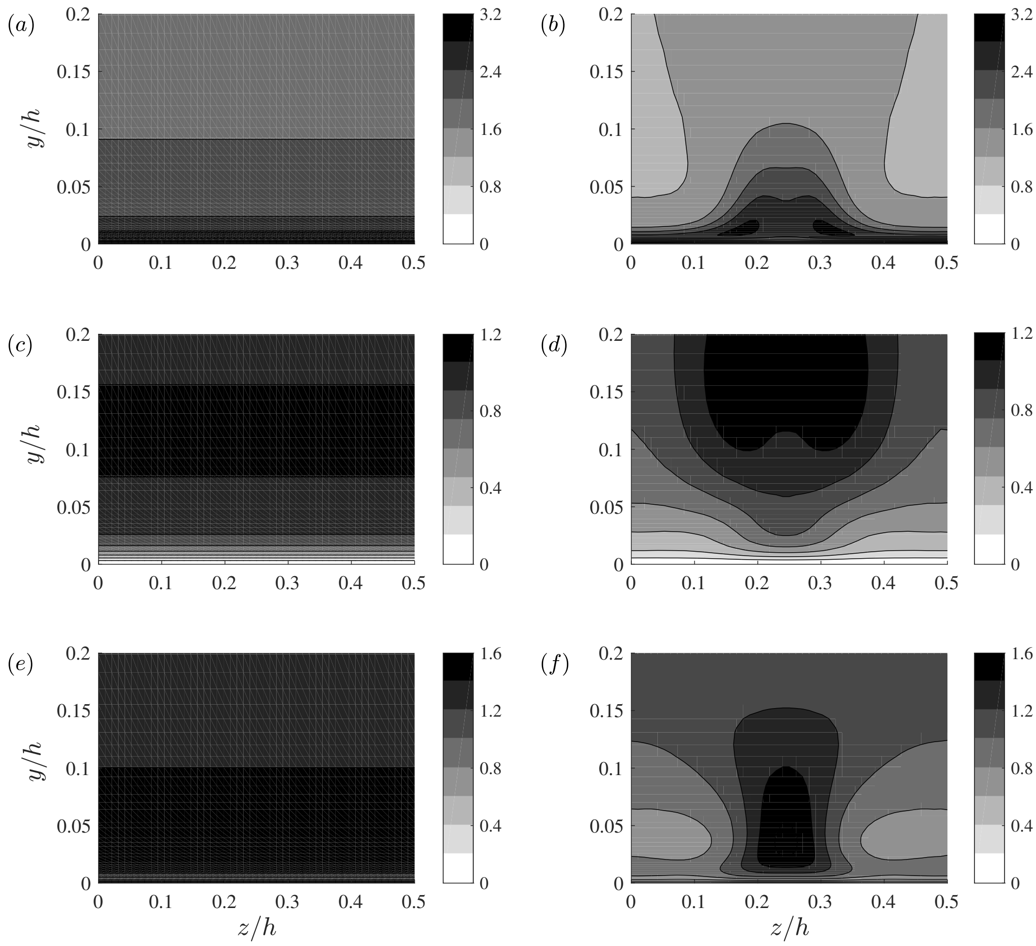

Figure 4.4: Cross-streamwise view of the RMS of the turbulent velocity fluctuations for (a, c, e) $A_s^+ = 0$ and (b, d, f) $A_s^+ = 3.11$ (S2050): (a,b) streamwise velocity; (c,d) wall-normal velocity; (e,f) spanwise velocity.

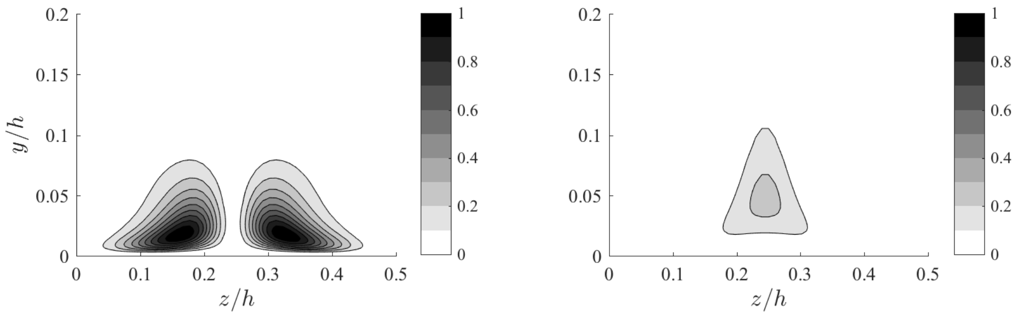

Figure 4.5: Turbulent kinetic-energy production around the streaky mean flow for $\lambda_{z,f} = 0.5h$ and $A_s^+ = 3.11$ (S2050): (a) $-\langle u'w' \rangle_{x,t} \partial U^+(y,z)/\partial z$; (b) $-\langle u'v' \rangle_{x,t} \partial U^+(y,z)/\partial y$. Here, the contours are normalised with the maximum value of (a).

produced by wall-normal mean shear (Park & Huerre, 1995). The former mechanism is characterised by $-\langle u'w' \rangle_{x,t} \partial U/\partial z$ ($U(y,z)$ is the streamwise velocity of streaky mean flow), and the latter by $-\langle u'v' \rangle_{x,t} \partial U/\partial y$. The cross-streamwise visualisation of the two terms in fig. 4.5 highlights that turbulent production by the spanwise mean shear is the main player in generation of the turbulent fluctuations in fig. 4.4, pointing towards the sinuous mode as the main instability mechanism in the forced flow.

The vortex packets in the logarithmic region are statistically in the form of quasi-streamwise vortices (del Álamo *et al.*, 2006). Therefore, if the streak instability is their precursor, the corresponding excitation in the wall-normal and spanwise velocity fluctuations would be anticipated: indeed, in fig. 4.4, the wall-normal and spanwise velocity fluctuations exhibit a significant elevation especially along $z = 0.25h$. To examine the streamwise size of the related turbulent fluctuations, the wall-normal velocity is first sampled around $z = 0.25h$ ($0.2 \leq z/h \leq 0.3$), and its streamwise wavenumber spectra are subsequently plotted in fig. 4.6. Here, in each subfigure, a dashed circle is added, and it indicates the region where an excitation of the wall-normal velocity spectra is expected. This is calculated using the fact that the wall-normal velocity spectra without forcing are aligned well along $y = 0.35\lambda_x$ (the dashed white line in fig. 4.6*a*) and the typical streamwise vortex packet size is twice as long as its spanwise size ($\lambda_x \simeq 2\lambda_{z,f}$ for $\lambda_{z,f} = 0.5h$) (del Álamo *et al.*, 2006; Hwang, 2015), providing the centre location of the circle to be at $(y, \lambda_x) = (0.35h, h)$. When the streak amplitude is relatively small ($A_s^+ = 1.61$), it is a little difficult to see any difference between the spectra of the unforced and forced simulations (fig. 4.6*b*). However, as the streak amplitude is increased ($A_s^+ = 2.03$), the spectral intensity in the circled region appear to gradually increase (fig. 4.6*c*). At the largest streak amplitude

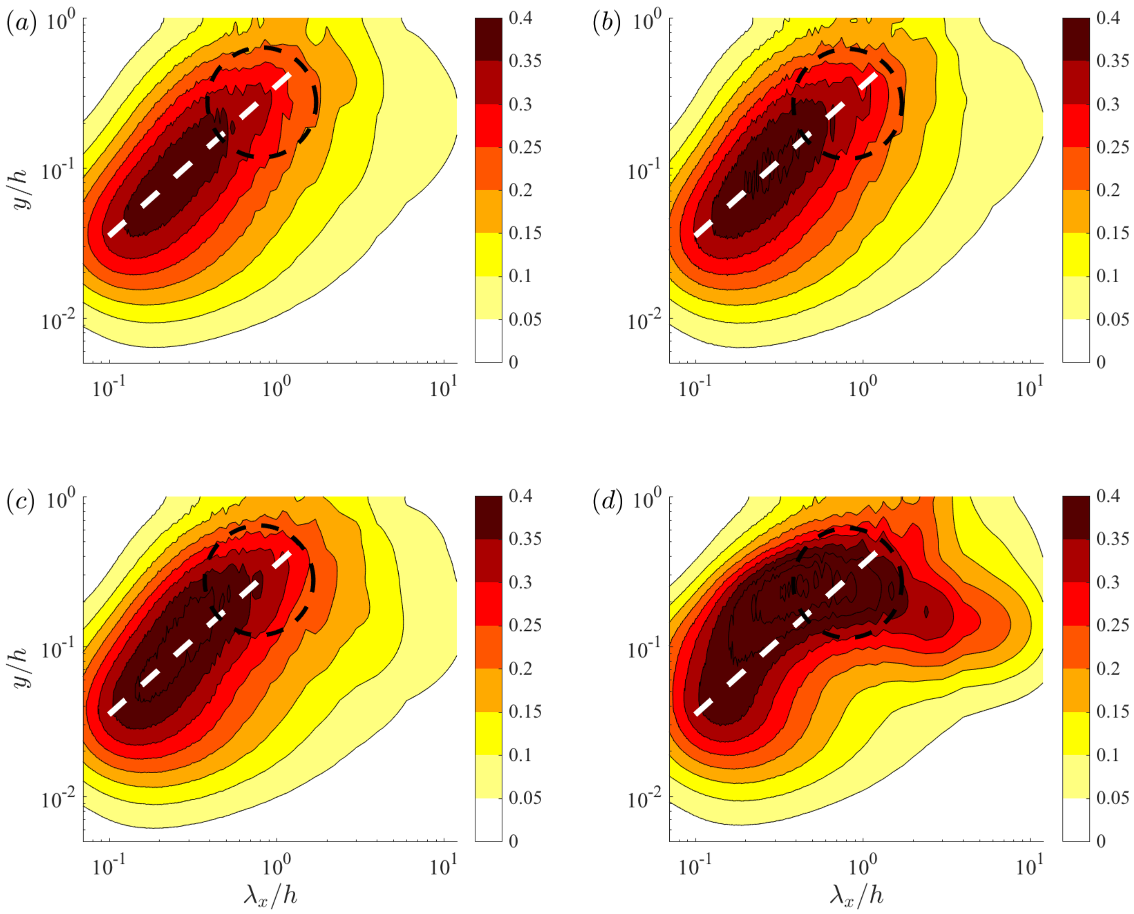

Figure 4.6: Premultiplied streamwise wavenumber spectra of wall-normal velocity, $\lambda_{z,f} = 0.5h$ (S2050). (a) $A_s^+ = 0.48$; (b) $A_s^+ = 1.61$; (c) $A_s^+ = 2.03$; (d) $A_s^+ = 3.11$. Here, the dashed white line indicates $y = 0.35\lambda_x$.

considered ($A_s^+ = 3.11$), the significantly elevated spectral energy around this region spreads over a range of streamwise wavelengths (fig. 4.6*d*).

The streamwise wavenumber spectra of spanwise velocity sampled from the same spanwise locations ($0.2 \leq z/h \leq 0.3$) are also inspected in fig. 4.7, where the centre of the dashed circle of each subfigure is given at $(y, \lambda_x) = (0.15h, h)$. This is also obtained using the fact that the peak streamwise wavenumber of the spanwise velocity spectra without forcing appears be reasonably well aligned along $y = 0.15\lambda_x$ (the dashed white line in fig. 4.7*a*) with the assumption of $\lambda_x \simeq 2\lambda_{z,f}$ for $\lambda_{z,f} = 0.5h$. As in the spectra of the wall-normal velocity, the elevation of the streak amplitude gradually increases the spectral energy in the circled region (figs 4.7*a*-*d*). However, in this case, the energy just below the circled region is also found to be significantly increased together (figs 4.7*b*, *c*). At the highest streak amplitude considered (fig. 4.7*d*), strong energy peaks are developed at $\lambda_x \simeq 3 - 6h$ in the region relatively close to the wall ($y \simeq 0.03 - 0.04h$). It should, however, be mentioned that this behaviour is somehow expected. First of all, even in the absence of any forcing, the near-wall spectra of spanwise velocity already exhibit a significant amount of energy at such large λ_x, as was recently pointed out in Hwang (2016) with an extensive discussion on their origin and scaling (see figs 10 and 11 in Hwang (2016)). Furthermore, it is important to note that the strong energy elevation at $\lambda_x \simeq 3 - 6h$ is also observed in the wall-normal velocity spectra (fig. 4.6*d*), although the energy elevation in this case appears relatively far from the wall ($y \simeq 0.1h$) presumably due to the impermeability boundary condition for the wall-normal velocity. This implies that the energy elevation of the near-wall spanwise velocity at $\lambda_x \simeq 3 - 6h$ for the high streak amplitudes is presumably associated with that of the wall-normal velocity a little further from the wall at the similar streamwise length scales. In this respect, these observations also suggest that the excitation mechanism of the cross-streamwise velocity components described here could be involved in the transfer of the spanwise momentum to the near-wall region.

Finally, it should be emphasised that all the observations made here is not a direct consequence of the forcing, as the lift-up effect itself is mathematically allowed to drive only the streamwise velocity component due to the streamwise-independent nature of the forcing (see the detailed discussion in §2.2). Instead, this implies that the excitation mechanism of the cross-streamwise velocity structures at relatively short streamwise length scales should be from a different physical process, which is only active at large streak amplitudes. Furthermore, these cross-streamwise velocity structures are first excited at $0.7 < \lambda_x/h < 1.5$ on increasing the streak amplitude (figs 4.6*b*, 4.7*b*). With a further increase of the streak amplitude, the range

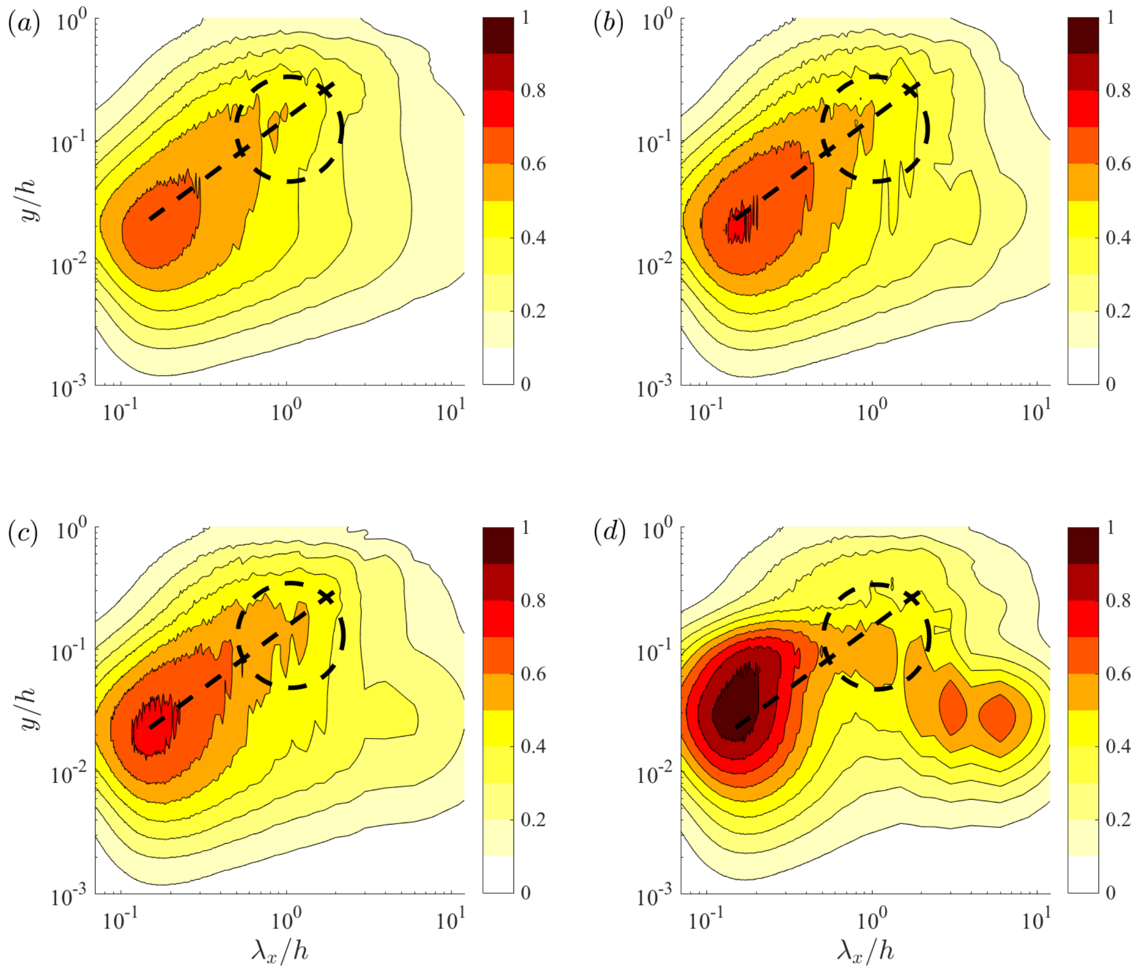

Figure 4.7: Premultiplied streamwise wavenumber spectra of spanwise velocity, $\lambda_{z,f} = 0.5h$ (S2050). (*a*) $A_s^+ = 0$; (*b*) $A_s^+ = 1.61$; (*c*) $A_s^+ = 2.03$; (*d*) $A_s^+ = 3.11$. Here, the dashed line indicates $y = 0.15\lambda_x$.

of the excited streamwise length scales becomes wider (figs 4.6*d*, 4.7*d*). This feature is exactly anticipated from the previous theoretical analysis on the streak instability (Alizard, 2015; Park *et al.*, 2011), where the range of the unstable streamwise wavelength was shown to become wider on increasing the streak amplitude.

4.2.3 Dynamic mode decomposition

Now, we employ the DMD described earlier to inspect the detailed flow structure associated with the observations above. The required snapshots are built from the Fourier coefficients of the velocity fields, sampled in the lower half of the channel. The spanwise wavenumber is selected to be the same as that of the forcing profile ($k_z = 2\pi/\lambda_z$ with $\lambda_z = \lambda_{z,f}$), while a range of streamwise wavenumbers ($k_x = 2\pi/\lambda_x$) is chosen in accordance with the observation with fig. 4.6 ($\lambda_z \lesssim \lambda_x \lesssim 3\lambda_z$). For given k_z and k_x, each snapshot is chosen to have the following form:

$$\tilde{\mathbf{u}}_s(y, z; k_x) = \hat{\mathbf{u}}(y; k_x, k_z)e^{ik_z z} + \hat{\mathbf{u}}(y; k_x, -k_z)e^{-ik_z z}, \tag{4.6}$$

where $\hat{\mathbf{u}}(y; k_x, k_z)$ is a plane Fourier mode. We note that $\tilde{\mathbf{u}}_s(y, z; k_x)$ now becomes the streamwise Fourier component given only with $\pm k_z$ spanwise Fourier components. The time interval, the number of POD modes, and the number of the snapshots for the DMD are then carefully chosen to ensure good temporal resolution for the dynamics of interest: the maximum time-step employed is $\Delta t u_\tau/h = 0.007$, the number of modes $r = 100$ and the total number of snapshots $N > 1000$ (see Appendix A for a more detailed discussion on the choice of the parameters). Once the DMD is performed, the phase speed c_j for a given DMD mode is computed from $c_j = \omega_j/k_x$, where ω_j is the real part of (i $\ln\mu_j/\Delta t$).

The outcome of DMD analysis for $\lambda_{z,f} = 0.5h$ is reported in fig. 4.8. Fig. 4.8(a) shows that the eigenvalues of matrix $\mathbf{S}$ are reasonably superimposed onto the unit circle, confirming that most of the DMD modes are neutral and collected from a statistically stationary system. The amplitude of each mode is plotted in fig. 4.8(b). The modes tend to cluster around the phase speed comprised between $0.7 < c/U_c < 0.9$ (U_c is the mean streamwise velocity at the centreline), in which the most energetic ones are located. The phase speed c is found to be virtually unchanged for different values of the streak amplitude at the given Re_τ.

The most energetic DMD mode is visualised in fig. 4.9 with the driven (averaged) streak. The streak is uniform in the streamwise direction, as it should be the outcome of the streamwise uniform forcing (fig. 4.9a), whereas each velocity component of the DMD mode $\mathbf{u}_{dmd}$ is composed

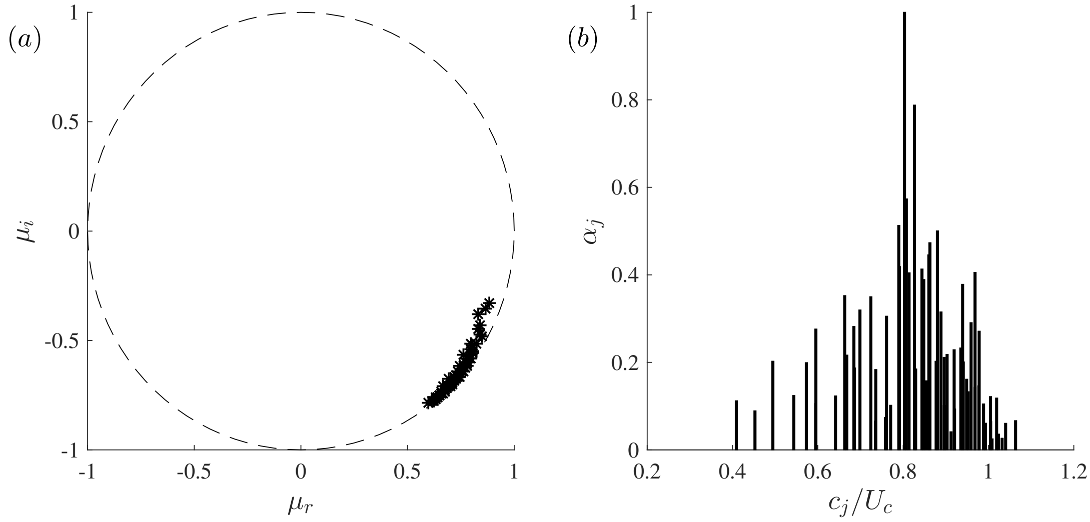

Figure 4.8: DMD results for $\lambda_{z,f} = 0.5h$, A_s^+=3.11, $\lambda_x = h$ (S2050): (a) distribution of the eigenvalues on the unit circle; (b) mode amplitude α_j against phase velocity c/U_c. In (b), the mode amplitude α_j is normalised by the most energetic DMD mode.

of alternating regions of positive and negative values, distributed symmetrically with respect to the spanwise centre of the mean streak (fig. 4.9b). When the driven streak and the DMD mode are assembled together, the resulting structure is well represented by a low-speed streak undergoing a sinusoidal motion flanked with alternating cross-streamwise velocity structures (fig. 4.9c). This visualisation of the DMD mode suggests that the structure excited by a highly amplified streak shows striking similarity to a sinuous-mode instability, as in the case of the large-scale outer structure. Finally, the main features of the flow field assembled with the streak and the DMD mode (fig. 4.9c) are also highly reminiscent of those of recently computed travelling-wave solution (e.g. Hwang *et al.*, 2016), supporting the relevance of the self-sustaining process in the structures of the logarithmic region.

4.2.4 Self-similarity

Thus far, we have mainly focused on the streak instability for $\lambda_{z,f} = 0.5h$. We now consider different values of $\lambda_{z,f}$ to examine the self-similarity of the streak instability. Fig. 4.10 reports the streamwise wavenumber spectra of wall-normal velocity for four different $\lambda_{z,f}$. Here, the wall-normal velocity for computation of the spectra is sampled around the low-speed region of the mean velocity (i.e. $0.35\lambda_{z,f} \leq z/h \leq 0.65\lambda_{z,f}$) and the streak amplitude for each $\lambda_{z,f}$ is

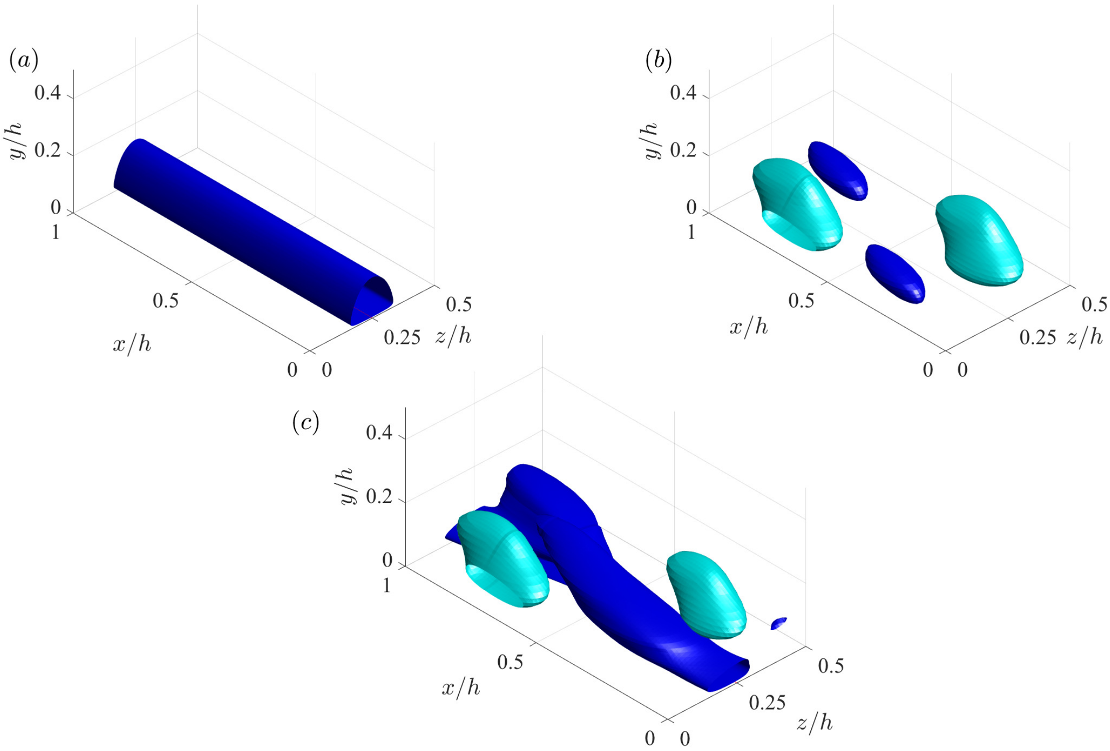

Figure 4.9: Visualisation of the streak instability using the most energetic DMD mode (S2050) for $\lambda_{z,f} = 0.5h$, $A_s^+ = 3.11$ $\lambda_x \simeq h$: (a) the low-speed streak with $u_s' = -0.85u_\tau$ ($u_s' \equiv u_s(y,z) - \langle u_s(y,z)\rangle_z$ where $\langle\cdot\rangle_z$ denotes average in the spanwise direction); (b) the DMD mode $\mathbf{u}_{dmd}$, where the dark blue iso-surfaces represent a negative streamwise velocity ($u = 0.8\min[u_{dmd}]$), and the pale blue ones a negative wall-normal velocity ($v = 0.8\min[v_{dmd}]$); (c) the low-speed streak with the DMD mode ($\mathbf{u}_s - \langle\mathbf{u}_s\rangle_z + \gamma\mathbf{u}_{dmd}$ where γ is an appropriate tuning constant for visualisation). In (c), the dark iso-surface indicates a negative streamwise velocity, while the pale ones indicate a negative wall-normal velocity.

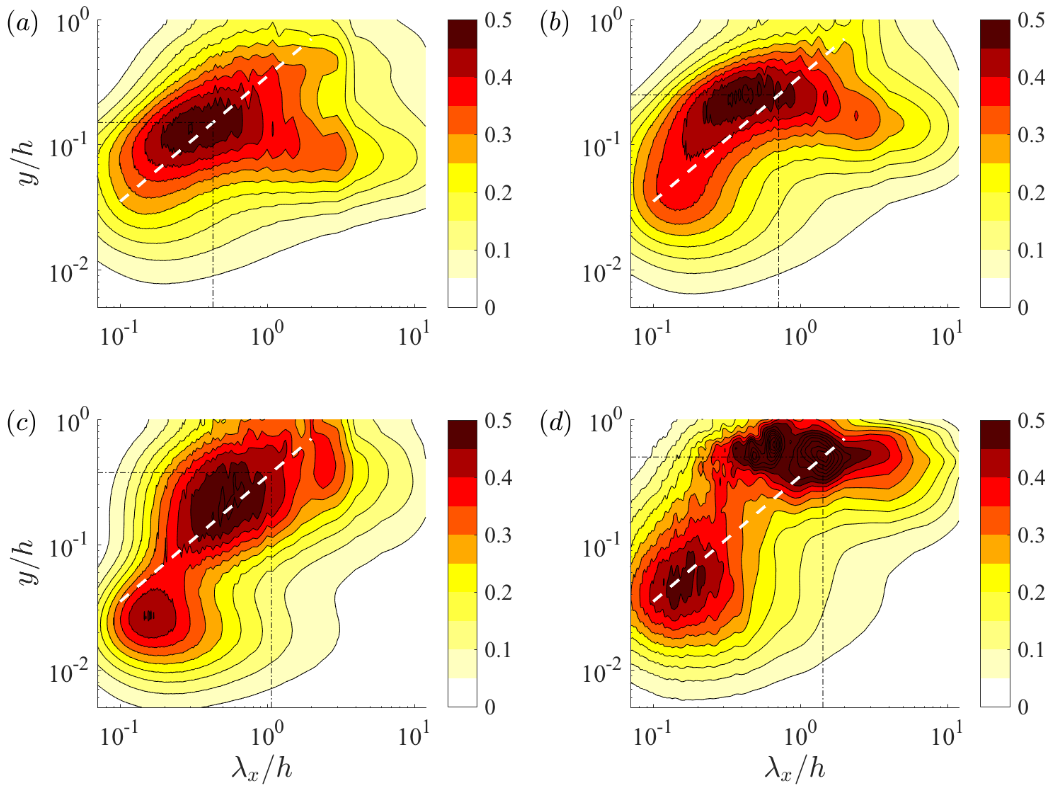

Figure 4.10: Premultiplied streamwise wavenumber energy spectra of wall-normal velocity (S2050): (*a*) $\lambda_{z,f} = 0.3h$ ($A_s^+ = 3.01$); (*b*) $\lambda_{z,f} = 0.5h$ ($A_s^+ = 3.11$); (*c*) $\lambda_{z,f} = 0.75h$ ($A_s^+ = 3.27$); (*d*) $\lambda_{z,f} = 1h$ ($A_s^+ = 3.53$). Here, the wall-normal velocity is sampled from $0.35\lambda_{z,f} \leq z/h \leq 0.65\lambda_{z,f}$. The dashed white line indicates $y = 0.35\lambda_x$.

chosen to be sufficiently large ($A_s^+ \simeq 3$), so that the wall-normal velocity structure from the streak instability is well captured. The computed wall-normal velocity spectra reveal that their most energetic parts are well aligned along the linear ridge $y = 0.35\lambda_x$, which was given for the scaling of the original wall-normal velocity spectra without forcing (fig. 4.6*a*). This suggests that the streak instability process can excite the wall-normal velocity structures in a self-similar way, by which the entire energy-containing region of the wall-normal spectra can be recovered.

The effect of the streak amplitude is also assessed in fig. 4.11 where the streamwise wavenumber spectra of wall-normal velocity at $(y, \lambda_x) = (0.6\lambda_{z,f}, 1.8\lambda_{z,f})$ are plotted on increasing the streak amplitude. As expected from fig. 4.6, the energy of the spectra at this location is elevated with the streak amplitude. We note that the streak amplitude for the onset of the instability was previously predicted to be $A_{s,c}/U_c \simeq 0.18$ at $Re_\tau = 5000$ by Alizard (2015), where a Floquet analysis was conducted by incorporating the ignored non-linearity into (2.18). Since $U_c/u_\tau \simeq \kappa^{-1} \log Re_\tau + B$ with $\kappa \simeq 0.4$ (the Kármán constant) and $B = 5.2$, this prediction gives $A_{s,c}^+ \simeq 4.8$ for the onset of the streak instability. This theoretically predicted value appears to be considerably larger than $A_s^+ \gtrsim 2-3$, above which a range of the streamwise length scale appear to be already excited, indicating that the eddy viscosity model in Alizard (2015); Park *et al.* (2011) may be too much diffusive for the analysis of the streak instability. However, it should also be pointed out that the streak instability has been understood to be subcritical (Schoppa & Hussain, 2002), allowing for a significant non-normal amplification before the onset of linear instability. In this respect, the effect of background noise such as surrounding turbulence should not be ignored, although it is practically impossible to quantify it.

Finally, we present the dependence of the phase speeds computed from DMD. To account for all the significant DMD modes, the overall phase speed is obtained by averaging the phase speed of all the DMD modes with sufficiently large amplitudes: i.e.

$$c = \frac{\sum_{j=1}^{N_l} [\alpha_j k_x \omega_j]}{\sum_{j=1}^{N_l} \alpha_j}, \tag{4.7}$$

where $k_x = 2\pi/\lambda_x$ and N_l is the number of the DMD modes with the magnitude larger than 5% of the magnitude of the leading DMD mode. Here, it should be mentioned that the simulations with forcing have the mean velocity profiles different from that of the unforced reference simulation due to the high-amplitude streaks introduced by the forcing (see Gayme *et al.* (2010) for this

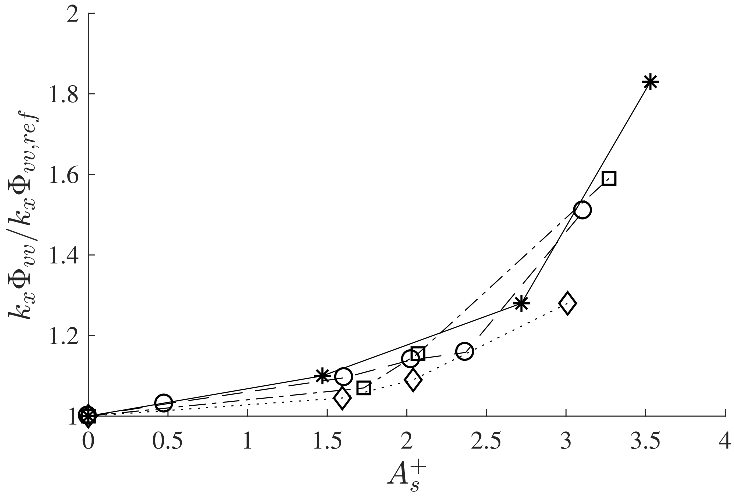

Figure 4.11: Maximum value of the streamwise wavenumber spectra of wall-normal velocity at $y = 0.6\lambda_{z,f}$ (S2050): $\diamond$, $\lambda_{z,f} = 0.3h$; $\circ$, $\lambda_{z,f} = 0.5h$; $\square$, $\lambda_{z,f} = 0.75h$, $*$ $\lambda_{z,f} = h$.

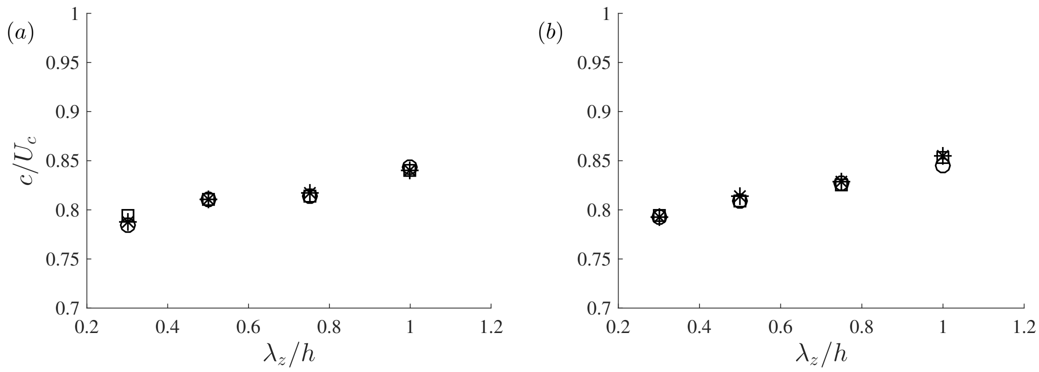

Figure 4.12: Dependence of the averaged phase speed c of the DMD modes on the spanwise wavelength of the forcing, $\lambda_{z,f}$: (a) S950; (b) S2050. The symbols are: $*$, $\lambda_x = 2\lambda_{z,f}$; $\square$, $\lambda_x = 1.6\lambda_{z,f}$; $\circ$, $\lambda_x = 1.3\lambda_{z,f}$. Here, the streak amplitude of the DMD mode is chosen to be $2 < A_s^+ < 3.5$.

issue). Since the advection of the flow structure of interest would be mainly determined by the mean velocity (i.e. Taylor's hypothesis), it would be difficult to establish any quantitative relation between the phase speed from the present DMD modes and the one of the structures in the 'unforced' simulation. Therefore, the phase speed from the DMD modes is normalised using the centreline velocity U_c of each simulation to present their relative velocity to inspect their general trend with $\lambda_{z,f}$. Fig. 4.12 reports the phase speeds of the DMD modes with respect to $\lambda_{z,f}$ for $Re_\tau \approx 1000$ (S960) and $Re_\tau \approx 2000$ (S2050). The phase speed appears to increase with $\lambda_{z,f}$, and the values of the phase speed range from $c/U_c \approx 0.79$ for $\lambda_z/h = 0.3$, to $c/U_c \approx 0.86$ for $\lambda_z/h = 1$. These numbers are smaller than the phase speed of the instability of the streak with $\lambda_{z,f} \simeq 1.5h$ ($c \simeq 0.9$) that mimics the very-large-scale motion (see chapter 3), and they are not very far from those predicted by the Floquet theory (Alizard, 2015).

4.3 Discussion

The present numerical experiment has shown that the streak instability process in the logarithmic region emerges in a self-similar manner. Given the fact that the streak instability is a subprocess of the self-sustaining process, this observation is consistent with the existence of the self-similar self-sustaining process throughout the entire logarithmic region (Hwang, 2015; Hwang & Bengana, 2016; Hwang & Cossu, 2011). In particular, it is shown that the streak instability mechanism can initiate the vortical structures mainly composed of cross-streamwise velocity components, and their size is characterised in a self-similar manner, as follows:

$$\lambda_x \simeq 2 - 3\lambda_z, \qquad y \simeq 0.3 - 0.7\lambda_z. \tag{4.8}$$

It should be stressed that the size of the vortical structure is strikingly similar to that of the vortex packets often called the hairpin vortex packets (Tomkins & Adrian, 2003) or the tall-attached vortex clusters (del Álamo *et al.*, 2006). This size is also comparable in the vortical structures of the self-sustaining attached eddies in Hwang (2015). Furthermore, the vortex packets generated by the streak instability mechanism can reach the near-wall region through the spanwise velocity (fig. 4.7), and this is also consistent with the wall-reaching nature of the vortex clusters reported in del Álamo *et al.* (2006). Taking all the observations, the present numerical experiment suggests that the self-similar vortex packets (or clusters) in the logarithmic region are likely to be formed or at least to be initiated by the streak instability mechanism in the self-similar self-sustaining process (Hwang, 2015; Hwang & Bengana, 2016).

5

Contributions to skin friction from attached eddies

5.1 Introduction

The reduction of skin friction in wall-bounded turbulent shear flows is an important goal to decrease energy expenditure in many industrial sectors. It has a wide range of engineering applications ranging from massive pipelines for oil and gas transport to almost all types of vehicles, ground, air or sea-based. Many of these applications typically take place at high Reynolds numbers, and a wealth of systems and techniques to reduce turbulent skin friction drag has been proposed over many years. In practice, only very few of these systems and techniques have been implemented to a successful extent, and many of them appear to be subject to a performance loss as the Reynolds number increases, as well as other technical constraints (Bushnell, 2002; García-mayoral & Jiménez, 2011; Kornilov, 2015; Quadrio, 2011).

5.2 Results

5.2.1 Skin-friction generation at $Re_\tau \simeq 2000$

The skin-friction generation by the motions at $\lambda_z \leq \lambda_{z,t}$ is assessed by the three methods presented in chapter 2, at $Re_\tau \simeq 2000$; the outcome is reported in fig. 5.1. We note that the spanwise length of the largest energy-containing structures (VLSMs and LSMs) is $\lambda_z = 1.5h$, and that of the smallest ones (near-wall streaks and quasi-streamwise vortices) is $\lambda_z \simeq 0.05h$ (from $\lambda_z/h = \lambda_z^+/Re_\tau$ with $\lambda_z^+ = 100$) at this Reynolds number. The most immediate and

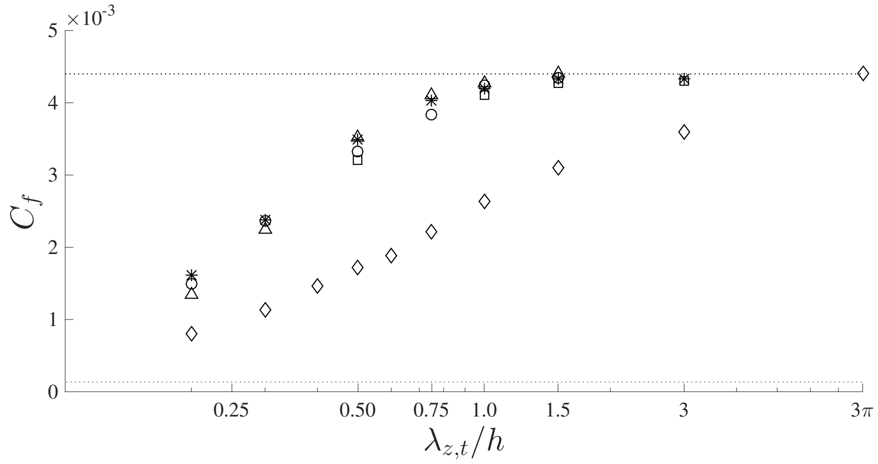

Figure 5.1: Variation of C_f with the cut-off spanwise wavelength $\lambda_{z,t}$ at $Re_\tau \simeq 2000$: $\diamond$, FIK-identity-based approach; $*$, box-confinement approach (with spanwise uniform mode); $\triangle$, box-confinement approach (without spanwise uniform mode) $\circ$, artificial damping with $W2000$; $\square$, artificial damping with $F2000$. Here, the upper and lower horizontal lines indicate turbulent (from DNS by Hoyas & Jiménez, 2006) and laminar skin-friction coefficient ($C_f = 12/Re_m$), respectively.

evident conclusion in fig. 5.1 is that, no matter which approach we take, the spanwise scales in the range of $0.2h \leq \lambda_z \leq 1h$ are responsible to the largest portion of skin friction and their removal leads to significant reduction of wall shear stress. The FIK-identity-based approach shows that this range of the spanwise scales is responsible to 41% of total skin friction, while the box-confinement approach and the artificial damping reveal that around 60% of skin-friction reduction is achieved by removing the motions at $\lambda_z > 0.2h$. This striking result implies that the largest amount of the skin friction at sufficiently high Reynolds numbers is generated by the self-similar energy-containing motions, most of which belong to the logarithmic region in the sense that their spanwise length scale is proportional to the distance from the wall.

An important difference is, however, observed between the skin frictions obtained with the FIK-identity-based approach and with the other two approaches. The FIK-identity-based method shows that the largest motions at $\lambda_z \geq 1.5h$ are involved in a considerable amount of skin friction, i.e. $25 \sim 30\%$ of total skin friction. This amount is not very far from that obtained by Deck *et al.* (2014), who computed the skin-friction generation by large scale structures using the streamwise spectra for $\lambda_x > 1 \sim 2\delta$ in a turbulent boundary layer (δ is the boundary-layer thickness). This approach also shows that skin-friction generation by the spanwise length scales of $\lambda_z > 1.5h$ is not negligible, despite the fact that the spanwise length of both the VLSMs and the LSMs is $\lambda_z \simeq 1.5h$. This is because the spanwise wavenumber spectra from the DNS with

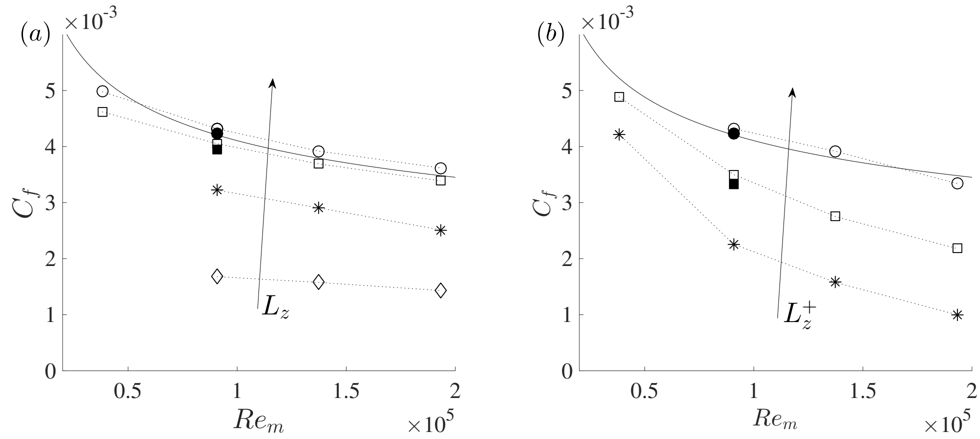

Figure 5.2: Variation of C_f with Re_m for the box-confinement approach (i.e. $L_z = \lambda_{z,t}$): (a) constant $L_z(= 0.2, 0.4, 0.75, 1.5h)$; ($b$) constant $L_z^+(\simeq 400, 1000, 3000)$. The filled square symbols (■) represent the artificial damping approach. Here, ——— , C_f suggested by Dean (1978) ($C_f = 0.073Re_m^{-0.25}$).

a large spanwise computational domain ($L_z = 3\pi$) contain a non-negligible amount of energy for $\lambda_z > 1.5h$ (see also fig. 5.1). However, the box-confinement approach and the artificial damping, both of which show very similar behaviour to each other, yield very different trend of C_f with $\lambda_{z,t}$ from the FIK-based approach. We observe that a sensible reduction in skin-friction ($4 \sim 8\%$) is observed only when $\lambda_{z,t} \simeq 0.75 \sim 1.0h$, by which the largest structures at $\lambda_z \simeq 1.5h$ are removed. It is interesting to note that a cutoff $\lambda_{z,t} > 1.5h$ yields basically no reduction in drag in the box-confinement and artificial damping approach, whereas the FIK appeared to show a non-negligible role of those structures in skin-friction generation. It is difficult to explain this feature if we exclude the role of scale interaction in the skin-friction generation process. A detailed discussion on this issue will be given in §5.3.1.

Finally, it is worth mentioning that the uniform spanwise mode in the box-confinement approach is found to have little influence on the skin friction, as also shown in fig. 5.1. Indeed, the removal of the spanwise uniform mode with (2.34) slightly reduces the skin friction only for relatively small $\lambda_{z,t}(= 0.2 \sim 0.3h)$ by the removal of the spanwise uniform mode ($\triangle$ in fig. 5.1). This implies that the direct interaction between the spanwise uniform mode and the motions at $\lambda_z \leq \lambda_{z,t}(= L_z)$ is probably very minor. Further detailed evaluation of the differences between simulations with and without the uniform spanwise mode is presented in Appendix B.2.

5.2.2 Different Reynolds numbers

Since the box-confinement approach and the artificial damping do not yield very different skin friction (see also discussion in §5.3.1), the assessment of the skin friction generation by the motions at $\lambda_z \leq \lambda_{z,t}$ is further explored only with the box-confinement approach up to $Re_\tau \simeq 4000$. Fig. 5.2 shows the skin-friction generation with respect to $\lambda_{z,t}(= L_z)$ at four different Re_m. When L_z is chosen to scale with the outer unit, the reduced skin friction is found to follow a similar curvature with that of the full skin friction obtained with $L_z = 1.5h$ without any further deviation on increasing Re_m (fig. 5.2*a*). In contrast, when L_z is set to scale with the inner unit, the deviation between C_f for $L_z^+ < 3000$ and that for $L_z^+ = 3000$ gradually increases with the Reynolds number. This implies that the contribution of the motions, the spanwise size of which is smaller than the given inner-scaled one, to total skin friction continuously decreases on increasing Re_m. This is consistent with the low-Reynolds-number result in Hwang (2013), who observed that the structures smaller than a fixed value of $L_z^+(\simeq 100,\ 200)$ yield decreasing portions of skin friction on increasing Re_m. The behaviour in fig. 5.2 clearly suggests that, at very high Reynolds numbers, most of skin friction would be generated by the motions, the spanwise size of which lies between $\lambda_z^+ \approx 100$ and $\lambda_z \simeq 1.5h$. Given the size of these motions proportional to the distance from the wall (i.e. $\lambda_z \sim y$), this indicates that the dominant skin-friction generation takes place essentially in the logarithmic region. It is possible to try and assess the effect of the large scales on the drag generation, by recalling the theory introduced by Luchini (1996), as well as the modulation theory by Mathis *et al.* (2009). The removal of the larger structures, especially in the logarithmic region, could be considered as the removal of an induced, time-dependent forcing on the near-wall structures; therefore, by eliminating this overarching interaction, the near-wall structures would produce less skin friction as a consequence of reduced oscillations. It is anyway difficult to pinpoint the exact mechanism of drag reduction, and debate still exists whether the large scales would contain enough energy to produce such an effect.

As the Reynolds number is increased, ‘more’ structures exist at a λ_z^+ larger than the given threshold, which could help to explain the behaviour in 5.2; while this can be considered as a slightly alternative explanation to our observations, it should still be noted that this line of reasoning does not negate, and indeed supports, the idea of the logarithmic region as very significant to drag generation.

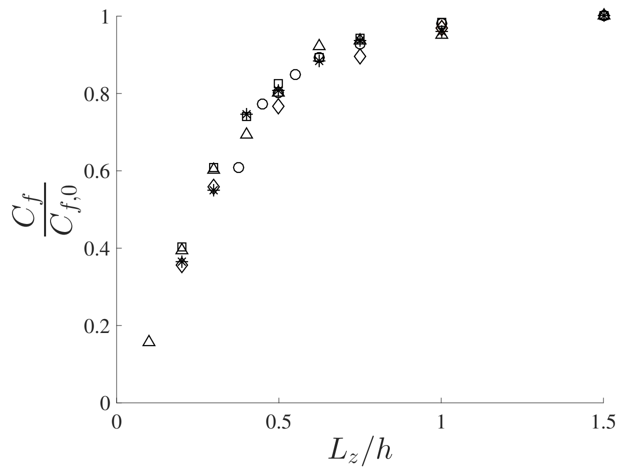

Figure 5.3: Variation of normalised skin friction coefficient with $L_z(=\lambda_{z,t})$: $\circ$, $Re_m = 38100$; $*$, $Re_m = 89100$; $\diamond$, $Re_m = 89100$, artificial damping; $\square$, $Re_m = 137500$; $\triangle$, $Re_m = 193200$.

Finally, the reduced amount of skin friction by setting $L_z < 1.5h$ is found to approximately scale with the outer unit if the Reynolds number is sufficiently high. In fig. 5.3, the skin friction coefficient normalised by the reference one with $L_z = 1.5h$ are plotted with respect to L_z/h for all the Reynolds numbers considered. All the data, obtained at four different Re_m, appear to collapse approximately well into a single curve. For instance, a reduction in skin friction in the region of $7 \sim 8\%$ is obtained halving the spanwise width (i.e. $L_z = 0.75h$). Another 10% of the original friction is lost by reducing the box width to $L_z = 0.5h$. At $L_z = 0.2h$, the amount of skin friction generated is very close to 40% of the initial value, for all three of the larger Reynolds number.

5.2.3 Probability density function of turbulent skin friction

To further investigate how the statistical behaviour of turbulent skin-friction generation is changed by the removal of the structures at $\lambda_z > \lambda_{z,t}$, probability density functions (PDFs) of skin friction are computed with the box-confinement approach ($\lambda_{z,t} = L_z$) at $Re_\tau \simeq 2000$. It has been found that the PDFs of instantaneous skin friction are positively skewed in a wide range of the Reynolds numbers (Keirsbulck *et al.*, 2012; de Silva *et al.*, 2014). This feature has often been interpreted to appear because the large-scale positive excursion of wall shear stress accompanies energetic small-scale wall-shear-stress fluctuations (Baars *et al.*, 2015; Chernyshenko *et al.*, 2012; Mathis *et al.*, 2013). The positive skewness of the PDFs also implies that if a high

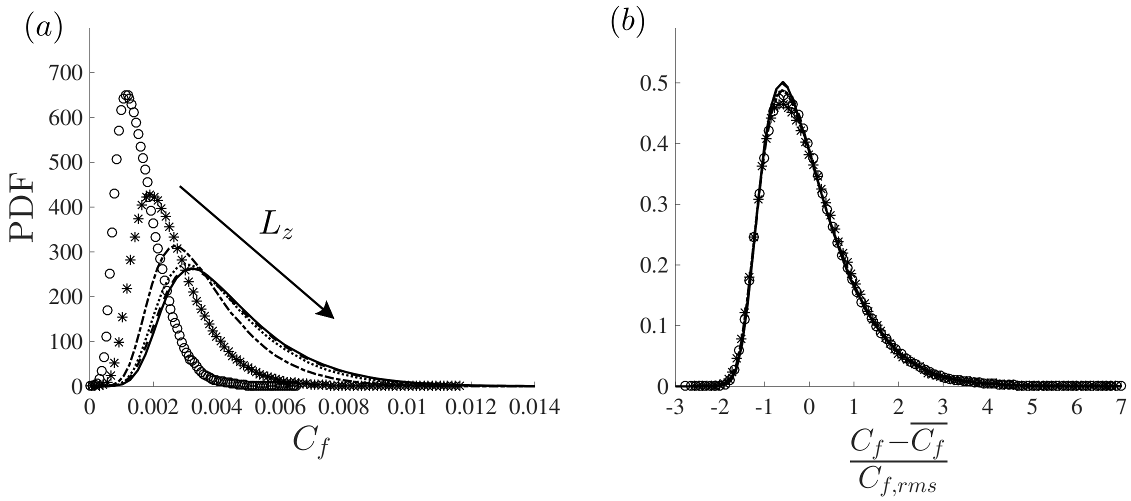

Figure 5.4: Probability density functions of instantaneous skin friction C_f from the box-confinement approach (i.e. $\lambda_{z,t} = L_z$) with (a) the original variable C_f and (b) normalised variable, $(C_f - \overline{C}_f)/C_{f,rms}$ where $C_{f,rms}$ is the root mean square of C_f: ——— , $L_z = 1.5h$; - - - - , $L_z = 1h$; ·········, $L_z = 0.75h$; $-\cdot-\cdot-$, $L_z = 0.5h$; $*$ $L_z = 0.3h$; $\circ$ $L_z = 0.2h$.

pass filter is applied to the instantaneous wall-shear-stress signal, its mean would be reduced, consistent with the observations in §5.2.1 and §5.2.2.

Fig. 5.4(a) shows the PDFs of the skin-friction coefficient C_f for several L_z. As L_z decreases, the peak location of the PDF moves towards smaller C_f, indicating reduction of mean skin friction. Also, the width of the PDFs is found to be decreased on decreasing L_z, suggesting that the variance of wall shear stress is also reduced by the decrease of L_z. Interestingly, the normalised PDFs, shown in fig. 5.4(b), do not appear to be so different from one another, indicating that the skin-friction generation process in each confined computational domain is statistically self-similar. We note that, given the findings in §5.2.1 and §5.2.2, the skin-friction generation process for all of the sufficiently large L_z would involve some extent of the hierarchical organisation of self-similar energy-containing motions, the largest one of which is determined by the spanwise computational domain L_z. This implies that the only difference among the processes in different computational domains would stem from the largest energy-containing motions and the resulting extent of the hierarchical organisation. Except these, the processes in different computational domains are supposed to be similar to one another. This is clearly indicated by fig. 5.4(b), also consistent with the notion that all the self-similar energy containing motions throughout the entire wall-normal directions involve turbulent skin-friction generation.

5.3 Discussion

All the three independent approaches introduced in the present study consistently show that all the energy-containing motions ranging from the inner to the outer units are actively involved in turbulent skin-friction generation. In particular, the self-similar energy-containing motions at the spanwise length scale λ_z between $\lambda_z^+ \simeq 100$ and $\lambda_z \simeq 1.5h$ have been shown to be mainly responsible for turbulent skin-friction generation at sufficiently high Reynolds numbers. It is evident that the near-wall region gradually loses its dominant role in the friction generation on increasing the Reynolds number (fig. 5.2*a*), consistent with previous findings (Chang *et al.*, 2002; Gatti & Quadrio, 2013; Hwang, 2013). A little surprisingly, the contribution from the largest scales in the flow also appears to be limited. This is particularly true, as their removal does not result in reduction of the skin friction for which they are responsible (fig. 5.1; see also a further discussion in §5.3.3).

This finding is also consistent with the well-documented logarithmic growth of the near-wall streamwise turbulence intensity with the Reynolds number (Marusic & Kunkel, 2003), i.e. the feature reflecting the increasing influence of the energy-containing motions in the logarithmic and outer regions to the near-wall region. The wall-attached part of each of the attached eddies is mainly composed of the streamwise and spanwise velocity components due to impermeability condition at the wall (Hwang, 2015; Perry & Chong, 1982; Townsend, 1976). This therefore implies that the collective skin-friction generation by the self-similar energy-containing motions is probably a consequence of their near-wall influence, establishing a tight physical link with the logarithmic growth of the near-wall streamwise turbulence intensity with the Reynolds number. In this respect, it is also worth mentioning that this finding is consistent with very recent observation by Renard & Deck (2016), who identified the dominant contribution of the logarithmic region to skin-friction generation using a theoretical formula based on the mean streamwise kinetic-energy budget. Lastly, it is worth pointing out that DNS data for channel flow at $Re_\tau \approx 5200$ (Lee & Moser, 2015) have shown an increase in the energy carried by the outer structures (the VLSM in particular) with a consequent impact on the velocity spectra as well. While this may potentially signify a more pronounced contribution of the largest scales to turbulent skin friction, it is difficult to disregard the observation made with fig. 5.2(*b*) even at higher Reynolds numbers.

Finally, it should be pointed out that the wall-attached part of each of the attached eddies is 'inactive' in the sense that they carry very little Reynolds shear stress, since there is little wall-normal velocity in the vicinity to the wall (Hwang, 2015; Townsend, 1976). However, this does not necessarily imply that the inactive wall-attached part is not related to turbulent skin-friction generation, as the skin friction is nothing more than the streamwise velocity in the very vicinity to the wall, given its mathematical definition (i.e. $\nu\partial u/\partial y$ at the wall). This rather indicates that the energy-containing motions, which essentially reside in the logarithmic and outer regions, transport the streamwise momentum to the near-wall region through their inactive part, while generating Reynolds shear stress with their wall-detached wall-normal velocity component in the region much further from the wall. This transport process of the streamwise momentum by the wall-normal velocity described here is likely to be the so-called 'lift-up' effect (Cossu *et al.*, 2009; Hwang & Cossu, 2010*b*), a part of the self-sustaining process extensively discussed in Hwang & Bengana (2016). The following discussion addresses this issue.

5.3.1 Skin-friction generation and the self-sustaining process

The concept of the self-sustaining process was originally proposed by Hamilton *et al.* (1995) for the near-wall motions, which were recently shown to be the smallest attached eddies (Hwang, 2015; Hwang & Bengana, 2016). The self-sustaining process is a cyclic dynamical process composed of three substeps: 1) the streaks are amplified by streamwise vortices via the lift-up effect, the process by which the streamwise vortices transfers the energy of the mean shear to the streaks (Chernyshenko & Baig, 2005*b*; Cossu *et al.*, 2009; Hwang & Cossu, 2010*b*; Kim & Lim, 2000; Landahl, 1990; Pujals *et al.*, 2009); 2) the amplified streaks break down with a sinuous-mode secondary instability and/or transient growth (Hamilton *et al.*, 1995; Park *et al.*, 2011; Schoppa & Hussain, 2002); 3) the streamwise vortices are regenerated by non-linear mechanisms (Hamilton *et al.*, 1995; Hwang & Bengana, 2016; Schoppa & Hussain, 2002). It has recently been shown that the energy-containing motions in the logarithmic and outer regions bear the same self-sustaining process with a single turn-over time period given by $Tu_\tau/\lambda_z \simeq 2$ (Hwang & Bengana, 2016).

In the box-confinement approach, the size of the largest energy-containing motions is determined by the spanwise computational box size. The temporal evolution of these largest motions would therefore be reasonably well resolved by the flow quantities obtained by averaging over the computational domain, as also shown in Hwang & Bengana (2016). Using this approach, here we investigate the temporal evolution of each element in the self-sustaining process, and relate it with generation of turbulent skin-friction drag by the largest scale in the given computational

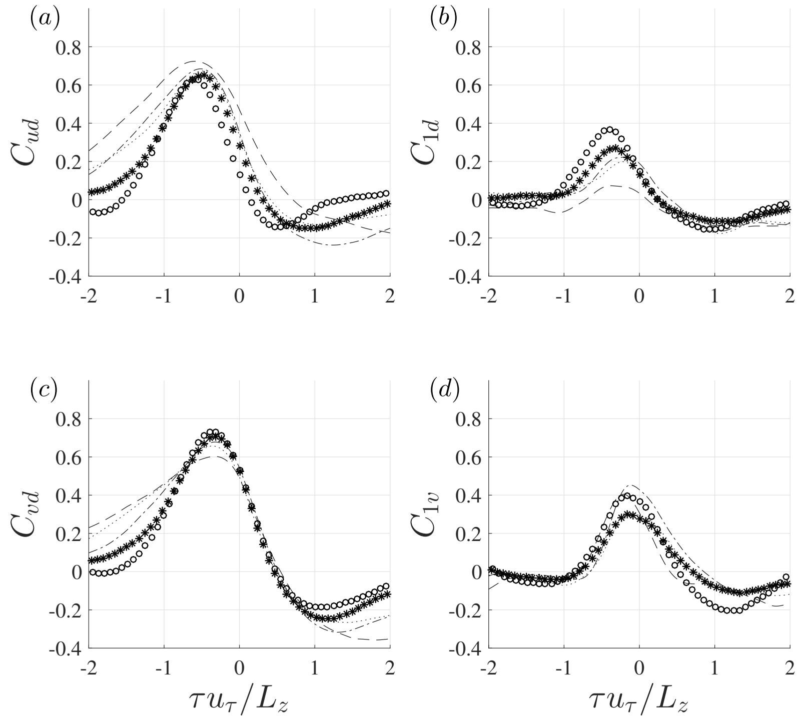

Figure 5.5: Cross-correlation functions obtained with the box-confinement approach ($\lambda_{z,t} = L_z$): (a) C_{ud}; (b) C_{1d}; (c) C_{vd}; (d) C_{1v}. Here, – – – –, $L_z = 1h$; ·········, $L_z = 0.75h$; –·–·–, $L_z = 0.5h$; $*$ $L_z = 0.3h$; $\circ$ $L_z = 0.2h$.

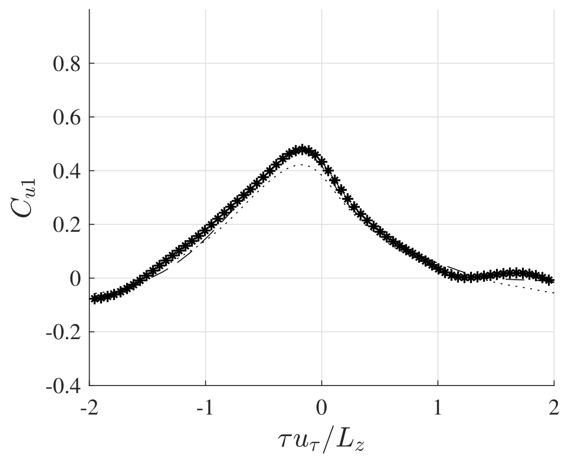

Figure 5.6: Cross-correlation functions obtained with the box-confinement approach ($\lambda_{z,t} = L_z$), C_{u1}: – – – –, $L_z = 1h$; ·········, $L_z = 0.75h$; –·–·–, $L_z = 0.5h$; $*$ $L_z = 0.3h$.

domain. For this purpose, we first introduce the following four integral quantities of interest:

$$E_u = \frac{1}{2L_xL_z}\int_0^{L_z}\int_0^{2/3L_z}\int_0^{L_x} u'^2 \ dxdydz, \tag{5.1a}$$

$$E_v = \frac{1}{2L_xL_z}\int_0^{L_z}\int_0^{2/3L_z}\int_0^{L_x} v'^2 \ dxdydz, \tag{5.1b}$$

$$E_1 = \int_0^{2/3L_z} |\hat{u}(y,k_x,k_z)|^2 + |\hat{v}(y,k_x,k_z)|^2 + |\hat{w}(y,k_x,k_z)|^2 \ dy, \tag{5.1c}$$

$$E_d = \frac{1}{L_xL_z}\int_0^{L_z}\int_0^{L_x} \tau_w \ dxdz, \tag{5.1d}$$

where $k_x = 2\pi/L_z$ and $k_z = 2\pi/L_z$, and τ_w is the instantaneous wall shear stress. Here, we note that the wall-normal domain for the integrals in (5.1) is defined to be $y \in [0, 2/3L_z]$ to include the most energetic part of the self-similar self-sustaining motions in each computational domain (see also Hwang & Bengana, 2016, for further details). We also note that E_u represents the streaks, E_v the quasi-streamwise vortices, and E_1 the streamwise meandering motions caused by streak instability, respectively, and their definitions exactly follow Hwang & Bengana (2016) where their physical relevance is extensively discussed. In the present study, we also introduce E_d, which would represent the instantaneous wall shear stress of the largest scale permitted by the given computational domain. However, one should bear in mind that E_d is not a full representation of the skin-friction generation by the largest structures in the domain, as it would not completely exclude the effect of smaller-scale structures on large-scale turbulent skin-friction generation.

To find exactly at which point in the self-sustaining process the skin-friction drag becomes maximised, we then compute temporal cross-correlation among these quantities in (5.1), such that:

$$C_{ij}(\tau) = \frac{\overline{E_i(t+\tau)E_j(t)}}{\sqrt{\overline{E_i^2}(t)}\sqrt{\overline{E_j^2}(t)}}, \tag{5.2}$$

with $i,j = u, v, 1, d$ from (5.1). Since an extensive discussion on the correlations among E_u, E_v, and E_1 was given in Hwang & Bengana (2016), the focus in the present study will be mainly given to understanding of the cross-correlations involving the spatially-averaged wall shear stress, i.e E_d. In order to investigate the characteristics of the self-similar drag generation, we introduce the concept of self-similar time scale, defined accordingly as $\tau u_\tau/L_z$ $(= \tau^+/L_z^+)$.

The computed correlations, C_{ud}, C_{1d}, C_{vd} and C_{uv}, are shown in fig. 5.5 for several different values of the spanwise domain size L_z. The cross correlations with E_d reveal that at least their peak locations scale well with respect to the self-similar time scale. The correlations are also quite large: the peak values of C_{ud} and C_{vd} are greater than 0.6. In the cross correlations, the peak location of C_{ud} is found to be at $\tau \approx -0.6$ (fig. 5.5*a*), while those of C_{1d} and C_{vd} are at $\tau \approx -0.3 \sim -0.1$ (figs 5.5*b* and *c*). Unfortunately, it is difficult to find clear difference between the peak locations of C_{1d} and C_{vd}. This is presumably because the streak instability, represented by E_1, is a fast dynamical process, as shown in Hwang & Bengana (2016). Further to this, it should be noted that all the flow quantities in (5.1) contain some effect of smaller-scale motions. In other words, these quantities do not precisely represent the structure of interest, yielding another complication. Nonetheless, the correlation C_{1v} in fig. 5.5(*d*) clearly shows that the amplification of E_1 emerges before E_v reaches a large amplitude, consistent with Hwang & Bengana (2016). This evidence appears to indicate that the streamwise fluctuations would appear chronologically in between E_u and E_v, i.e. the streaks and the quasi-streamwise vortices. This is confirmed by visualising the correlation quantity C_{u1}, in fig. 5.6, where it can be observed that the streamwise meandering motion is subsequent to the largest amplitude of the streak. The cross correlations in fig. 5.5 therefore suggest that the sequence of the excursion of E_u (streak), E_1 (streak instability), E_v (streamwise vortical structure) and E_d (skin-friction generation) would be cyclically given as:

$$E_u \rightarrow E_1 \rightarrow E_v \rightarrow E_d, \tag{5.3}$$

The self-sustaining process is essentially a cyclic process represented by $E_u \rightarrow E_1 \rightarrow E_v$ with the single turn-over time scale of $Tu_\tau/L_z \simeq 2$ (Hwang & Bengana, 2016), and the process of $E_v \rightarrow E_u$ should follow with occurrence of the next cycle. Given the small time scale of the physical process of $E_v \rightarrow E_d$ at $\Delta\tau u_\tau/L_z \approx 0.1 \sim 0.3$ (fig. 5.5*c*), the only conclusion we can reach here would therefore be that the large amplification of E_d appears in the process of $E_v \rightarrow E_u$: i.e. the skin-friction generation by the largest structure (E_d) takes place when the streamwise vortices (E_v) are converted to the streak (E_u). This conversion of vortices to streaks is exactly the lift-up process, and the small time scale of the process of $E_v \rightarrow E_d$ suggests that the skin-friction generation is dominant at the early stage of the lift-up process. This observation is also consistent with the numerical experiment in Hwang & Bengana (2016) where the artificial suppression of the lift-up effect of the energy-containing motions in the logarithmic and outer regions was found to yield significant amounts of skin-friction reduction. Finally, it is important to highlight that the lift-up effect is a linear process, which is well described by the Navier-Stokes equation linearised around the mean flow (e.g. Cossu *et al.*, 2009; Hwang & Cossu, 2010*b*). Therefore, performing a linear analysis to understand skin-friction generation would provide a useful physical insight, as already demonstrated by a number of previous studies (e.g. Blesbois *et al.*, 2013; Lim & Kim, 2004; Luhar *et al.*, 2014; Moarref & Jovanović, 2012).

5.3.2 Scale interaction and skin-friction generation

Although the three independent assessment methods in the present study consistently suggest that turbulent skin friction at sufficiently high Reynolds numbers is dominantly generated by self-similar motions in the logarithmic region, an important difference between the FIK-identity-based approach and the other two approaches has also been observed (fig. 5.1). This difference originates from the fact that the FIK-identity-based approach computes contribution of the motions at $\lambda_z \leq \lambda_{z,t}$ in the presence of all the structures, whereas the other two approaches actually remove the motions at $\lambda_z > \lambda_{z,t}$ during the simulation and calculate the skin friction with the remaining motions. It is evident that this large difference would not have been observed if there was no interaction among the energy-containing motions at different length scales.

To further understand the related scale interaction, one-dimensional spanwise wavenumber spectra from the LESs with a sufficiently large spanwise domain ($F2000$), a confined box with $L_z = 0.5h$, and an artificial damping applied to $F2000$ with $\lambda_{z,t} = 0.5h$ are compared in fig. 5.7. The spectra with the confined box and the artificial damping are quite different from those of the full simulation particularly near $\lambda_z \simeq \lambda_{z,t}$. However, the two approaches, both of which physically remove the motions at $\lambda_z > \lambda_{z,t}$ from the simulations, do not yield very significant difference from each other in their spectra (see also fig. 5.1). Overall, the spectral density of all the flow variables with the box-confinement approach and the artificial damping is found to be elevated compared to that of the full simulation particularly at the wall-normal location where the removed motions originally reside. Furthermore, this influence persists over a fairly wide range of the spanwise wavelength: the wall-normal velocity and the spanwise velocity spectra show non-negligibly large distortions even at $\lambda_z^+ \simeq 100 \sim 200$ (figs 5.7*b*, *c*). This indicates that the scale interaction is not localised only near the cut-off wavelength, $\lambda_z \simeq \lambda_{z,t}$.

The generation of such a 'tall' turbulent fluctuation both in the simulations with the box-confinement and the artificial damping is reminiscent of the feature commonly observed in the minimal channel simulations using a small spanwise domain (e.g. Hwang, 2013, 2015; Jiménez

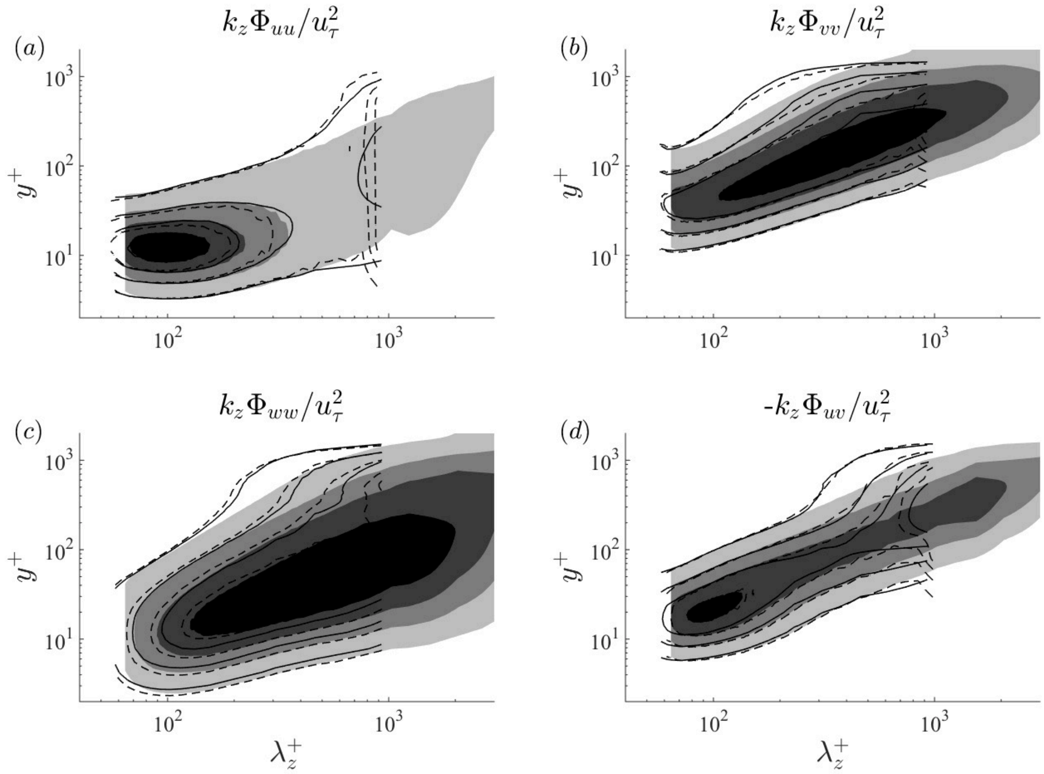

Figure 5.7: Premultiplied one-dimensional spanwise wavenumber spectra of (a) streamwise, (b) wall-normal, (c) spanwise velocities, and (d) Reynolds shear stress. Here, the shaded, solid, and dashed contours indicate the full domain simulation ($F2000$), the box-confinement approach, and the artificial damping applied to $F2000$, respectively. For the box-confinement approach and the artificial damping, the cut-off spanwise wavelength is $\lambda_{z,t} = 0.5h$. The contour labels are chosen to be 0.2, 0.4, 0.6, 0.8 times each of the maximum for comparison.

& Pinelli, 1999). In the minimal channel, such a fluctuation has been understood to be induced by the remaining self-sustaining motions, as its removal does not significantly affect the statistics and dynamics of the remaining motions. Here, the appearance of such a fluctuation also with the artificial damping suggests that this is not a specific behaviour observed only in the confined spanwise domain, but may be an important general physical feature associated with a scale interaction occurring in the remaining motions. The spectra show that this fluctuation is responsible for generation of a considerable amount of Reynolds shear stress over a range of spanwise wavelength (fig. 5.7*d*), explaining why the skin friction obtained by the box-confinement approach and the artificial damping is elevated than what is expected by the FIK identity.

Although the generation mechanism of the tall fluctuation is not entirely clear at the moment, a dimensional analysis, similar to the one given by Jiménez & Pinelli (1999), provides a physical insight into a possible origin of this behaviour. In a full-domain simulation, the production in the logarithmic region would be $\mathcal{P} \sim u_\tau^3/y$, while dissipation is $\mathcal{E} \sim \nu\omega^2$ where ω is denoted as the total vorticity fluctuation. If the production and the dissipation are assumed to be locally balanced at each wall-normal location, this yields $\omega \sim 1/y^{1/2}$, indicating that the vorticity fluctuation would decay with y. However, in the simulations with a narrow spanwise domain width L_z where the motions at $\lambda_z > L_z$ are not resolved, the production of the largest energy-containing motions resolved would be $\mathcal{P} \sim u_\tau^3/L_z$ due to $\lambda_z \sim y$. Therefore, the resulting ω would become $\omega \sim 1/L_z^{1/2}$, indicating that the vorticity fluctuation in a confined spanwise domain would not significantly decay along the wall-normal direction, at least to some extent. Furthermore, the dimensional analysis indicates that the vorticity fluctuation would 'increase' as L_z is decreased.

Fig. 5.8 reports the vorticity fluctuations for several L_z in the box-confinement approach (i.e. $\lambda_{z,t} = L_z$). Despite the fact that the present numerical experiments are based on a set of large-eddy simulations, all the vorticity fluctuations indeed appear to increase on decreasing L_z, consistent with the dimensional analysis above. This behaviour is particularly prominent in the wall-normal vorticity statistics, and the wall-normal distribution also appears to be roughly constant for $10^2 < y^+ < 10^3$. This observation indicates that the dimensional analysis provides at least a partial explanation for the origin of the tall fluctuation. Given the dimensional analysis simply relying on the balance between production and dissipation, it is also important to mention that the mechanism of generation of the tall fluctuation would be associated with the energy cascade rather than the energy extraction of the large eddies from mean shear. In this respect, it is worth mentioning the recent work by Cimarelli *et al.* (2016), who showed the presence of

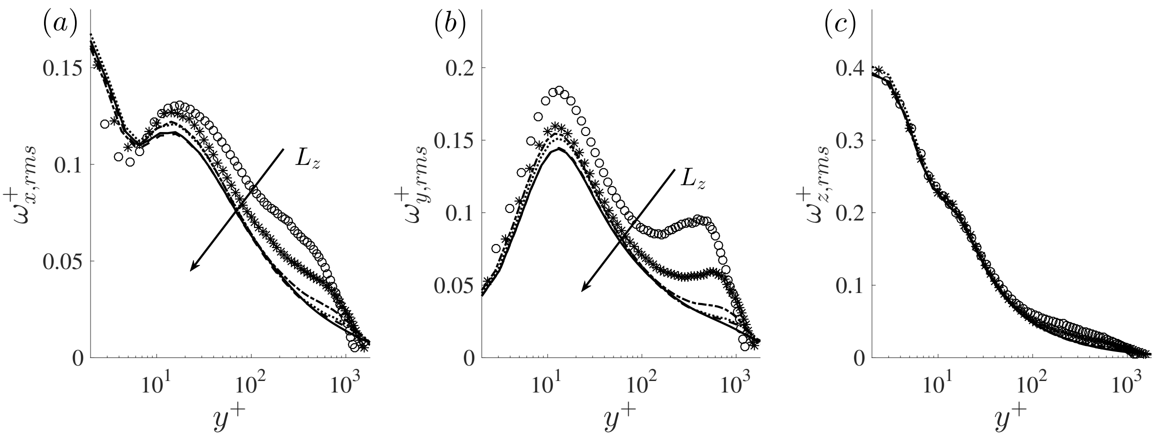

Figure 5.8: Vorticity fluctuations for different L_z with the box-confinement approach ($\lambda_{z,t} = L_z$): (a) $\omega^+_{x,rms}$; (b) $\omega^+_{y,rms}$; (c) $\omega^+_{z,rms}$. Here, ——, $L_z = 1.5h$; - - - -, $L_z = 1h$; ·········, $L_z = 0.75h$; −·−·−, $L_z = 0.5h$; $*$ $L_z = 0.3h$; $\circ$ $L_z = 0.2h$.

the wall-normal energy flux progressing from smaller to larger attached eddies located further from the wall. This process might be related to the generation of the tall fluctuation, although other possible origins of the tall fluctuation should not be excluded.

Finally, it should be pointed out that all the spectra in fig. 5.7 exhibit fairly good inner-scaling for $y^+ < 100 \sim 200$ and $\lambda_z^+ < 100 \sim 200$. However, this does not necessarily mean that the original near-wall motions in the full simulation are not affected by the removal of the motions at $\lambda_z \simeq \lambda_{z,t}$. It should be stressed that the removal of large-scale motions either by the box-confinement approach or by the artificial damping reduces the skin friction, resulting in a reduced friction velocity. In other words, the good inner-scaling nature of the spectra near $\lambda_z^+ \simeq 100$ in all the three simulations precisely implies that the removal of the motions at $\lambda_z \simeq \lambda_{z,t}$ makes the near-wall motions resettled such that they scale well with the 'new' inner units given by the reduced friction velocity.

The scale-interaction process discussed above is also directly supported by the Reynolds-shear-stress distribution, as shown in fig. 5.9. Here, we note that both of the box-confinement approach and the artificial damping are designed not to change the FIK identity itself. Therefore, the Reynolds-shear-stress profiles, normalised by $2U_m$, are supposed to be directly related to their contribution to turbulent skin-friction through the FIK identity in (2.32). Not surprisingly, all the Reynolds-shear-stress profiles obtained by applying the three approaches are overall smaller than that of full DNS. The profile obtained with the FIK-identity-based approach is almost

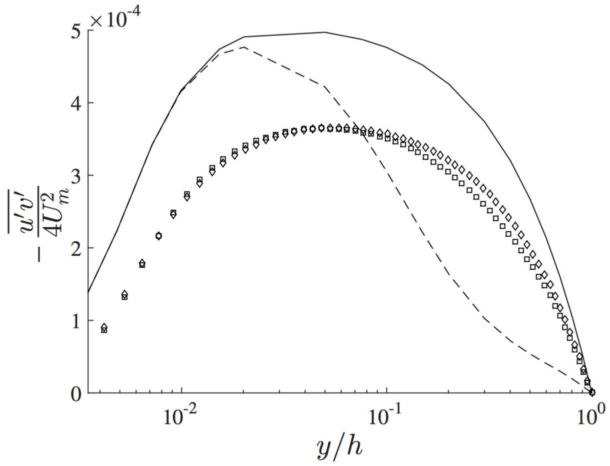

Figure 5.9: Comparison of the Reynolds shear stress: ——, DNS (Hoyas & Jiménez, 2006); - - - -, FIK-identity-based approach; $\diamond$, box-confinement approach; $\square$, artificial damping of $F2000$. Here, the cut-off spanwise wavelength applied is $\lambda_{z,t} = 0.5h$.

identical to that of full DNS for $y/h \lesssim 0.01$, but is very different from those with the box-confinement approach and the artificial damping. In the region close to the wall ($y/h \lesssim 0.06$), the application of the FIK-identity-based approach to full DNS data yields larger Reynolds shear stress than those with the other two approaches. This suggests that removing the motions larger than a given length scale indeed affects the near-wall motions such that they are adjusted to the reduced friction velocity. On the other hand, in the region relatively further from the wall ($y/h \gtrsim 0.06$), both of the box-confinement approach and the artificial damping exhibit larger Reynolds shear stress than that obtained with the FIK-identity-based approach. This indicates that the remaining motions in the absence of the motions at $\lambda_z > \lambda_{z,t}$ indeed generate additional Reynolds shear stress in this region, resulting in an elevated skin friction compared to what is expected from the FIK identity.

5.3.3 Implications to flow control

It has been constantly reported that the effectiveness of flow control strategies targeting the near-wall structures, such as opposition control (Chang *et al.*, 2002) and spanwise wall oscillations (Agostini *et al.*, 2014; Quadrio, 2011), is reduced on increasing the Reynolds number. It has often been speculated that the undesirable performance degradation with the Reynolds number would possibly be due to the energetic large-scale structures such as large-scale and very-large scale motions (Touber & Leschziner, 2012).

An explanation to this phenomenon has been provided by Luchini (1996), who postulated that the vertical shift in the law of the wall expressed in wall units is independent of Re, so that due to the well-known correspondence between the additive constant in the log law and the drag, the Reynolds-number effect can be explained by the intrinsic reduction of C_f at increasing values of Re (see (1.1)). The present finding suggests that this behaviour is due to a large number of self-similar energy-containing structures in the form of Townsend's attached eddies, most of which populate in the logarithmic region. In this respect, the trends shown by Hwang (2013) have been successfully extended to much higher Reynolds numbers (fig. 5.2*b*).

It is also important to remember that the inhibition of the largest structures at scales $\lambda_z \geq 1.5h$ (i.e. VLSMs and LSMs) does not yield sufficiently large amounts of drag reduction, possibly due to the scale interaction discussed, even though they are expected to be responsible to $25 \sim 30\%$ of total skin friction at $Re_\tau = 2000$ according to the FIK-identity-based approach (fig. 5.1): the removal of the motions at $\lambda_z \geq 0.75h$ by both of the box-confinement and the artificial damping approaches have reduced only $7 \sim 8\%$ of total skin friction. These levels of performance are a little discouraging, especially given the fact that the streamwise grooved surface (riblet), which does not require any external energy input to the system, has been shown to potentially give similar amounts of drag reduction, at least in optimal conditions (Choi *et al.*, 1993; Spalart & McLean, 2011; Squire & Savill, 1989; Viswanath, 2002; Walsh, 1982). It is also worth noting that the amount of skin-friction reduction with the removal of the largest structures does not appear to be highly dependent upon the way of removing and/or disturbing these motions. For example, destruction of the self-sustaining process of these motions through inhibition of the lift-up effect also yielded 8% of skin-friction reduction at $Re_\tau \simeq 950$ (Hwang & Bengana, 2016), a value not very different from that obtained here. Of course, it is still too early to conclude that this value would be the largest amount of drag reduction possible by inhibiting the largest structures.

Despite this discouraging postulation, it is still hopeful to observe the outer-scaling behaviour of the normalised skin friction with gradual removal of the motions from the largest scale (see fig. 5.3). This observation suggests that a drag reduction of $20 \sim 30\%$ may be achievable with an array of actuators and/or sensors, the size of which is only an order of magnitude smaller than the outer length scale. Since the boundary-layer thickness over wing or surface of a commercial aircraft is $O(1\text{cm})$ (Kasagi *et al.*, 2009), the expected size of the actuators and sensors would be $O(1\text{mm})$, significantly relieving the micro-scale design restriction posed by targeting the near-wall structures (Kasagi *et al.*, 2009).

‘

6

Conclusions

Thus far, results have been presented concerning the dynamics and role of coherent structures in a turbulent channel flow, with special reference to Townsend's theory of attached eddies. We summarise the main outcomes as follows:

1. Initially, we have examined the instability of an 'amplified' streaky motion in the outer layer, artificially driven by the optimal forcing computed in Hwang & Cossu (2010*a*). As the forcing amplitude is gradually increased, a streamwise-uniform streak, reminiscent of VLSM, is successfully introduced. We have shown that an energetic cross-streamwise velocity structure emerges at the streamwise length scale $\lambda_x/h = 1 - 2$, and this structure produces all the typical statistical features of the LSM. All diagnosis tools employed (the cross-streamwise turbulence statistics, DMD analysis and energy-production analysis) firmly indicate that the origin of this structure is a sinuous-mode streak instability, the existence of which had only been previously postulated. Consequently, it has been proposed that the streak instability mechanism determines the streamwise length scales of the LSM and the VLSM. Nonetheless, we should also mention that this picture is potentially compatible with the theory of broadband forcing, because the predictions of both theories are largely determined by the properties of the same linear operator, al least for the problem at hand. Although it should not be treated as definitive evidence, it should be mentioned that the emergence of the correct streamwise length scale would be more complex to explain in the framework of broadband forcing.

2. Subsequently, the same technique has been applied to the logarithmic layer, as we sought to unveil the formation mechanism of the self-similar vortex clusters in this region (del

Álamo *et al.*, 2006). Turbulence statistics indicate the emergence of vortical structures significantly contributing to the cross-streamwise turbulent kinetic energy, in a fashion that closely resembles the results obtained in the outer layer. In particular, it is shown that the streak instability mechanism can initiate the vortical structures mainly composed of cross-streamwise velocity components, and their size is characterised in a self-similar manner, as follows:

$$\lambda_x \simeq 2 - 3\lambda_z, \tag{6.1a}$$

$$y \simeq 0.3 - 0.7\lambda_z. \tag{6.1b}$$

It should be stressed that the size of the vortical structure is strikingly similar to that of the vortex packets often called the hairpin vortex packets Tomkins & Adrian (2003) or the tall-attached vortex clusters del Álamo *et al.* (2006), and that this is also comparable in the vortical structures of the self-sustaining attached eddies in Hwang (2015). These results support the existence of the self-sustaining process in the logarithmic layer, and suggest that the streak instability is the mechanism behind the formation of the vortical structures (Hwang, 2015; Hwang & Bengana, 2016; Hwang & Cossu, 2010*c*).

3. Finally, we have assessed contribution of the energy-containing motions to turbulent skin friction at sufficiently high Reynolds numbers. In particular, skin-friction generation by the motions, the spanwise size of which is smaller than a given cut-off wavelength (i.e. $\lambda_z \leq \lambda_{z,t}$), has been quantified by employing three different approaches: 1) FIK-identity-based approach; 2) box-confinement approach; 3) artificial damping. The near-wall motions have been found to continuously lose their importance on increasing the Reynolds number, consistent with the previous finding at low Reynolds numbers (Hwang, 2013). However, interestingly, the largest structures (i.e. very-large-scale and large-scale motions) given at $\lambda_z = 1.5h$ have also been found to be of limited importance: although the FIK-identity-based approach shows that the largest motions at $\lambda_z = 1.5h$ (i.e. large-scale and very-large-scale motions) are responsible for $20 \sim 30\%$ of total skin friction at $Re_\tau \simeq 2000$, their actual removal by the box-confinement and the artificial damping approaches yields only $5 \sim 8\%$ of skin-friction reduction, possibly due to a non-trivial scale interaction. All the three methods have consistently revealed that the largest amount of skin-friction is generated by the self-similar energy-containing motions, the spanwise size of which lies between $\lambda_z^+ \simeq 100$ and $\lambda_z \simeq 1.5h$ at sufficiently high Reynolds numbers. These motions essentially belong

to the logarithmic region in the sense that their size is proportional to the distance from the wall (Hwang, 2015), and their contribution has been found to gradually increase with the value of Re_τ, eventually being responsible for most of turbulent skin-friction generation. The significance of attached eddies to drag is also shown by the probability density function of wall-shear stress, which retains its fundamental characteristics of positive skewness even with the removal of the largest eddies. Additionally, it has been shown that the normalised skin-friction reduction with respect to the cut-off spanwise wavelength $\lambda_{z,t}$ scales in outer units (fig. 5.3), at least in the range of Reynolds number investigated in the present study.

6.1 Further work

Although novel evidence has been presented on the self-sustaining process, some questions still remain to be answered in this respect: for instance, the exact linear and/or non-linear mechanisms that follow the streak instability are not completely clear. In any case, these findings unveil the importance of non-linear processes in understanding the mechanism of the streamwise length-scale determination, and this may play a crucial role in developing low-order models for coherent structures at high Reynolds numbers.

The assessment on the contribution of attached eddies to skin friction carries ramifications for flow control, and especially for drag reduction at Reynolds numbers that approach industrially relevant conditions. It appears that any method, in order to be effective, should aim at controlling the self-similar energy-containing motion. However, the generation of skin-friction appears to be a multi-scale process, involving significant scale interaction across the logarithmic layer, of which little is currently known. This suggests that designing a practically realizable flow controller would be highly challenging. Simple trial and error approaches would be unlikely to work for this problem, and much more innovative and systematic approaches need to be taken with very careful inspection of the given system.

References

Abe, H., Kawamura, H. & Choi, H. 2004 Very large-scale structures and their effects on the wall shear-stress fluctuations in a turbulent channel flow up to $Re_\tau = 640$. *J. Fluids Eng.* **126** (5), 835. 9

Adrian, R. J. 2007 Hairpin vortex organization in wall turbulence. *Phys. Fluids* **19**, 041301. 7, 10, 52

Adrian, R. J, Balachandar, S. & Liu, Z. C. 2001 Spanwise growth of vortex structure in wall turbulence. *KSME Int. J.* **15** (12), 1741–1749. 10

Adrian, R. J. & Liu, Z. C. 2002 Observation of vortex packets in direct numerical simulation of fully turbulent channel flow. *J. Vis.* **5** (1), 9–19. 7

Adrian, R. J., Meinhart, C .D. & Tomkins, C. D. 2000 Vortex organization in the outer region of the turbulent boundary layer. *J. Fluid Mech.* **422**, 1–54. 7

Agostini, L., Touber, E. & Leschziner, M. A. 2014 Spanwise oscillatory wall motion in channel flow: drag-reduction mechanisms inferred from DNS-predicted phase-wise property variations at $Re_\tau = 1000$. *J. Fluid Mech.* **743**, 606–635. 8, 94

del Álamo, J. C. & Jiménez, J. 2003 Spectra of the very large anisotropic scales in turbulent channels. *Phys. Fluids* **15** (6), 41–44. 6, 24

del Álamo, J. C. & Jiménez, J. 2006 Linear energy amplification in turbulent channels. *J. Fluid Mech.* **559**, 205–213. 3, 23, 54

del Álamo, J. C. & Jiménez, J. 2009 Estimation of turbulent convection velocities and corrections to Taylor's approximation. *J. Fluid Mech.* **640**, 5–26. 48

del Álamo, J. C., Jiménez, J., Zandonade, P. & Moser, R. D. 2006 Self-similar vortex clusters in the turbulent logarithmic region. *J. Fluid Mech.* **561**, 329–358. 5, 10, 32, 68, 78, 97, 98

Alizard, F. 2015 Linear stability of optimal streaks in the log-layer of turbulent channel flows. *Phys. Fluids* **27**, 105103. 7, 40, 44, 50, 52, 72, 76, 78

Andersson, P., Brandt, L., Bottaro, A. & Henningson, D. S. 2001 On the breakdown of boundary layer streaks. *J. Fluid Mech.* **428**, 29–60. 40, 44, 46, 65, 66

Argyropoulos, C. D. & Markatos, N. C. 2015 Recent advances on the numerical modelling of turbulent flows. *Appl. Math. Model.* **39** (2), 693–732. 14

Asai, M., Minagawa, M. & Nishioka, M. 2002 The instability and breakdown of a near-wall low-speed streak. *J. Fluid Mech.* **455**, 289–314. 66

Baars, W. J., Talluru, K. M., Hutchins, N. & Marusic, I. 2015 Wavelet analysis of wall turbulence to study large-scale modulation of small scales. *Exp. Fluids* **56** (10), 1–15. 83

Baltzer, J. R., Adrian, R. J. & Wu, X. 2013 Structural organization of large and very large scales in turbulent pipe flow simulation. *J. Fluid Mech.* **720**, 236–279. 7, 10, 51

Belan, M. & Quadrio, M. 2013 A perturbative model for predicting the high-Reynolds-number behaviour of the streamwise travelling waves technique in turbulent drag reduction. *ZAMM - J. Appl. Math. Mech. / Zeitschrift für Angew. Math. und Mech.* **93** (12), 944–962. 8

Bernardini, M., Pirozzoli, S. & Orlandi, P. 2014 Velocity statistics in turbulent channel flow up to $Re_\tau = 4000$. *J. Fluid Mech.* **742**, 171–191. 17, 18, 21

Bewley, T. R., Moin, P. & Temam, R. 2001 Dns-based predictive control of turbulence: an optimal benchmark for feedback algorithms. *J. Fluid Mech.* **447**, 179–225. 15

Blackwelder, R. F. & Eckelmann, H. 1979 Streamwise vortices associated with the bursting phenomenon. *J. Fluid Mech.* **94**, 577–594. 2

Blesbois, O., Chernyshenko, S. I., Touber, E. & Leschziner, M. A. 2013 Pattern prediction by linear analysis of turbulent flow with drag reduction by wall oscillation. *J. Fluid Mech.* **724**, 607–641. 90

Bushnell, D. M. 2002 Aircraft drag reduction - a review. *J. Aerosp. Eng.* **217**, 1–18. 79

Butler, K. M. & Farrell, B. F. 1993 Optimal perturbations and streak spacing in wall-bounded turbulent shear flow. *Phys. Fluids* **5** (3), 774–777. 3

Canton, J., Örlü, R., Chin, C. & Schlatter, P. 2016 Reynolds number dependence of large-scale friction control in turbulent channel flow. *Phys. Rev. Fluids* **1**, 081501. 36, 43

Cantwell, B. J. 1981 Organised Motion in Turbulent Flow. *Annu. Rev. Fluid Mech.* **13** (1), 457–515. 1

Cassinelli, A., de Giovanetti, M. & Hwang, Y. 2017 Streak instability in near-wall turbulence revisited. *J. Turbul.* **18** (5), 443–464. 39, 40, 52, 64, 66

Chang, Y., Collis, S. S. & Ramakrishnan, S. 2002 Viscous effects in control of near-wall turbulence. *Phys. Fluids* **14** (11), 4069–4080. 8, 85, 94

Chernyshenko, S. I. & Baig, M. F. 2005*a* Streaks and vortices in near-wall turbulence. *Philos. Trans. R. Soc. A Math. Phys. Eng. Sci.* **363** (1830), 1097–1107. 3

Chernyshenko, S. I. & Baig, M. F. 2005*b* The mechanism of streak formation in near-wall turbulence. *J. Fluid Mech.* **544**, 99–131. 3, 86

Chernyshenko, S. I., Marusic, I. & Mathis, R. 2012 Quasi-steady description of modulation effects in wall turbulence. *arXiv:1203.3714v1 [physics.flu-dyn]* p. 16, arXiv: 1203.3714. 83

Choi, H., Moin, P. & Kim, J. 1993 Direct numerical simulation of turbulent flow over riblets. *J. Fluid*

Mech. **255**, 503–539. 95

Choi, H., Moin, P. & Kim, J. 1994 Active turbulence control for drag reduction in wall-bounded flows. *J. Fluid Mech.* **262**, 75–110. 2, 8

Cimarelli, A., De Angelis, E., Jiménez, J. & Casciola, C. M. 2016 Cascades and wall-normal fluxes in turbulent channel flows. *J. Fluid Mech.* **796**, 417–436. 92

Corrsin, S. 1961 Turbulent Flow. *Am. Sci.* **49** (3), 300–325. 13

Cossu, C., Pujals, G. & Depardon, S. 2009 Optimal transient growth and very largescale structures in turbulent boundary layers. *J. Fluid Mech.* **619**, 79–94. 3, 7, 54, 86, 90

De Graaff, D. B. & Eaton, J. K. 2000 Reynolds-number scaling of the flat-plate turbulent boundary layer. *J. Fluid Mech.* **422**, 319–346. 4

Dean, R.B. 1978 Reynolds number dependence of skin friction and other bulk flow variables in two-dimensional rectangular duct flow. *Trans. ASME J. Fluid Eng.* **100**, 215–223. 18, 21, 81

Deardorff, J. W. 1970 A numerical study of three-dimensionnal turbulent channel flow at large Reynolds numbers. *J. Fluid Mech.* **41**, 453–480. 13

Deck, S., Renard, N., Laraufie, R. & Weiss, P.-É. 2014 Large-scale contribution to mean wall shear stress in high-Reynolds-number flat-plate boundary layers up to $Re_\theta = 13650$. *J. Fluid Mech.* **743**, 202–248. 9, 11, 29, 80

Dukowicz, J. K. & Dvinsky, A. S. 1992 Approximate factorization as a high order splitting for the implicit incompressible flow equations. *J. Comput. Phys.* **102** (2), 336–347. 18

Falco, R. E. 1974 Some comments on turbulent boundary layer structure inferred from the movements of passive contaminants. In *AIAA 12th Aerosp. Sci. Meet.*, pp. 74–99. 6

Falco, R. E. 1991 A Coherent Structure Model of the Turbulent Boundary Layer and Its Ability to Predict Reynolds Number Dependence. *Philos. Trans. R. Soc. A Math. Phys. Eng. Sci.* **336** (1641), 103–129. 6

Farrell, B. F. & Ioannou, P. J. 1998 Perturbation structure and spectra in turbulent channel flow. *Theor. Comput. Fluid Dyn.* **11**, 237–250. 3

Flores, O. & Jiménez, J. 2006 Effect of wall-boundary disturbances on turbulent channel flows. *J. Fluid Mech.* **566**, 357–376. 6, 10

Flores, O. & Jiménez, J. 2010 Hierarchy of minimal flow units in the logarithmic layer. *Phys. Fluids* **22**, 071704. 8, 30, 32

Flores, O., Jiménez, J. & del Álamo, J. C. 2007 Vorticity organization in the outer layer of turbulent channels with disturbed walls. *J. Fluid Mech.* **591**, 145–154. 6

Fukagata, K., Iwamoto, K. & Kasagi, N. 2002 Contribution of Reynolds stress distribution to the skin friction in wall-bounded flows. *Phys. Fluids* **14** (11), 13–17. 29

Ganapathisubramani, B., Longmire, E. K. & Marusic, I. 2006 Experimental investigation of vortex properties in a turbulent boundary layer. *Phys. Fluids* **18**, 055105. 5

García-mayoral, R. & Jiménez, J. 2011 Drag reduction by riblets. *Philos. Trans. R. Soc. A Math. Phys. Eng. Sci.* **369** (1940), 1412–1427. 79

Gatti, D. & Quadrio, M. 2013 Performance losses of drag-reducing spanwise forcing at moderate values of the Reynolds number. *Phys. Fluids* **25**, 125109. 8, 85

Gayme, D. F., McKeon, B. J., Papachristodolou, A., Bamieh, B. & Doyle, J. C. 2010 A streamwise constant model of turbulence in plane couette flow. *J. Fluid Mech.* **665**, 99–119. 76

Germano, M., Piomelli, U., Moin, P. & Cabot, W. H. 1991 A dynamic subgrid-scale eddy viscosity model. *Phys. Fluids* **1760**, 8–14. 17

Guala, M., Hommema, S. E. & Adrian, R. J. 2006 Large-scale and very-large-scale motions in turbulent pipe flow. *J. Fluid Mech.* **554**, 521–542. 6

Gullbrand, J. 2000 An evaluation of a conservative fourth order DNS code in turbulent channel flow. *Cent. Turbul. Res. Annu. Briefs* pp. 211–218. 18

Hamilton, J. M., Kim, J. & Waleffe, F. 1995 Regeneration mechanisms of near-wall turbulence structures. *J. Fluid Mech.* **287**, 317–348. 2, 3, 10, 86

Head, M. R. & Bandyopadhyay, P. 1981 New aspects of turbulent boundary-layer structure. *J. Fluid Mech.* **107**, 297–338. 6

Hoepffner, J., Brandt, L. & Henningson, D. S. 2005 Transient growth on boundary layer streaks. *J. Fluid Mech.* **537**, 91–100. 52

Hoyas, S. & Jiménez, J. 2006 Scaling of the velocity fluctuations in turbulent channels up to $Re_\tau =$ 2003. *Phys. Fluids* **18**, 011702. 18, 19, 20, 21, 28, 29, 30, 41, 80, 94

Hussain, A. K. M. F. 1986 Coherent structures and turbulence. *J. Fluid Mech.* **173**, 303–356. 1

Hutchins, N. & Marusic, I. 2007*a* Evidence of very long meandering features in the logarithmic region of turbulent boundary layers. *J. Fluid Mech.* **579**, 1–28. 5, 6

Hutchins, N. & Marusic, I. 2007*b* Large-scale influences in near-wall turbulence. *Philos. Trans. R. Soc. A Math. Phys. Eng. Sci.* **365** (1852), 647–664. 4, 6, 9, 10, 38, 51

Hwang, Y. 2013 Near-wall turbulent fluctuations in the absence of wide outer motions. *J. Fluid Mech.* **723**, 264–288. 4, 5, 9, 15, 29, 31, 82, 85, 90, 95, 98, 115

Hwang, Y. 2015 Statistical structure of self-sustaining attached eddies in turbulent channel flow. *J. Fluid Mech.* **767**, 254–289. 5, 6, 10, 11, 24, 29, 31, 41, 51, 52, 68, 78, 85, 86, 90, 98, 99

Hwang, Y. 2016 Mesolayer of attached eddies in turbulent channel flows. *Phys. Rev. Fluids* **1**, 064401. 5, 57, 70

Hwang, Y. & Bengana, Y. 2016 Self-sustaining process of minimal attached eddies in turbulent channel flow. *J. Fluid Mech.* **795**, 708–738. 6, 7, 8, 11, 36, 51, 52, 53, 63, 78, 86, 88, 89, 95, 98, 111, 112

Hwang, Y. & Cossu, C. 2010*a* Amplification of coherent streaks in the turbulent Couette flow: an inputoutput analysis at low Reynolds number. *J. Fluid Mech.* **643**, 333–348. 7, 50, 97

Hwang, Y. & Cossu, C. 2010*b* Linear non-normal energy amplification of harmonic and stochastic forcing in the turbulent channel flow. *J. Fluid Mech.* **664**, 51–73. 3, 7, 10, 21, 23, 24, 35, 54, 66, 86, 90

Hwang, Y. & Cossu, C. 2010*c* Self-sustained process at large scales in turbulent channel flow. *Phys. Rev. Lett.* **105** (4), 1–10. 5, 6, 10, 29, 30, 32, 52, 98

Hwang, Y. & Cossu, C. 2011 Self-sustained processes in the logarithmic layer of turbulent channel flows. *Phys. Fluids* **23**, 061702. 5, 6, 10, 11, 30, 32, 78

Hwang, Y., Willis, A. P. & Cossu, C. 2016 Invariant solutions of minimal large-scale structures in turbulent channel flow for Re_τ up to 1000. *J. Fluid Mech.* **802**, R1. 50, 52, 73

Jeong, J. & Hussain, F. 1997 Coherent structures near the wall in a turbulent channel flow. *J. Fluid Mech.* **332**, 185–214. 2

Jiménez, J. 2013*a* How linear is wall-bounded turbulence? *Phys. Fluids* **25**, 110814. 3, 8, 52

Jiménez, J. 2013*b* Near-wall turbulence. *Phys. Fluids* **25**, 101302. 8, 52

Jiménez, J., del Álamo, J. C. & Flores, O. 2004 The large-scale dynamics of near-wall turbulence. *J. Fluid Mech.* **505**, 179–199. 3

Jiménez, J. & Hoyas, S. 2008 Turbulent fluctuations above the buffer layer of wall-bounded flows. *J. Fluid Mech.* **611**, 215–236. 4

Jiménez, J. & Pinelli, A. 1999 The autonomous cycle of near-wall turbulence. *J. Fluid Mech.* **389**, 335–359. 4, 90, 92

Jimenez, J. & Moin, P. 1991 The minimal flow unit in near-wall turbulence. *J. Fluid Mech.* **225**, 231–240. 2, 4

Jovanović, M. R. & Bamieh, B. 2001 Adaptive Control of Wall-Turbulence for Skin Friction Drag Reduction and Some Consideration for High Reynolds Number Flows. In *Proc. of the 40th IEEE Conf. on Decision and Control*, pp. 4944–4949. 3

Jovanović, M. R., Schmid, P. J. & Nichols, J. W. 2014 Sparsity-promoting dynamic mode decomposition. *Phys. Fluids* **26**, 024103. 26, 28, 35

Jung, W., Mangiavacchi, N. & Akhavan, R. 1992 Suppression of turbulence in wallbounded flows by highfrequency spanwise oscillations. *Phys. Fluids* **4** (8), 1605–1607. 8

von Kármán, T. 1930 *Mechanische Ähnlichkeit und Turbulenz*. Weidmannsche Buchh. 2

Kasagi, N., Suzuki, Y. & Fukagata, K. 2009 Microelectromechanical SystemsBased Feedback Control of Turbulence for Skin Friction Reduction. *Annu. Rev. Fluid Mech.* **41** (1), 231–251. 95

Keirsbulck, L., Labraga, L. & Gad-El-Hak, M. 2012 Statistical properties of wall shear stress fluctuations in turbulent channel flows. *Int. J. Heat Fluid Flow* **37**, 1–8. 83

Kim, H. T., Kline, S. J. & Reynolds, W. C. 1971 The production of turbulence near a smooth wall in a turbulent boundary layer. *J. Fluid Mech.* **50**, 133–160. 2

Kim, J. 2011 Physics and control of wall turbulence for drag reduction. *Philos. Trans. R. Soc. A Math. Phys. Eng. Sci.* **369** (1940), 1396–411.

Kim, J. & Lim, J. 2000 A linear process in wall-bounded turbulent shear flows. *Phys. Fluids* **12** (8), 1885–1888. 86

Kim, J., Moin, P. & Moser, R. D. 1987 Turbulence statistics in fully developed channel flow at low Reynolds number. *J. Fluid Mech.* **177**, 133–166. 2

Kim, K. C. & Adrian, R. J. 1999 Very large-scale motion in the outer layer. *Phys. Fluids* **11** (2), 417–422. 6, 51

Kline, S. J., Reynolds, W. C., Schraub, F. A. & Rundstatler, P. W. 1967 The structure of turbulent boundary layers. *J. Fluid Mech.* **30**, 741–773. 2

Korda, M. & Mezić, I. 2018 On convergence of extended dynamic mode decomposition to the koopman operator. *J. of Nonlinear Sc.* **28** (2), 687–710. 27

Kornilov, V. I. 2015 Current state and prospects of researches on the control of turbulent boundary layer by air blowing. *Prog. Aerosp. Sci.* **76**, 1–23. 79

Kovasznay, L. S. G. 1970 The Turbulent Boundary Layer. *Annu. Rev. Fluid Mech.* **2**, 95–112. 5, 51

Kovasznay, L. S. G., Kibens, V. & Blackwelder, R. F. 1970 Large-scale motion in the intermittent region of a turbulent boundary layer. *J. Fluid Mech.* **41(2)**, 283–325. 5

Kravchenko, A. G., Choi, H. & Moin, P. 1993 On the relation of near-wall streamwise vortices to wall skin friction in turbulent boundary layers. *Phys. Fluids A Fluid Dyn.* **5** (12), 3307–3309. 2, 11

Kravchenko, A. G. & Moin, P. 1997 On the effect of numerical errors in large eddy simulations of turbulent flows. *J. Comput. Phys.* **131**, 310–322. 18

Landahl, M. T. 1990 On sublayer streaks. *J. Fluid Mech.* **212**, 593– 614. 86

Lee, M. & Moser, R. D. 2015 Direct numerical simulation of turbulent channel flow up to. *J. Fluid Mech.* **774**, 395–415. 4, 18, 21, 85

Leonard, A. 1974 Energy cascade in large-eddy simulations of turbulent fluid flows. *Adv. Geophys.* **18**, 237–248. 14

Lim, J. & Kim, J. 2004 A singular value analysis of boundary layer control. *Phys. Fluids* **16** (6), 1980–1988. 90

Lozano-Durán, A. & Jiménez, J. 2014 Time-resolved evolution of coherent structures in turbulent channels: characterization of eddies and cascades. *J. Fluid Mech.* **759**, 432–471. 18, 21, 32, 115

Luchini, P. 1996 Reducing the turbulent skin friction. In *Comp. Meth. in Appl. Sc. '96*. Wiley. 9, 82

Luhar, M., Sharma, A. S. & McKeon, B. J. 2014 Opposition control within the resolvent analysis framework. *J. Fluid Mech.* **749**, 597–626. 90

Luhar, M., Sharma, A. S. & McKeon, B. J. 2015 A framework for studying the effect of compliant surfaces on wall turbulence. *J. Fluid Mech.* **768**, 415–441. 9

Marusic, I. & Kunkel, G. J. 2003 Streamwise turbulence intensity formulation for flat-plate boundary layers. *Phys. Fluids* **15** (8), 2461–2464. 4, 85

Marusic, I., Monty, J. P., Hultmark, M. & Smits, A. J. 2013 On the logarithmic region in wall turbulence. *J. Fluid Mech.* **716**, R3. 4

Mathis, R., Hutchins, N. & Marusic, I. 2009 Large-scale amplitude modulation of the small-scale structures in turbulent boundary layers. *J. Fluid Mech.* **628**, 311–337. 4, 9, 82

Mathis, R., Marusic, I., Chernyshenko, S. I. & Hutchins, N. 2013 Estimating wall-shear-stress fluctuations given an outer region input. *J. Fluid Mech.* **715**, 163–180. 4, 9, 83

McKeon, B. J. & Sharma, A. S. 2010 A critical-layer framework for turbulent pipe flow. *J. Fluid Mech.* **658**, 336–382. 7

Meneveau, C. & Katz, J. 2000 Scale-Invariance and Turbulence Models for Large-Eddy Simulations. *Annu. Rev. Fluid Mech.* **32**, 1–32. 14

Metzger, M. M. & Klewicki, J. C. 2001 A comparative study of near-wall turbulence in high and low Reynolds number boundary layers. *Phys. Fluids* **13** (3), 692–701. 3, 4

Millikan, C. B. 1938 A critical discussion of turbulent flows in channels and circular tubes. In *5th Int. Congr. Appl. Mech. Proc.* (ed. J. P. Den Hartog & H. Peters). Wiley. 4

Moarref, R. & Jovanović, M. R. 2012 Model-based design of transverse wall oscillations for turbulent drag reduction. *J. Fluid Mech.* **707**, 205–240. 3, 90

Monty, J. P., Hutchins, N., Ng, H. C. H., Marusic, I. & Chong, M. S. 2009 A comparison of turbulent pipe, channel and boundary layer flows. *J. Fluid Mech.* **632**, 431–442. 41, 51

Morrison, J. F. 2007 The interaction between inner and outer regions of turbulent wall-bounded flow. *Philos. Trans. R. Soc. A Math. Phys. Eng. Sci.* **365** (1852), 683–698. 4

Nagib, H. M. & Chauhan, K. A. 2008 Variations of von Kármán coefficient in canonical flows. *Phys. Fluids* **20**, 101518. 2

Orlandi, P. & Jimenez, J. 1994 On the generation of turbulent wall friction. *Phys. Fluids* **6** (2), 634–641. 2

Park, D. S. & Huerre, P. 1995 Primary and secondary instabilities of the asymptotic suction boundary layer on a curved plate. *J. Fluid Mech.* **283**, 249–272. 55, 68

Park, J., Hwang, Y. & Cossu, C. 2011 On the stability of large-scale streaks in turbulent Couette and Poiseulle flows. *Comptes Rendus Mec.* **339**, 1–5. 7, 40, 44, 50, 52, 72, 76, 86

Park, N., Lee, S., Lee, J. & Choi, H. 2006 A dynamic subgrid-scale eddy viscosity model with a global model coefficient. *Phys. Fluids* **18**, 125109. 17

Perry, A. E. & Chong, M. S. 1982 On the mechanism of wall turbulence. *J. Fluid Mech.* **119**, 173–217. 4, 5, 85

Perry, A. E., Henbest, S. & Chong, M. S. 1986 Theoretical and experimental study of wall turbulence. *J. Fluid Mech.* **165**, 163–199. 7, 10, 52

Perry, A. E. & Marusic, I. 1995 A wall-wake model for the turbulence structure of boundary layers. Part 1. Extension of the atatched eddy hypothesis. *J. Fluid Mech.* **298**, 389–407. 4

Piomelli, U. & Balaras, E. 2002 Wall Layer Models for Large Eddy Simulations. *Annu. Rev. Fluid Mech.* **34**, 349–374. 14

Pope, S. 2000 *Turbulent Flows*, 1st edn. Cambridge University Press. 14

Pope, S. B. 2004 Ten questions concerning the large-eddy simulation of turbulent flows. *New J. Phys.* **6**. 14

Pujals, G., García-Villalba, M., Cossu, C. & Depardon, S. 2009 A note on optimal transient growth in turbulent channel flows. *Phys. Fluids* **21**, 015109. 3, 7, 23, 54, 86

Quadrio, M. 2011 Drag reduction in turbulent boundary layers by in-plane wall motion. *Philos. Trans. R. Soc. A Math. Phys. Eng. Sci.* **369** (1940), 1428–1442. 79, 94

Renard, N. & Deck, S. 2016 A theoretical decomposition of mean skin friction generation into physical phenomena across the boundary layer. *J. Fluid Mech.* **790**, 339–367. 9, 85

Reynolds, W. C. & Hussain, A. K. M. F. 1972 The mechanics of an organized wave in turbulent shear flow. Part 3. Theoretical models and comparisons with experiments. *J. Fluid Mech.* **54(2)**, 263–288. 21, 23

Reynolds, W. C. & Tiederman, W. G. 1967 Stability of turbulent channel flow, with application to Malkus's theory. *J. Fluid Mech.* **27(2)**, 253–272. 23

Robinson, S. K. 1991 Coherent motions in the turbulent boundary layer. *Annu. Rev. Fluid Mech.* **23**, 601–639. 2

Rogallo, R. S. & Moin, P. 1984 Numerical simulation of turbulent flows. *Annu. Rev. Fluid Mech.* **16**, 99–137. 13

Rosenberg, B. J., Hultmark, M., Vallikivi, M., Bailey, S. C. C. & Smits, A. J. 2013 Turbulence spectra in smooth- and rough-wall pipe flow at extreme Reynolds numbers. *J. Fluid Mech.* **731**, 46–63. 6

Rowley, C. W., Mezić, I., Bagheri, S., Schlatter, P. & Henningson, D. S. 2009 Spectral analysis of nonlinear flows. *J. Fluid Mech.* **641** (Rowley 2005), 115. 27

Russo, S. & Luchini, P. 2016 The linear response of turbulent flow to a volume force: comparison between eddy-viscosity model and DNS. *J. Fluid Mech.* **790**, 104–127. 40

Sarghini, F., Piomelli, U. & Balaras, E. 1999 Scale-similar models for large-eddy simulations. *Phys. Fluids* **11** (6), 1596–1607. 18

Schlatter, P., Örlü, R., Li, Q., Brethouwer, G., Fransson, J. H. M., Johansson, A. V., Alfredsson, P. H. & Henningson, D. S. 2009 Turbulent boundary layers up to $Re_\theta = 2500$ studied through simulation and experiment. *Phys. Fluids* **21**, 051702. 9

Schmid, P. J. 2010 Dynamic mode decomposition of numerical and experimental data. *J. Fluid Mech.* **656**, 5–28. 26, 27, 35, 111

Schmid, P. J. & Henningson, D. S. 2001 *Stability and Transition in Shear Flows*. Springer. 24, 25, 26, 52

Schoppa, W. & Hussain, F. 1998 Genesis of longitudinal vortices in near-wall turbulence. *Meccanica* **33** (5), 489–501. 43

Schoppa, W. & Hussain, F. 2002 Coherent structure generation in near-wall turbulence. *J. Fluid Mech.* **453**, 57–108. 3, 52, 76, 86

Schultz, M. P. & Flack, K. A. 2013 Reynolds-number scaling of turbulent channel flow. *Phys. Fluids* **25**, 025104. 18, 21

Sharma, A. S. & McKeon, B. J. 2013 On coherent structure in wall turbulence. *J. Fluid Mech.* **728**, 196–238. 7

de Silva, C. M., Gnanamanickam, E. P., Atkinson, C., Buchmann, N. A., Hutchins, N., Soria, J. & Marusic, I. 2014 High spatial range velocity measurements in a high Reynolds number turbulent boundary layer. *Phys. Fluids* **26**, 025117. 83

Sirovich, L. 1987 Turbulence and the dynamics of coherent structures. I - Coherent structures. II - Symmetries and transformations. III - Dynamics and scaling. *Q. Appl. Math.* **45** (3), 561–571. 1

Smagorinsky, J. 1963 General circulation experiments wiht the primitive equations I. The basic experiment. *Mon. Weather Rev.* **91** (3), 99–164. 13

Smith, C. R. & Metzler, S. P. 1983 The characteristics of low-speed streaks in the near-wall region of a turbulent boundary layer. *J. Fluid Mech.* **129**, 27–54. 2

Spalart, P. R. & McLean, J. D. 2011 Drag reduction: enticing turbulence, and then an industry. *Philos. Trans. R. Soc. A Math. Phys. Eng. Sci.* **369**, 1556–1569. 95

Squire, L. C. & Savill, A. M. 1989 Drag measurements on planar riblet surfaces at high subsonic speeds. *Appl. Sci. Res.* **46** (3), 229–243. 95

Stadsted, O. & Moin, P. 1991 On the mechanics of 3-D turbulent boundary layer. In *Proc. Eighth Symp. Turbul. Shear Flows*. Munich. 8

Swearingen, J. D. & Blackwelder, R. F. 1987 The growth and breakdown of streamwise vortices in the presence of a wall. *J. Fluid Mech.* **182**, 255–290. 2

Tomkins, C. D. & Adrian, R. J. 2003 Spanwise structure and scale growth in turbulent boundary layers. *J. Fluid Mech.* **490**, 37–74. 5, 78, 98

Tomkins, C. D. & Adrian, R. J. 2005 Energetic spanwise modes in the logarithmic layer of a turbulent boundary layer. *J. Fluid Mech.* **545**, 141–162. 5

Touber, E. & Leschziner, M. A. 2012 Near-wall streak modification by spanwise oscillatory wall motion and drag-reduction mechanisms. *J. Fluid Mech.* **693**, 150–200. 8, 94

Townsend, A. A. 1961 Equilibrium layers and wall turbulence. *J. Fluid Mech.* **12**, 97–120. 4, 5

Townsend, A. A. 1976 *The structure of turbulent shear flow*, 1st edn. Cambridge University Press. 4, 5, 10, 29, 85, 86

Van Driest, E. R. 1956 On Turbulent Flow Near a Wall. *J. Aeronaut. Sci. (Institute Aeronaut. Sci.* **23** (11), 1007–1011. 17

Viswanath, P. R. 2002 Aircraft viscous drag reduction using riblets. *Prog. Aerosp. Sci.* **38** (6-7), 571–600. 95

Vreman, A. W. 2004 An eddy-viscosity subgrid-scale model for turbulent shear flow: Algebraic theory and applications. *Phys. Fluids* **16** (10), 3670–3681. 16, 17

Walsh, M. J., ed. 1982 *Turbulent boundary layer drag reduction using riblets*. 95

Willis, A. P., Hwang, Y. & Cossu, C. 2010 Optimally amplified large-scale streaks and drag reduction in turbulent pipe flow. *Phys. Rev. E* **82** (3), 1–11. 3, 7, 43, 54

Zagarola, M. V. & Smits, A. J. 1998 Mean-flow scaling of turbulent pipe flow. *J. Fluid Mech.* **373**, 33–79. 2

Zanoun, E.-S., Nagib, H. & Durst, F. 2009 Refined c_f relation for turbulent channels and consequences for high- Re experiments. *Fluid Dyn. Res.* **41** (2), 021405. 21

Zare, A., Jovanović, M. R. & Georgiou, T. 2017 Colour of turbulence. *J. Fluid Mech.* **812**, 636–680. 7, 26

Zhang, C & Chernyshenko, S. I. 2016 Quasisteady quasihomogeneous description of the scale interactions in near-wall turbulence. *Phys. Rev. Fluids* **1**, 014401. 9

Zhou, J., Adrian, R. J. & Balachandar, S. 1996 Autogeneration of near-wall vortical structures in channel flow. *Phys. Fluids* **8** (1), 288–290. 7

Zhou, J., Adrian, R. J., Balachandar, S. & Kendall, T. M. 1999 Mechanisms for generating coherent packets of hairpin vortices in channel flow. *J. Fluid Mech.* **387**, 353–396. 10, 52

Appendix A

Dynamic Mode Decomposition

The parameters for the DMD need to be chosen very carefully. Hereafter, we discuss how we have chosen the three main parameters of the DMD: i.e. the sampling time-interval Δt, the number of snapshots N, and the number of POD modes r.

A.1 Sampling time interval Δt

The theoretical upper bound for the sampling time step is represented by the Nyquist criterion, which applies to the frequency of the process we are interested in (i.e. streak instability). There is also a lower bound, since a too high sampling rate could result in this feature being perceived as quasi-steady (Schmid, 2010). The typical time scale of the self-sustaining process in the outer layer is $T_{ssp}u_\tau/h \simeq 3$ and the time scale of the streak instability is even shorter (Hwang & Bengana, 2016). To provide a good resolution for this time scale, four different snapshot time intervals have been tested with S960: $\Delta t u_\tau/h = 0.009,\ 0.018,\ 0.027,\ 0.036$. The two smaller values yield eigenvalues of $\mathbf{S}$ lying almost perfectly on the unit circle $|\mu| = 1$ (see fig. 3.8), and the smallest value has been used for the DMD analysis in the present study.

A.2 Total number of snapshots N

The minimum number of snapshots N is determined as follows. We first assume that the N-th snapshot is given by a linear combination of all previous $N-1$ snapshots with a residual vector $\mathbf{r}$: i.e.

$$\psi_N = \mathbf{\Psi_0}\mathbf{a} + \mathbf{r}, \tag{A.1}$$

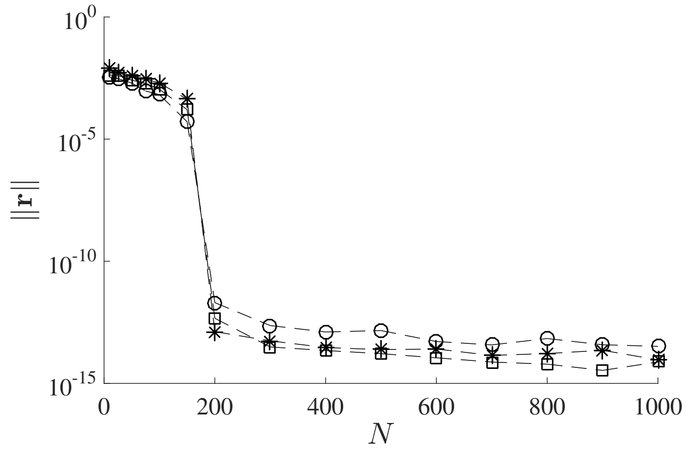

Figure A.1: The norm of the residual vector with the number of snapshots N (S960): $*$, $A_s^+ = 3.42$; $\square$, $A_s^+ = 4.04$; $\diamond$, $A_s^+ = 4.76$.

where $\mathbf{a} = [a_1\ a_2\ ...a_{N-1}]^T$ is a column vector for the coefficients of the linear combination. If the norm of $\mathbf{r}$ approaches zero for sufficiently large N, the number of snapshots may be considered large enough to cover any flow field using the snapshots. The minimum residual $\mathbf{r}$ is computed with the economy-size QR decomposition of the snapshots $\mathbf{\Psi_0} = \mathbf{QR}$, and the coefficients of the linear combination are given by

$$\mathbf{a} = \mathbf{R}^{-1}\mathbf{Q}^H\psi_N. \tag{A.2}$$

The residual and its 2-norm are then found with (A.1) and (A.2).

Fig. A.1 shows the dependence of the 2-norm of $\mathbf{r}$ on the number of snapshots. The test was carried out with $\Delta t u_\tau/h = 0.009$ using the S960 simulations with three different forcing amplitudes. At $N \simeq 200$, the 2-norm of the residual vector drops drastically, and falls below $O(10^{-10})$. However, further increase in the number of snapshots N does not decrease the residual vector significantly, and it remains at $O(10^{-15})$ even for $N = 1000$. The number of snapshots chosen in the present study is $N = 1000$. We note that this number also ensures that the total time interval of the snapshots is $Tu_\tau/h \simeq 9$, which would be six to nine times longer than the streak meandering time scale observed in Hwang & Bengana (2016).

A.3 Number of POD modes r

The choice of the number of POD modes to be included has been based on the amount of energy contained in the first r POD modes. Here, $N = 1000$ and $\Delta t u_\tau/h = 0.009$, and the

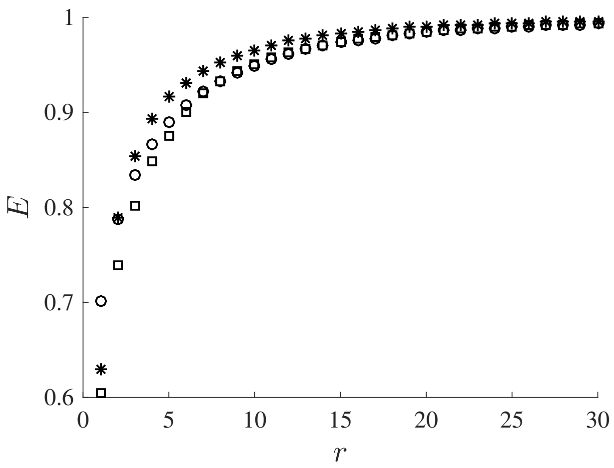

Figure A.2: Energy content of the first r POD modes (S960): $*$, $A_s^+ = 3.42$; $\square$, $A_s^+ = 4.04$; $\diamond$, $A_s^+ = 4.76$.

calculations were performed with the $S960$ simulations. If the matrix of snapshots is decomposed as $\mathbf{\Psi}_0 = \mathbf{U}\Sigma\mathbf{V}^H$, the relative energy content up to the r^{th} mode is computed by:

$$E = \frac{\sum_{i=1}^{r} \Sigma_{ii}}{trace(\Sigma)}. \tag{A.3}$$

Fig. A.2 reports the dependence of E on r. With only the first twenty-five modes, more than 95% of the total energy is recovered. Given this feature, it is evident that the use of all the POD modes is not necessary. Furthermore, appropriate truncation of the number of POD modes would help for eliminating noise associated with background turbulence, as higher-order POD modes are expected to contain such noise. Therefore, in the present study, thirty POD modes are used to ensure to contain all the energetic features in our DMD analysis, while appropriately removing the effect of noisy small-scale background in the snapshots.

Appendix B

Effect of various parameters on skin-friction prediction

B.1 Comparison of box streamwise domain

The effect of the streamwise domain size on the skin friction coefficient is examined here for $L_z = 0.5h$ and $L_z = 1.5h$, and is reported in table B.1. For $L_z = 1.5h$, three different streamwise domains are tested with $L_x = 3, 6, 9h$. The change of the skin friction change little with $\Delta C_f < 2\%$ even for $L_x = 2L_z$, as one would have expected from the existing literatures (e.g. Lozano-Durán & Jiménez, 2014). In the case of $L_z = 0.5h$, this behaviour remains essentially the same, justifying the use of short streamwise domains for the box-confinement approach.

B.2 Influence of uniform spanwise mode in small and large streamwise computational domains

With the box-confinement approach applied to DNS at low Reynolds numbers, it was previously shown that the role of the spanwise uniform mode ($k_z = 0$) in turbulent skin friction is very limited (Hwang, 2013). Here, the related discussion is further extended for larger $L_z(= \lambda_{z,t})$, and, in particular, here we show that their effect in a short streamwise computational domain is even smaller than that in a long streamwise computational domain. This is presumably because the short streamwise computational domain does not allow for an enough streamwise space required for the spanwise uniform motion, which was found to be energetic at $\lambda_x \simeq 2 \sim 4h$ (Hwang, 2013). Fig. B.1 shows the spanwise wavenumber spectra of following three tested cases

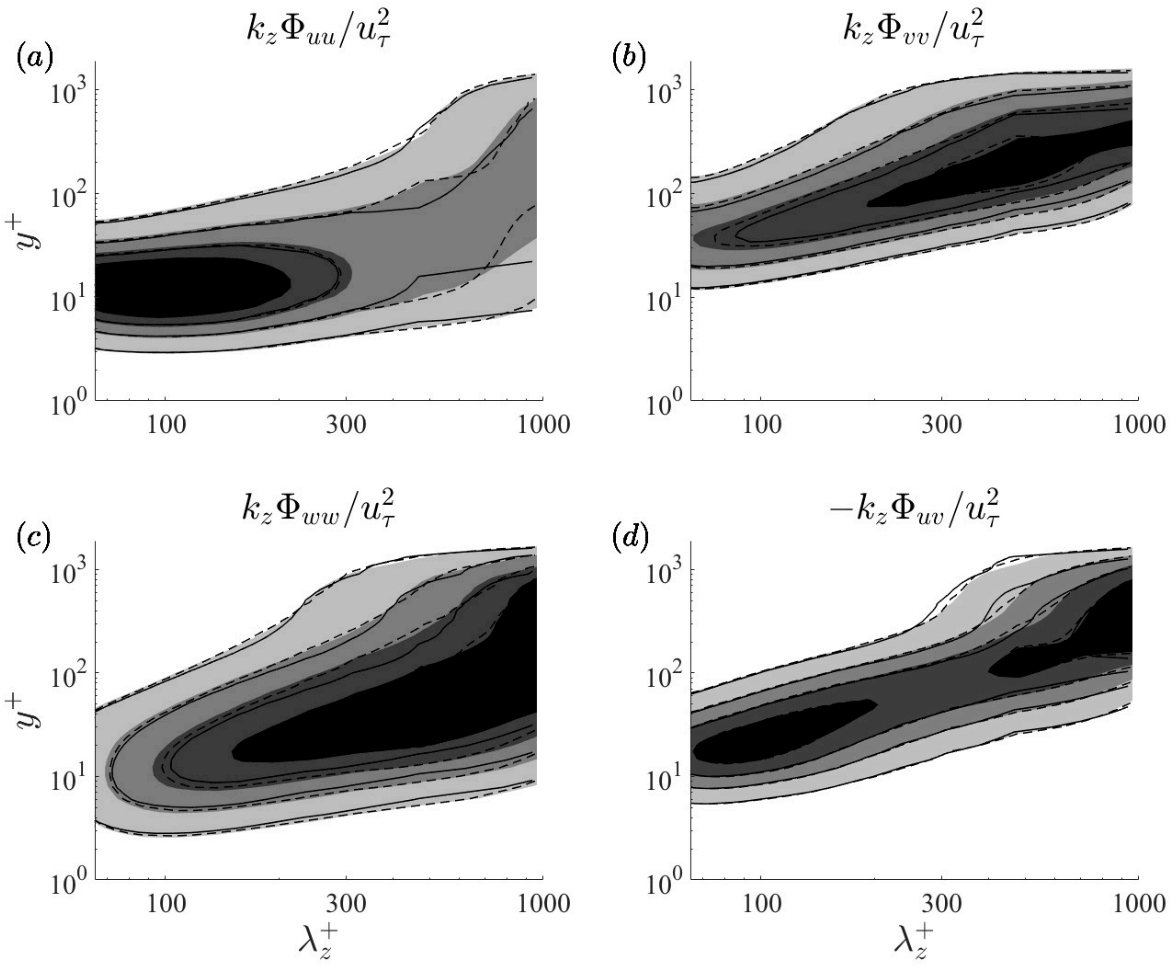

Figure B.1: Premultiplied one-dimensional spanwise wavenumber spectra of (*a*) streamwise, (*b*) wall-normal, (*c*) spanwise velocities, and (*d*) Reynolds shear stress for $L_z = 0.5h$. Here, the solid, dashed and shaded contours indicate $L_x = 1h$ with the spanwise uniform mode ($M2000a$), $L_x = 1h$ without the spanwise uniform mode, and $L_x = 4h$ without the spanwise uniform mode, respectively. The contour labels are chosen to be 0.2, 0.4, 0.6, 0.8 times each of the maximum for comparison.

Case	Re_m	Re_τ	L_x/h	L_z/h	Δx^+	Δz^+	Δy_1^+	C_f $(\times 10^{-3})$	$\Delta C_f(\%)$
$M2000a$	89,100	1863	1.0	0.5	58.2	29.1	1.31	3.50	1.7 %
$L2000a$	89,100	1854	2.0	0.5	57.9	28.9	1.30	3.46	0.6 %
$VL2000a$	89,100	1848	4.0	0.5	57.7	28.8	1.30	3.44	Ref.
$M2000$	89,100	2070	3.0	1.5	64.7	32.3	1.45	4.32	1.4 %
$L2000$	89,100	2061	6.0	1.5	64.4	32.2	1.44	4.28	0.5 %
$VL2000$	89,100	2056	9.0	1.5	64.2	32.1	1.44	4.27	Ref.

Table B.1: Effect of the streamwise computational domain on the friction coefficient with $L_z = 0.5h$ and $L_z = 1.5h$. Here, $\Delta C_f = |C_f - C_{f,0}|/C_{f,0}$ where $C_{f,0}$ is the friction coefficient of each of the reference cases (i.e. $VL2000a$ for $L_z = 0.5h$ and $VL2000$ for $L_z = 1.5h$). Note that, for each L_z, the case with the longest streamwise domain is chosen as the reference case.

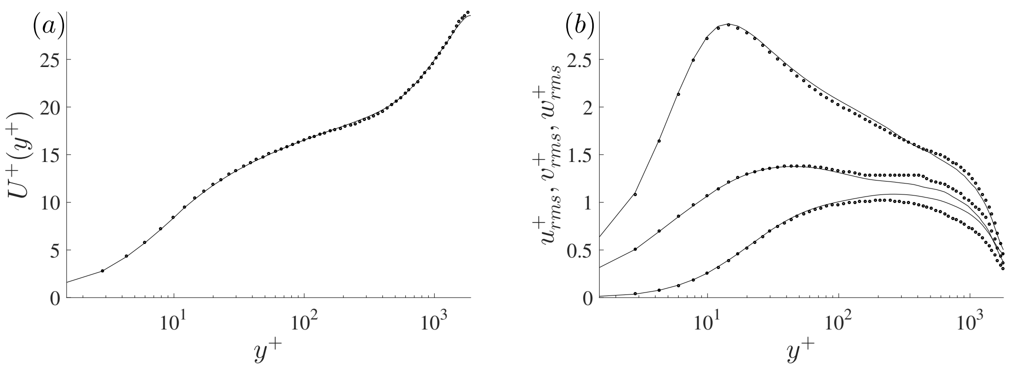

Figure B.2: (a) Mean velocity profile and (b) turbulent velocity fluctuations at $Re_\tau \approx 2000$ $(L_x = 1h)$: ——, $L_z = 0.5h$ with uniform mode; $\circ$, $L_z = 0.5h$ without uniform mode.

for $L_z = 0.5h$: 1) the short domain ($L_x = 1.0h$) with the spanwise uniform mode (solid; $M2000a$ in table B.1); 2) the short domain ($L_x = 1.0h$) without the spanwise uniform mode (dashed); 3) the long domain at least for this case ($L_x = 4h$) without the spanwise uniform mode (shaded). Overall, the spectra of the three tested cases do not show significant difference from one another, except for the streamwise velocity spectra. However, this may have been expected, given the streamwise elongated nature of the streamwise velocity fluctuation. The overall deviation of the spectra (especially for the Reynolds shear stress) appears to be reasonably small, suggesting the relatively minor roles of the spanwise uniform mode and the streamwise box size. The role of the spanwise uniform mode in first- and second-order statistics is also examined for $L_z = 0.5h$, as reported in fig. B.2. The change in the mean velocity appears to be little, consistent with the very small change in C_f in fig. 5.1. Some non-negligible effect was observed in the velocity fluctuations, but they also appear to be small and insignificant, explaining the minor role of the spanwise uniform mode in skin-friction generation.